Parametric study of lower limb bone fracture under impact loading considering nonlinear characteristics of bone.

ANGLIA RUSKIN UNIVERSITY AND UNIVERSITY OF BATH

Rosaliyo Samuel

SUPERVISOR | DR. MEHRDAD ASADI

Table of Contents

Table of Figures

Parametric study of lower limb bone fracture under impact loading considering nonlinear characteristics of bone.

1. Abstract:

In our human body, bones support our skin, muscle, tissues and all the organs inside. It gives our body the frame to sustain the body structure. Bones are non-rigid materials that can fracture if it undergoes heavy loading or a sudden impact. To study and understand how bones behave under different circumstances, Finite Element Analysis can be done to interpret real life situations through computer simulations. However, one of the key essential into getting accurate results is determining that the material used in the simulations is very similar characteristics to the real life bone material and the boundary conditions are set right.

This report discusses on various material types used to model a bone as a non-rigid material and its validation to real life test results. Results from different published papers are analysed to find the apt material that could be used to depict a closely accurate simulation of a lower limb bone fracture to real life scenario. It also aims to help determine the boundary conditions that could be used to perform the simulations.

2. Introduction:

Fractures of lower limb bones are very common when it comes to automotive collisions and military underbody blasts where a high impact force is applied in a short period of time. The fracture type can be oblique, comminuted, spiral or compound and they depend on various factors such as age, diet, physical activity, osteoporosis, weight etc.

In the modern world it is possible to understand how matter from metals to bones would behave when under impact through the help of finite element analysis software's. However, the model needs to be designed accurately, right properties and boundary conditions must be set in order to obtain reliable results. Bone being a matter of complex design, anisotropic, viscoelastic and dependent on the belonging person's characteristics and wellbeing, is a tough design to manipulate. However, the prime focus of this paper is given onto researching on, how to create and simulate FE models of bone accurately reflecting its material properties and considering it as a non-rigid material.

Different researchers have used different simulation software's to analyse their bone model and they all follow a basic backbone structure of geometry creation and manipulation where they acquire the model's geometry data along with its material properties (material properties obtained from existing experimental results or their own experiments) and decide the boundary conditions. Then they perform the finite element modelling where the model is meshed and all the material properties and boundary conditions are set or entered. Finally, they get result output for parameters such as stress, strain, fracture rate etc. which is compared with the experimental results for validation. Although the basic layout of the procedure is same for all researchers the details of their processes and assumptions are distinct.

3. Human Bone characteristics and composition:

All bones consist of living cells embedded in the mineralized organic matrix that makes up the bone tissue. The primary tissue of bone, bone tissue, is a relatively hard and lightweight composite material, formed mostly of calcium phosphate in the chemical arrangement termed calcium hydroxylapatite (this bone tissue gives bones their rigidity). It has relatively high compressive strength but poor tensile strength, meaning it resists pushing forces well, but not pulling forces (Umadevi and Geethalakshmi, 2011).

The bone tissue is a viscous-elastic material whose mechanical properties are affected by its deformation grade. The flexibility properties of the bone are provided by the collagen material of the bone. The collagen content gives the bone the ability to support tense loads. The bone is also a fragile material and its force depends on the load mechanism. The fragility grade of the bone depends on the mineral constituents that give it the ability to support compressive loads. Bone is a highly adaptive material and very sensitive to disuse, immobilization or vigorous activity and high load levels. The bone tissue can be separated and may change its properties and setting in response to the mechanical demand. It was determined at first by the German anatomist, Julius Wolff, that gave us the theory on the bone development named Wolff Law, that says: "Each change in the form and function of a bone or only its function is followed by certain definitive changes in its internal architecture, and secondary changes equally definitive in its external compliance, in accordance to the mathematics law". (Alberts et al., 1994; Junqueira & Carneiro, 1997, 1999).

The exterior of bones (except where they interact with other bones through joints) is covered by the periosteum, which has an external fibrous layer, and an internal osteogenic layer. The periosteum is richly supplied with blood, lymph, and nerve vessels, attaching to the bone itself through Sharpey's fibers. Bone can also be either woven or lamellar (layered). Woven bone is weak, with a small number of randomly oriented collagen fibers, but forms quickly and without a pre-existing structure during periods of repair or growth. Lamellar bone is stronger, formed of numerous stacked layers and filled with many collagen fibers parallel to other fibers in the same layer. The fibers run in opposite directions in alternating layers, assisting in the bone's ability to resist torsion forces (Bankoff A., 2012).

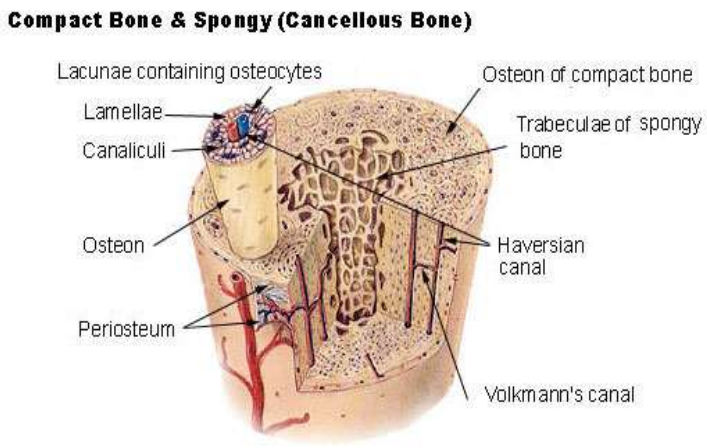

Figure 1: Bone tissue matrix (New world encyclopaedia, 2006)

3.1 Anisotropic Characteristics Bone tissue:

The bone is an anisotropic material, indicating that the bone behavior will change depending on the direction of the load application. In general, the bone tissue may lead to higher loads in the longitudinal direction and a lesser quantity of load when applied over the bone surface. The bone is strong to support loads in the longitudinal direction because it is used to receive loads in this direction. (Holtrop, 1975).

3.2 Viscoelastic Characteristics:

The bone is also viscoelastic, which means that it responds differently depending on the speed to which the load is applied and the length of the load. In very fast speeds of load placement, the bone can lead to higher loads before it fails or breaks. As showed in the figure below, the bone that receives the load slowly breaks with a load that is approximately half of that it could support if the load was more quickly applied (Bankoff, 2007, p.123).

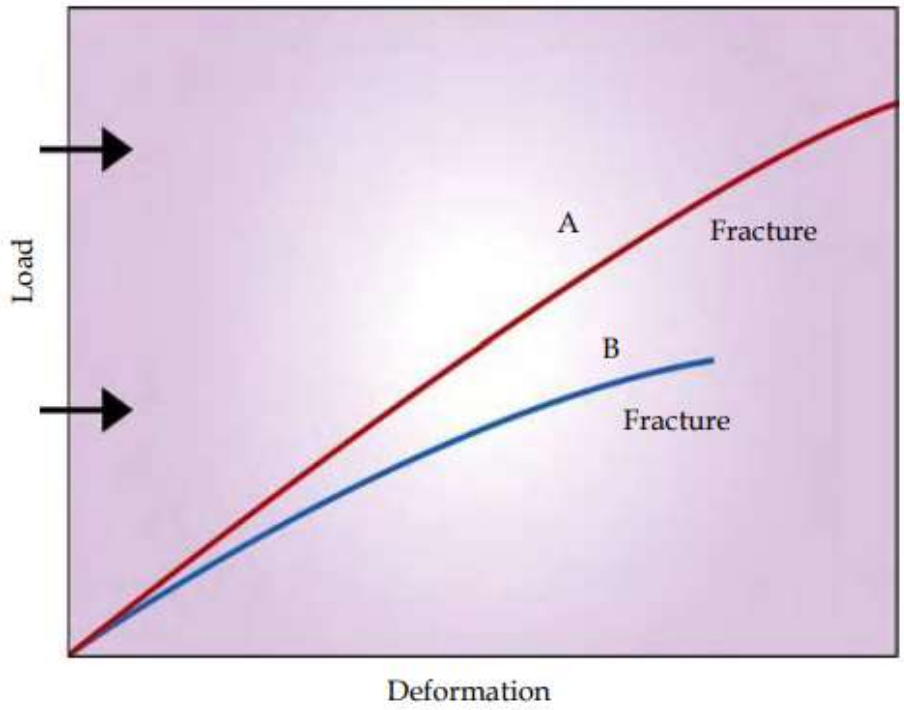

Figure 2: Viscoelastic characteristics of bone. (Bankoff, 2007, p.123)

A) When it receives the load quickly, the bone responds more rigidly, and may handle a higher load before it breaks.

B) When it receives the load slowly, the bone is not so rigid or strong, breaking under lesser loads.

3.3 Elastic Response:

When the load is firstly applied, a bone is deformed by a change in the extent or angular format. The bone is deformed up to 3%. This is considered the elastic amplitude of the load-deformation curve because, when the load is removed, the bone is recovered and goes back to the original format or extent.

3.4 Plastic Response:

With the continuous placement of load on the bone tissue, its deformation point is reached, after which the external fibers of the bone tissue will start to cede, experiencing micro-breaks and disconnection of the material within the bone. (Hay, 1982; Holtrop, 1975).

3.5 Strength:

The strength of the bone or any other material is defined by the point of failure or by the load sustained before the failure. The strength may also be analysed in terms of storage of energy, the area under the load-deformation or stress-distension curve. (Holtrop, 1975; Bankoff, 2007).

3.6 Hardness:

The hardness, or elasticity module of a material, is determined by the decrease of the load-deformation curve during the amplitude of the elastic response and is represented by the resistance of the material to the load as the structure is deformed. This response occurs in many materials, including bones, tendons and ligaments (Bankoff A., 2012).

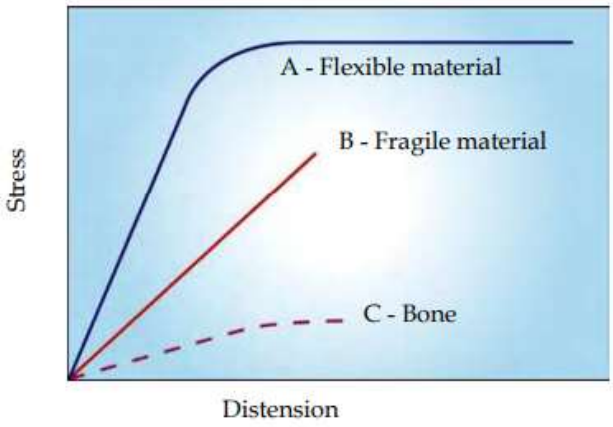

Figure 3: Stress vs distension curve for flexible material, fragile material and bone (Bankoff, 2007, p. 124)

A hard material will respond with a minimum deformation to the load increase. When the material fails in the end of the elastic phase, it is considered a fragile material. The glass is an example of fragile material. The bone is not so hard as the glass or metal, and, differently of those materials, it does not respond linearly, because it cedes and deforms not uniformly during the load placement phase. The higher the load imposed to the bone, the higher the deformation. In addition, if the load exceeds the elastic limits of the material, there will be a permanent deformation and failure of the material. If a material continues to over-elongate and over-deform in the plastic phase, it is known as flexible material. (Choi & Goldstein, 1992). The skin is an example of material that is deformed considerably before the failure. The bone is a material that has properties that respond in both the fragile and the flexible mode. (Choi & Goldstein, 1992).

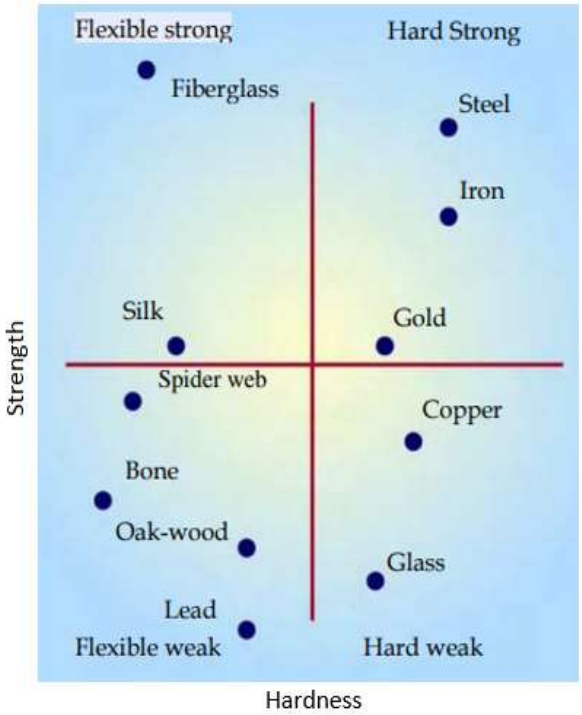

Figure 4: Strength and stiffness of bone compared to other materials. The bone is considered flexible and weak Bankoff (2007, p. 124).

3.7 Bone composition:

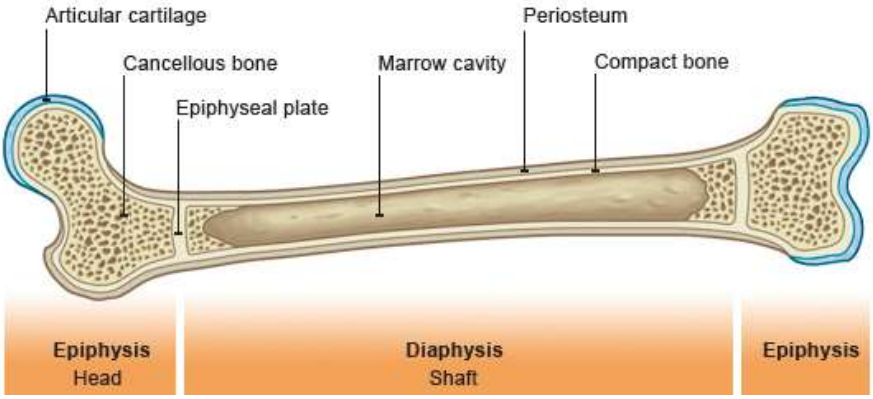

Figure 5: Composition of femur bone (BBC Bitesize, 2014)

The outer hard surface of the bone is referred to as compact bone and the soft sponge inside is the cancellous bone.

3.8 Loading and fracture types:

The skeletal system is subjected to a variety of different types of forces on such a way that the bone receives loads in different directions. There are loads produced by the weight sustentation, by the gravity, by muscle forces and by external forces. The loads are applied in different directions producing forces that may vary from five different types: compression, tension, shear, curvature or torsion (Shipman, Walker & Bichell, 1985).

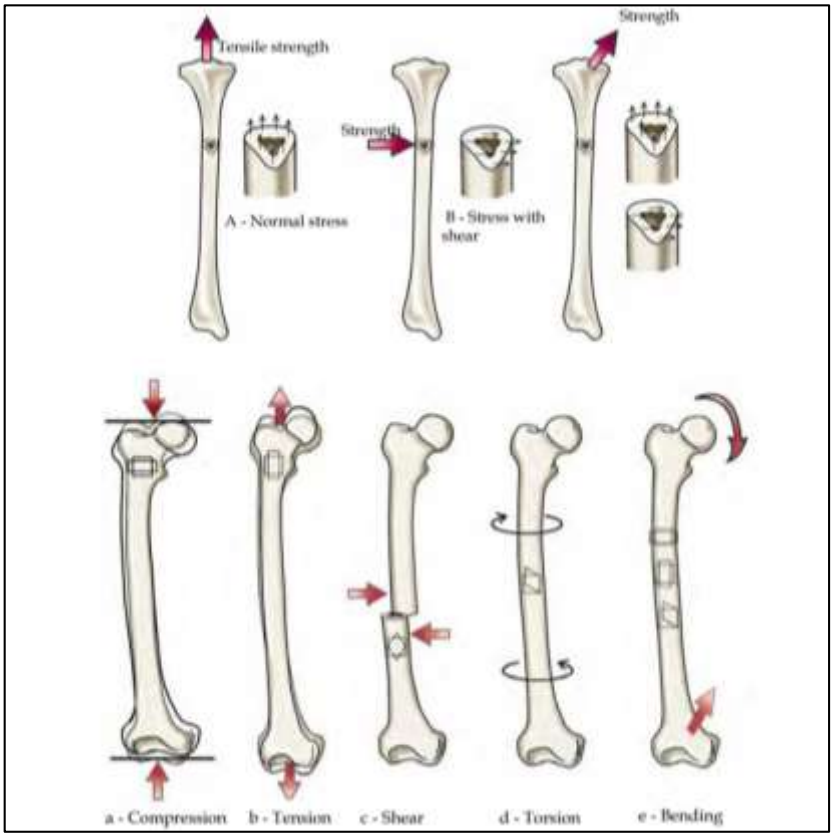

Figure 6: Different types of loading conditions in a femur bone Bankoff (2007, p. 126)

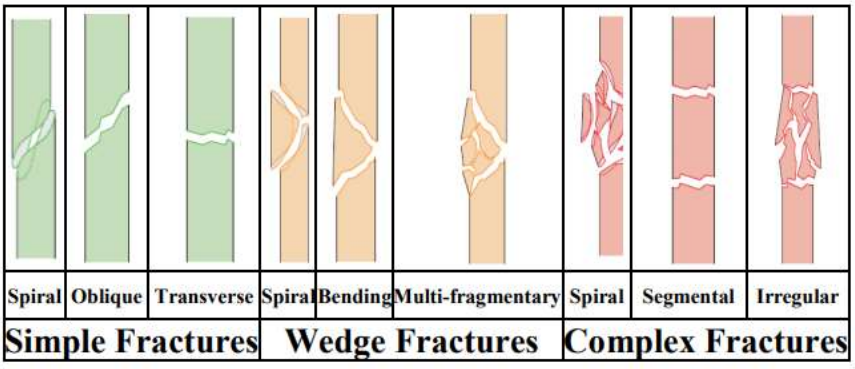

Figure 7: Tibia bone fracture types (Umadevi & Geethalakshmi, 2011)

4. FEA Analysis of human femur bone: (Pape focus: Femur Hexahedral mesh)

4.1 Introduction and Overview

The human bone is anisotropic in nature meaning that its material properties such as young's modulus differ along with the direction of the object. The finite element method was first used in bone biomechanics for analysis of mechanical behaviour of skeletal parts in 1972 (Huiskes and Chao, 1983). Steadily this method has become very popular in biomechanics field. Finite element modelling (FEM) has three major stages to analyse the human bones i.e. pre-processor, solution, and the post process stage. In the pre-process stage a CAD model is required to be generated. The geometry and material properties (CT Hounsfield Units) of bone can be acquired from computed tomography (CT) or through a 3D laser scan. The geometry of fracture fixation is usually developed on CAD software like CATIA, Solid works, Pro/E etc. Once the bone model is developed the mesh generation is carried out. The material properties to each model is assigned and finally the boundary conditions are applied. It is essential to apply the correct boundary conditions in FEM to get accurate results (Parashar S. & Sharma J., 2016).

In brief, the actions performed by the solver are selection of failure criteria, generation of element mesh, implementation of material properties, determination of loading and boundary conditions and definition of analysis. The FE solver will give us results on Formulation of stiffness matrix for each element, Substitution of element stiffness matrices to whole model stiffness matrix and Solving of unknown quantities and calculation of stress-strain distributions (Parashar S. & Sharma J., 2016).

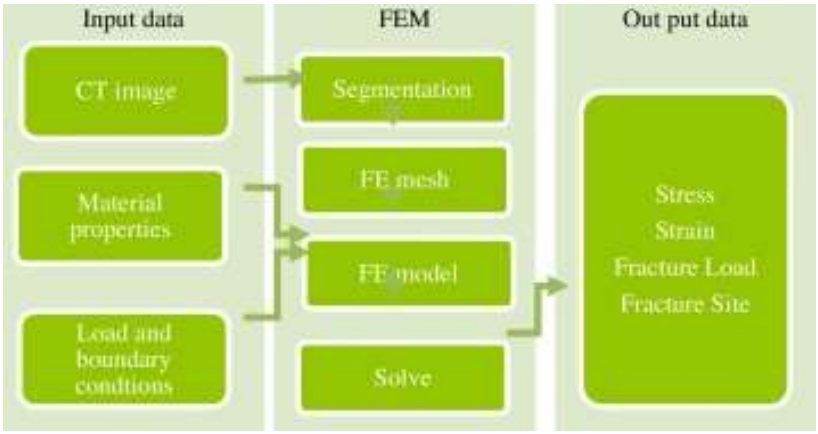

Figure 8: Finite element modelling of bone based on CT images (Parashar S., 2016)

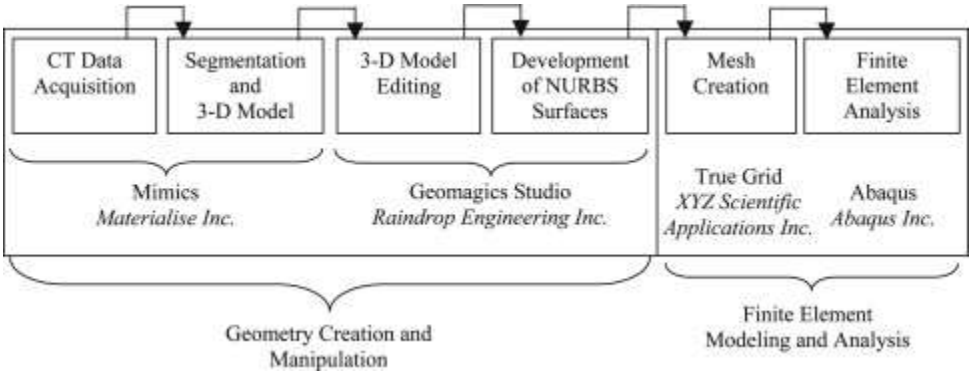

Figure 9: Model development process outline example with the software's used (Schonning A., 2009)

4.2 Data acquisition and three–dimensional model generation:

To perform the task of image segmentation, the CT data was imported into a medical imaging and editing software, in the present case Mimics (Materialize). Separate volumes were generated for the cortical bone, cancellous bone and the bone marrow. A semi-automated segmentation algorithm was used in conjunction with a region-growing algorithm applied to interpolate the 2D-image data, resulting in the generation of three-dimensional models (Shonning et al., 2009)

4.3 Geometry data filtering and NURBS development

The volumes generated were edited further using a reverse- engineering software package called Geomagics Studio (Raindrop Engineering). The imported geometry had rough surfaces and included some inaccuracies (interpolation algorithms were used in estimating the surface between the 1 mm separated scans, threshold values were estimated in defining the boundary of the bony tissue, and editing techniques were used on slices). While some details were removed from the models through the available smoothing techniques, it aided in generating the FE mesh (Shonning et al., 2009).

Figure 10: Femoral head before and after smoothening (Shonning et al., 2009).

To best prepare the geometry for meshing, the polygonal surface was replaced by a highly compliant NonUniform Rational B-Spline (NURBS) surface. It was comprised of rectangular patches, as shown in figure below, which aided in the meshing process. For the model at hand, it was desired to create surface patches that could easily be "mapped" into block structures in the mesh generation software. The NURBS surface was exported as an *.IGES file. The methodology described was carried out for the cortical, cancellous, and the bone marrow volumes (Shonning et al., 2009).

Figure 11: NURBS patch layout (Shonning et al., 2009).

4.4 Material properties:

The mechanical properties of bones vary according to age, species, anatomical site etc. The outer hard and dense part of the bone is called the cortical bone. Elastic isotropic cortical bone values were derived from the table on right (Jade S., 2014).

Material properties			
	Cortical bone	Cancellous bone	Bone marrow
E (MPa)	17,000	750	300
υ	0.33	0.33	0.45

Figure 12: Material properties for cortical bone (Shonning et al., 2009)

4.5 FE model mesh configuration:

Due to the complexity of anatomical geometry, tetrahedral elements are most commonly used in biomechanical applications as the meshing process is automated. However, hexahedral elements are more preferred but they require extensive manual meshing but provide significant benefits such as regularity, angle distribution and anisotropy. In comparing linear tetrahedral and hexahedral elements it has been judged that hexahedral elements give better quality results in many structural applications, including linear static bending, linear static torsion, and non-linear elasto-plastic analysis. The quadratic tetrahedral element has been found to be adequate for many structural applications; Nevertheless, hexahedral elements showed improved convergence and sensitivity to mesh orientation. General contact problems perform better with linear as opposed to second order elements (Shonning et al., 2009).

4.6 Hexahedral mesh development:

A commercial FE meshing software package (TrueGrid), using a multi-block approach that allows for the generation of highly controllable hexahedral meshes, was employed. This software was preferred as it is used as a preprocessor for a vast number of FE packages. The outline specified here may be of aid for mesh construction using other multi-block meshers. When using a multi-block mesher, the analyst divides the structure into manageable blocks. These blocks are then subdivided into elements. The subdivision of the geometry into manageable blocks will here be referred to as the block structure.

The femur was modelled in four distinct steps; the first tackled the bone marrow, the second included the cancellous bone as well as part of the cortical bone along the diaphysis, the third step consisted of modelling the cortical bone around the femoral head, greater trochanter, condyles and the remaining cortical bone along the diaphysis; and the fourth and final step included merging eight extra blocks to the femoral structure. Each of these steps is described in the following subsections.

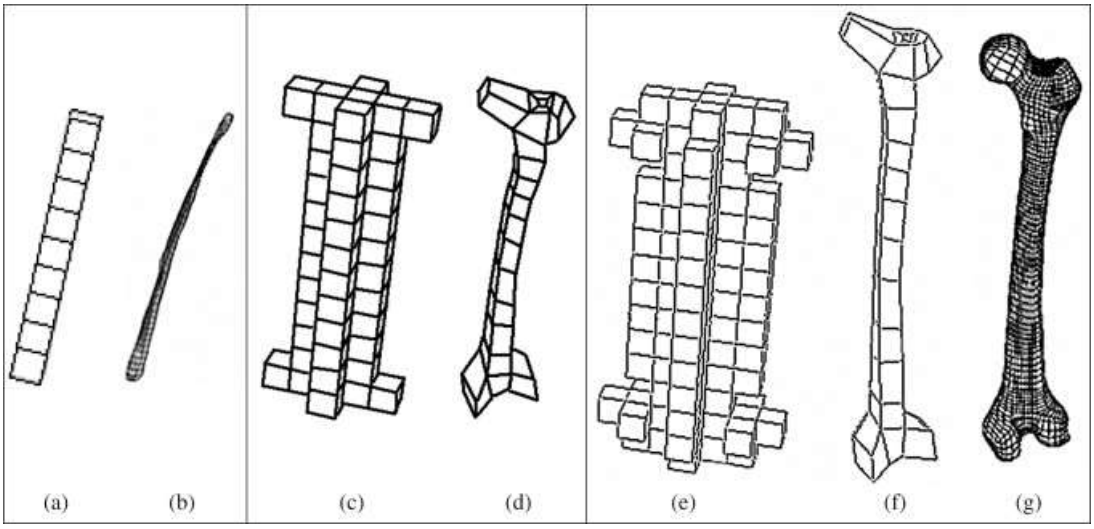

Figure 13: Development of block structure (Shonning et al., 2009)

A) Block structure of bone marrow, B) Marrow block structure mesh projected onto the geometry. C) Block structure of cancellous volume, D) Block structure mesh of the cancellous volume and part of the cortical volume along the diaphysis of the femur. The block structure is attached to the geometry. E) Cortical bone structure after removing

unnecessary blocks F) block structure after bounding specific faces and G) Resulting mesh following projection of the faces and subdivision into hexahedral elements.

The *.IGES geometry of the bone marrow volume was imported into TrueGrid. A block structure was generated, as seen in fig. 13a. Each of the corners of the blocks was attached to the appropriate geometry vertices, followed by projection of the blocks' faces onto the geometry's "combined surfaces". Upon completion of the projection, the mesh density was increased to ensure that the projection was performed properly. The block mesh projected onto the marrow geometry is shown in fig. 13b.

Figure 13d shows the block structure attached to the geometry. This figure illustrates the mesh after all of the block-boundary commands had been applied, after the corners of the computational blocks had been attached to the vertices of the physical geometry, and after the faces of the blocks had been projected onto the "combined surfaces" of the geometrical structure. Where highly irregular geometry occurs it was necessary to also attach the edges of the block structure to the curves of the geometry. One location of highly irregular geometry occurs at the condyles. In studying the block structure of Fig. 13c - 13d, it should be noted that the centre elements include the medullar volume. However, above and below the medullar volume are now blocks/elements that will be assigned material properties of cancellous bone. Blocks along the diaphysis will be assigned material properties of cortical bone.

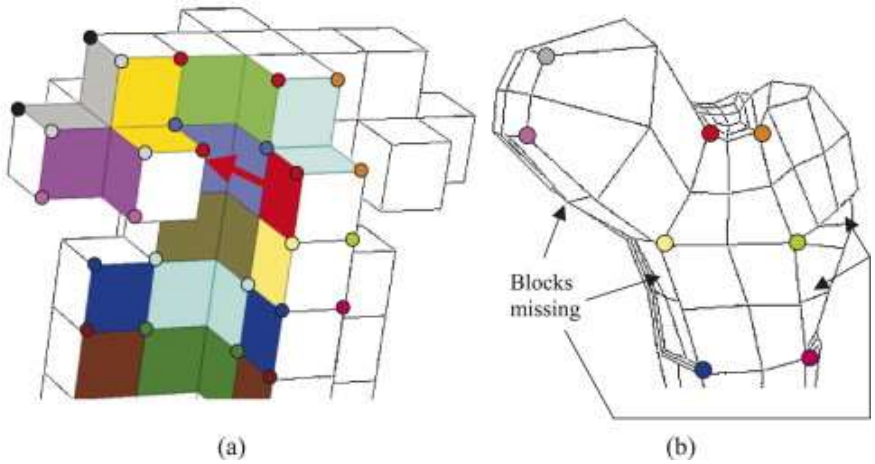

Figure 14: Block-structure at femoral head before (a) and after (b) application of the block-boundary commands. (Shonning et al., 2009)

The mesh generated in True Grid consisted of 8832 eight-noded hexahedral elements with a total of 9505 nodes. This mesh was imported into Abaqus Standard (Abaqus Inc.), a commercially available FE software package, where the element type C3D8 (Eight node brick element), a three-dimensional linear stress-element type, was chosen (Shonning et al., 2009).

4.7 Boundary conditions and loads:

The femur was constrained at the distal end of the condyles to hinder motion in all degrees of freedom resembling the contact with the tibia. The loading condition consisted of the joint reaction force distributed at the femoral head and the abductor muscle force distributed on the greater trochanter.

Figure 15: Femoral loads (Shonning et al., 2009)

	x	y	z
Joint reaction force ($F1$) (N)	−616	171	−2800
Abductor muscle force ($F2$) (N)	430	0	1160

Figure 16: Applied loads (Shonning et al., 2009)

4.8 Results:

The femoral bone was subjected to a joint reaction force on the femoral head and an abductor muscle force at the greater trochanter. The stresses and displacements of the femoral model were obtained using a standard FE software package, Abaqus Standard (Abaqus Inc.). The highest von Mises stress (37 MPa) was recorded for a location on the medial side of the femur, directly distal to the femoral head in the cortical volume, as shown in figure 17.

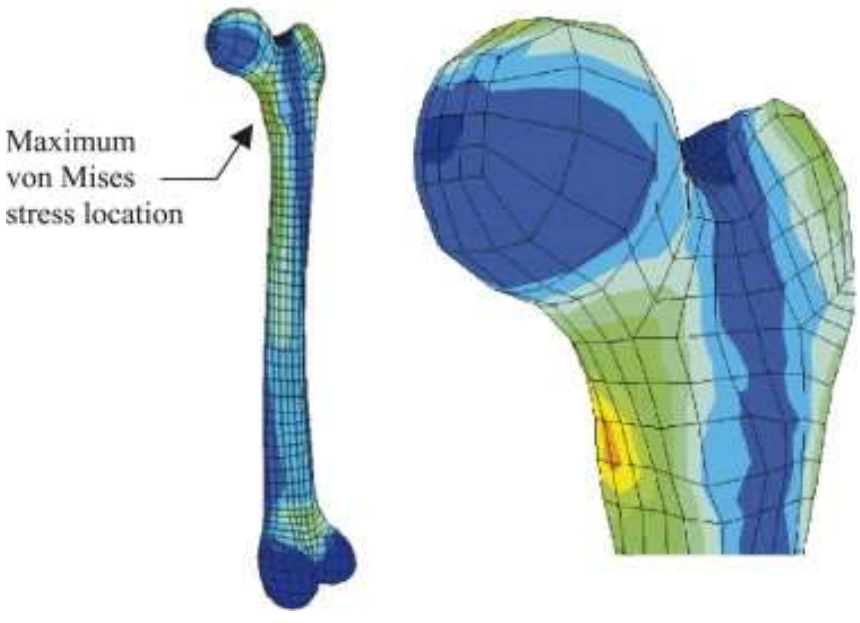

Figure 17: Von-mises stress distribution (Shonning et al., 2009)

Although it is known that von Mises stresses are not adapted for the behaviour of biological tissues, being a failure criterion for ductile metals, most results pertaining to FE studies of bones are given in terms of von Mises stresses. For easier comparison, the stresses here are also presented in terms of the von Mises effective stress.

The largest displacement magnitude of 3.1 mm is located at the superior end of the femur where no constraints are applied. The medial/lateral displacements, with a maximum value of 2.6 mm, are largest in close proximity to the load applications and are almost non-existent in the inferior half of the femur. The greater trochanter has the largest posterior displacement of 1.7 mm. The femoral head has a 1 mm displacement in the inferior direction while the greater trochanter has a superior displacement of 0.35 mm. This “rotating effect” is the cause of the opposing inferior/superior components of the applied joint and muscle loads. Overall, the displacements are largest close to the load applications and are reduced for locations further away; a zero displacement is obtained at the distal end of the condyles, verifying proper functionality of boundary conditions (Shonning et al., 2009).

4.9 Conclusion:

- During meshing clear the surface to produce a smooth geometry as minor surfaces can result in poor meshing which will affects the solver output time and the results.

- Hexahedral mesh models perform better than tetrahedral mesh models and give better outputs especially when contact analysis is to be done and they showed improved convergence and sensitivity to mesh orientation.

- Best results are obtained when meshing is done manually then when applied automatically by the software. However, extensive effort needs to be put in.

- The only disadvantage of this type of meshing is the time and effort that needs to be applied.

5. FEA Analysis of human cortical bone: (Paper focus: Rib cortical bone material properties and strain rates)

5.1 Introduction and Overview

Thoracic trauma is the principal causative factor in 30% of road traffic deaths. And when 6 or more ribs are fractured, mortality rate and associated injuries to the head and thorax are increased significantly (Beaupied H., 2007).

This report was carried out to improve the understanding of the mechanical properties of the human rib. These properties are necessary in order to develop realistic finite element models of human chest which are used in the field of vehicle safety. The purpose of this study was to collect values for the rib mechanical properties obtained experimentally. And to compare the values of material properties of human rib cortical bone used in the FE simulation of THUMS (Total Human Model for Safety) with the material properties of human rib cortical bone of PMHS analyzed by Kemper et al. with a tensile test (Kemper A., 2005).

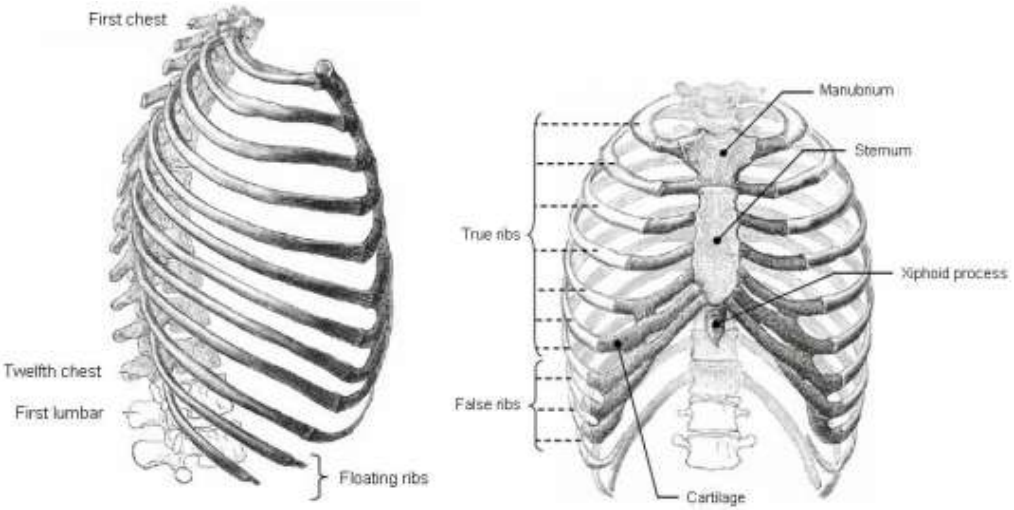

Figure 18: Different parts of a rib

The ribs themselves are composed of cancellous (spongy or trabecular) bone surrounded by a cortical shell which is compact and solid.

5.2 Mechanical properties of ribs:

Young's modulus of rib cortical bone	7.51 to 20 GPa
Young's modulus of cancellous bone	1.4 to 9800 MPa

Figure 19: Mechanical properties of ribs

This wide range in the values of the elastic modulus is due to a lot of factors that affect the values of mechanical properties measured experimentally. The values of mechanical properties depend on the type of test (tensile, compressive, bending, shear, etc), on the characteristics of the tested subject (age, gender, weight, bone mineral density, etc) rib level and location of the specimen, on the type of subject (cadaver or living human), the load distribution, and so on.

The cortical bone structure is very compact, heterogeneous, viscoelastic and anisotropic (Charpali E., 2006): Bone has heterogeneous structure; it means that the properties vary with the point. Bones have viscoelastic properties; it means that the mechanical behavior depends on the speed at which the load is applied. The higher the strain rate is the higher the stress at a given strain (Ordaka J., 2006). Bone is also an anisotropic material; it means that it has different mechanical properties when loading is applied along different axes. It is caused by the structure of bone, which is dissimilar in the transverse and longitudinal directions (Ordaka J., 2006).

5.3 Assumptions of mechanical properties of ribs in FEM

In the THUMS model rib bone is considered homogeneous, isotropic, linear elastic with plastic zone and viscoplastic.

Ref	Subject	Test	Specimen	E [GPa]	σ_{ult} [MPa]	ε_{ult}	Def [mm]	K [N/mm]	F_{max} [N]
Granik and Stein (1973)	15 cadavers	3 point bending	Rib specimen	11.5	106	0.41 cm			
Got et al (1975)	34 cadavers (24-94 years old)	3 point bending	Rib specimen	Stat.: 7.807±4.05	Stat.: 109±61		Stat.: 6.23±2.84 ; Dyn.: 4.62±1.13	Stat.: 154.8±86	Stat.: 192.2±95.2; Dyn.: 117.8±58.5
Sacreste et al (1981)		3 point bending	Rib specimen	6.14±4.26	86±55				
Cesari and Bouquet (1981)	6	3 point bending	Rib specimen				3.30±0.82		210±134
Yoganandan and Pintar (1998)	30 cadavers (29-81 years old)	3 point bending	Rib specimen	2.32	188.6				
Kallieris (2000)	11 cadavers (20-70 years old)	3 point bending	Rib specimen	10.113±4.529; 12.872±3.421; 9.561±2.431	110±59; 287±72; 206±77		Stat.: 3.7±1.2		2 m/s: 569±92; 4 m/s: 460±110
Kimpara et coll. (2003)	70 males 26 females	3 point bending	Rib specimen	F: 7.57±5.44; M: 7.21±5.94				F: 44.3±27.3 ; M: 78.2±58.7	F: 149±79; M: 216±107
Cornier et al (2005)	4 cadavers	3 point bending	Rib specimen	Ant.: 7.51; Lat.:11.9; Post.:10.7 Average:17.7	Ant.: 116.7; Lat.:153.5; Post.:127.7 Average:135.4	Average : 1.38 %			
Charpail (2005)	6 cadavers (54-73 years old)	3 point bending	Whole rib	Static:9; Dynamic:11; Ant:7.51; Med:11.9; Post:10.7; Average:12.72	Static:110; Dynamic:250; Ant:117; Med:153; Post:128 Average:179		4.9	59	216

Figure 20: Literature review on mechanical properties of rib bone

Ref	Subject	Test	Specimen	E [GPa]	σ_{ult} [MPa]	ε_{ult}	Def [mm]	K [N/mm]	F_{max} [N]
Charpail (2005)	5 cadavers (58-70 years old)	Lateral compression	Whole rib	~13	150				
Rumelhart et comm. (1987)		Compression	Rib specimen	9.32-50.6	27-197				
Kallieris (2000)		Compression	Rib specimen	2.7	105.3				
Ashman et al (1984)		Continuous wave acoustic technique	Cortical specimen	Longitudinal: 20 Transverse: 13.4					
Stitzel et al (2003)	4 cadavers (61-71 years old)	3 point bending	Small cortical bone coupons	Ant.: 7.51; Lat.:11.9; Post.:10.7	Ant.: 116.7; Lat.:153.5; Post.:127.7				
Kemper et all. (2005)	6 cadavers : 3 males and 3 females (18 – 67 years old)	Traction	Cortical specimen	13.96±3.76	124.2				

Figure 21: Literature review on mechanical properties of rib bone

5.4 Experimental test procedure and results to determine material properties:

Tensile tests on PMHS (Kemper et al. 2005) - To get more realistic results as possible, it has been sought to compare the simulation test with a real test with cadavers. As previously described, the tensile test is a more reliable test to evaluate the material properties of rib cortical bone. Therefore, the results from tensile tests were used as a basis for comparison. The tensile tests used in this project correspond to the tests conducted by Kemper et al.

Cadaver	Gender	Age	Global BMD
1	Female	64	89.2
2	Male	45	81.4
3	Male	67	105.4
4	Female	61	122.3
5	Female	46	93.7
6	Male	18	138.3

Figure 22: Osteogram data for cadavers used in rib cortical bone testing

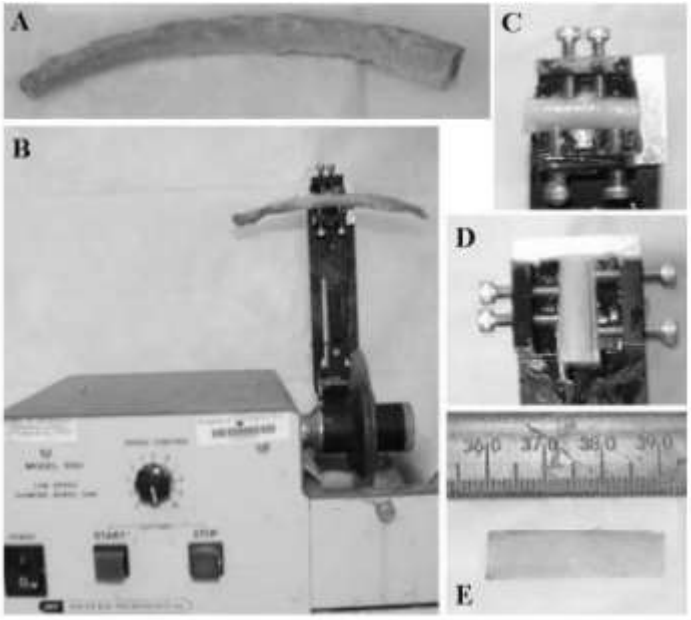

Figure 23: Rib bone testing

A) Anterior, lateral and posterior sections were cut from cach rib of the cage. B) Rib sections were placed in a bone chuck and mounted to the low speed diamond saw. C) Specimen were cut to the final specimen length. D) Two parallel cuts were made on the exterior side along the axis of the rib to obtain the final specimen width. E) Rib coupon cut to final dimensions and ready for milling.

The proper specimen hydration was maintained at all times during preparation and testing. The tissue and periosteum were removed from the bone surface.

Test configuration - A high-rate servo-hydraulic Material Testing System (MTS) machine was used to apply tension loads to failure (Figure 10). The tension tests were run using displacement control. Using MTS and the custom designed slack adapter and grips, the coupons were pulled in tension beyond the point of failure at a target rate of 0.5 strains/s. This strain rate used by Kemper in his test corresponds to the average strain rate resulting from dynamic seat belt loading of the rib cage.

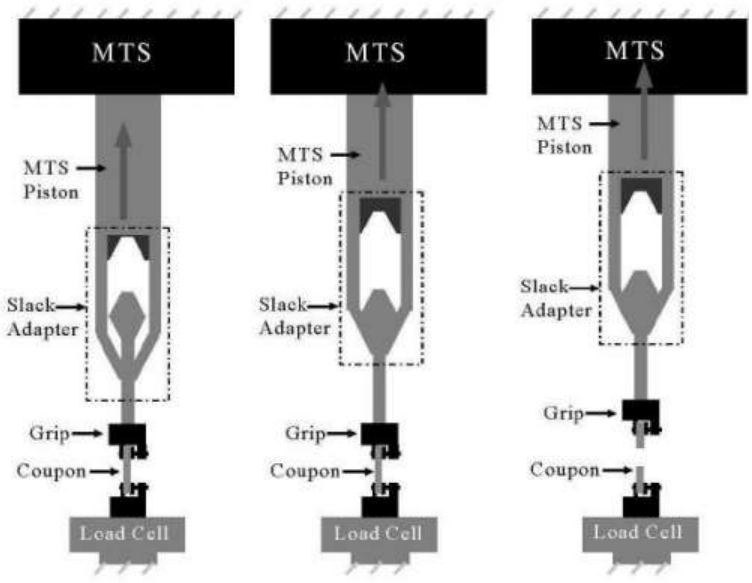

Figure 24: Illustration of the slack adaptor: as the MTS shaft moves upward (left), the slack adapter is engaged (middle) and pulls the bone coupon to failure (right)

5.5 Material properties obtained through Kemper tests:

	E [GPa]	σ_{yield} [MPa]	ε_{yield} [%]	σ_{ut} [MPa]	ε_{ut} [%]
All cadavers	13.9	93.9	0.88	124.2	2.71
All cadavers but 18 year old	14.8	101,9	0.89	129.3	2.27
All male cadavers	12.9	88.2	0.88	120.0	3.06
Older male cadavers (45-67)	14.6	101.3	0.89	134.1	2.38
18 year old male cadaver	9.8	67.2	0.87	106.3	4.24
All female cadavers	15.2	102.7	0.89	129.8	2.23
Older female cadavers (61 and 64)	14.8	101.9	0.89	129.3	2.27

E = Elastic modulus

Σ yield = Yield stress

ε yield = Yield strain

σ ut = Ultimate stress

ε ut = Ultimate strain.

Figure 25: Material properties of human rib cortical bone of PMHS used in Kemper´s

5.6 FEA simulation in LS-DYNA

In the THUMS model, the ribs are simulated as a shell for the cortical bone and as a solid element for the trabecular bone. One the left side of the specimen displacement and rotation in X, Y & Z directions were restricted. In the right side of the specimen was imposed a displacement in X direction. The strain rate is the same imposed by Kemper in his test, a displacement of 0.5 strains/s (5 mm/s).

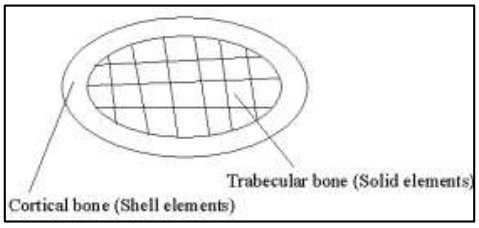

Figure 26: Model of the rib cross section of the THUMS model

5.7 Material properties used in several FE simulations:

Ref	Author	Model	E [GPa]	E_t [GPa]	σ_{yield} [MPa]	ε_{yield} [%]	σ_{ut} [MPa]	ε_{ut}
[12]	Furusu et al (2001)	THUMS	11.5		73.7	0.64	105.9	2.04 %
[12]	TNO Automotive (2003)	MADYMO FE human model	19.0		73.0	0.38		
[12]	Zhao and Narwanil (2005)	Total Human Body Model	10.2		65.3	0.64		
[12]	Ruan et al (2003)	Full Human Body FEM (Ford)	11.5					
[31]	Z. Li et al (2009)	Simulation of anteroposterior solicitation	11.5	1.15	88			0.02
[13]	Charpail	Simulation of anteroposterior solicitation	13		150		150	10%
	THUMS model		13	0	93.5		150	

E = Elastic modulus

Et = Tangent modulus

σyield = Yield stress

ε yield = Yield strain

σut = Ultimate stress

ε ut = Ultimate strain

Figure 27: Material properties of human rib cortical bone of different FEM models

5.8 Material type:

The rib cortical bone specimen was simulated with Piecewise linear plasticity material. With Piecewise linear plasticity material, it can be defined an elasto-plastic material with an arbitrary stress versus strain curve and arbitrary strain rate dependency. The stress strain behavior may be treated by a bilinear stress strain curve by defining the tangent modulus. This material includes two attributes: Strain-rate effects and failure criteria.

Piecewise linear plasticity material is an isotropic material and it is used for applications as a metal and plastic (LSDyna, 2018).

CORTICAL BONE OF RIB	
Material type	Piecewise Linear Plasticity
ρ (ton/mm3)	2 exp -09
E (MPa)	13000
υ	0.3
σ_Y (MPa)	93.5
E_t (MPa)	0
Fail	0.018
C	360.70001
P	4.605
ε_1	0
ε_2	0.007154
ε_3	0.0018462
σ_1 (MPa)	93.5
σ_2 (MPa)	128
σ_3 (MPa)	150

ρ = Mass density

E = Young´s modulus

υ = Poisson´s ratio

σY = Yield stress

Et = Tangent modulus

Fail = Failure flag

C = Strain rate parameter

P = Strain rate parameter

ε 1 = First effective plastic strain value

ε 2 = Second effective plastic strain value

ε 3 = Third effective plastic strain value

σ1 = Corresponding yield stress value to ε 1

σ2 = Corresponding yield stress value to ε 2

σ3 = Corresponding yield stress value to ε 3

Figure 28: Simulation parameters of rib specimens

5.9 Mesh Element Size:

The cortical bone has been simulated like a shell. And it has been simulated using different mesh sizes to choose the most appropriate element size. The two parameters used to choose the element size were convergence and simulation time. The simulation has been done in Ls Dyna with Piecewise linear plasticity material type and under integrated shell elements (integration with one point).

Mesh size (mm)	Number of elements	Thickness (mm)	Element size/Thickness	Energy at rupture (mJ)	Break time (s)	Ncpu	Time of simulation
2.5	4	0.3	8.33	41.5922	0.086001	1	9 sec
1	25	0.3	3.33	31.5538	0.073801	1	1 min 3 sec
				32.3537	0.074901	2	
0.5	100	0.3	1.67	51.239	0.099801	1	6 min 48 sec
				51.4306	0.099901	2	
0.4	156.25	0.3	1.33	47.8332	0.097101	1	17 min 38 sec
				47.6853	0.099901	2	
0.3	277.78	0.3	1	46.0763	0.119901	1	26 min 17 sec
				45.7188	0.119901	2	
				46.2217	0.119901	4	
0.2	625	0.3	0.67	42.7787	0.090201	1	1 h 4 min 5 sec
				43.5061	0.091201	2	
				43.5024	0.091201	4	
0.1	2500	0.3	0.33	41.6462	0.088101	1	10 h 8 min 16 sec
				42.0234	0.088601	2	
				42.5526	0.089301	4	

Figure 29: Properties of simulation of different meshes

Energy at rupture and the break time respectively for the different meshes simulated.

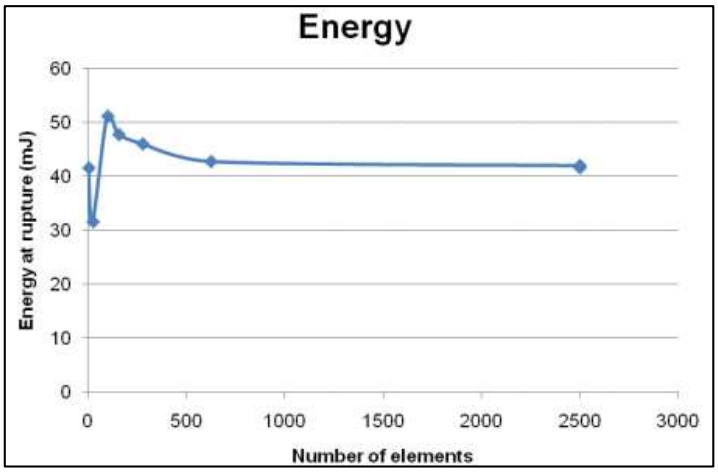

Figure 30: The energy at rupture for different meshes.

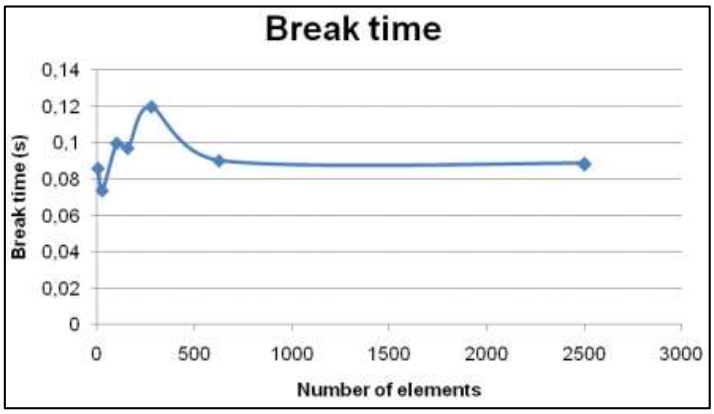

Figure 31: The break time for different meshes.

The breaking energy and the rupture moment are stabilized for an element number of 625 that corresponds with an element size of 0.2 mm. So, the simulation has been done with an element size of 0.2 mm.

As the specimen is simulated like a shell, the element size (0.2 mm x 0.2 mm) is smaller than its thickness (0.3 mm). It was thought that there could be problems due to the size-thickness ratio, so simulations were performed with solid elements and shell elements to see if it influenced. A specimen was simulated using solid elements with an element size of 0.2 mm x 0.2 mm and a thickness of 0.15 mm. Figure below shows stress – strain curves of shell and solid specimen taking into account the strain rate effect in the piecewise plasticity material type. The difference may be due to the different ways to calculate the deformation in solid and in shell elements.

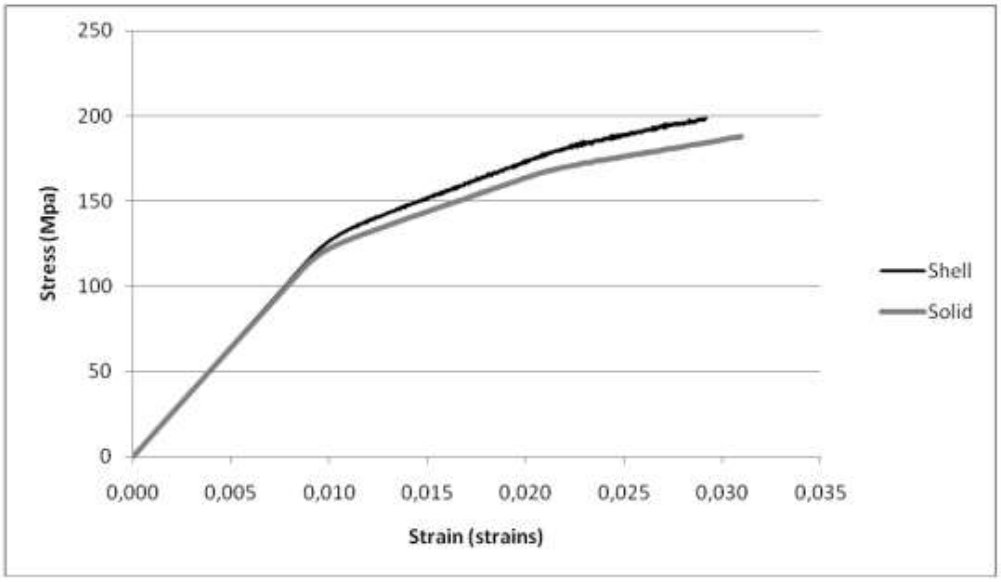

Figure 32: Stress-Strain curve for shell specimen and solid specimen with strain rate

Stress – strain curves below of shell and solid specimen without taking into account the strain rate effect. There is no difference between them when the strain rate effects are not considered.

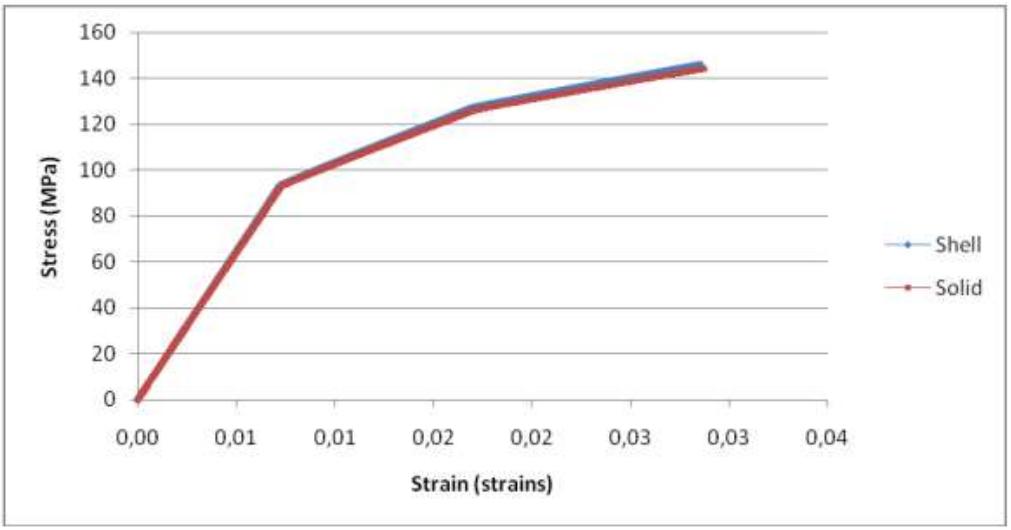

Figure 33: Stress-Strain curve for shell specimen and solid specimen without strain rate

From these results, it was decided to work with a specimen simulated by shell elements (size of 0.2 mm x 0.2 mm and thickness of 0.3 mm) because its simulation time is approximately the half than this in the solid, and because in the THUMS model the cortical bone is simulated like a shell.

5.10 Results:

The force in axial direction, F_x, was measured with Ls-Dyna in the restricted set node (nodes in the left) to calculate the stress. Also the displacement of two nodes was measured (X1 and X2) to calculate the specimen deformation.

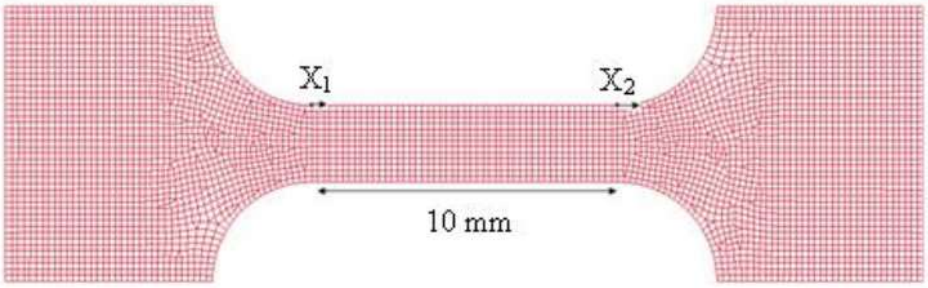

Figure 34: The specimen simulated in Ls Dyna.

5.10.1 Stress – Strain curves:

Engineering stress and Engineering strain equation:

$$\sigma = \frac{F}{A}$$

Where:

σ is stress

F is force

A is cross sectional area

Figure 35: Formulation for engineering stress

$$\varepsilon = \frac{\Delta L}{L}$$

Where:

ε is the strain

ΔL is the change in length

L is the original length

Figure 36: Formulation for engineering strain

True stress and strain equation:

$$\varepsilon_{true} = \ln(1+\varepsilon_{eng})$$

Figure 37: Formulation for true strain

$$\sigma_{true} = \sigma_{eng}(1+\varepsilon_{eng})$$

Figure 38: Formulation for true stress

The yield stress defined for the cortical bone was 93.5 MPa and taking into account the strain rate parameters defined in THUMS, the yield stress was 115.89 MPa.

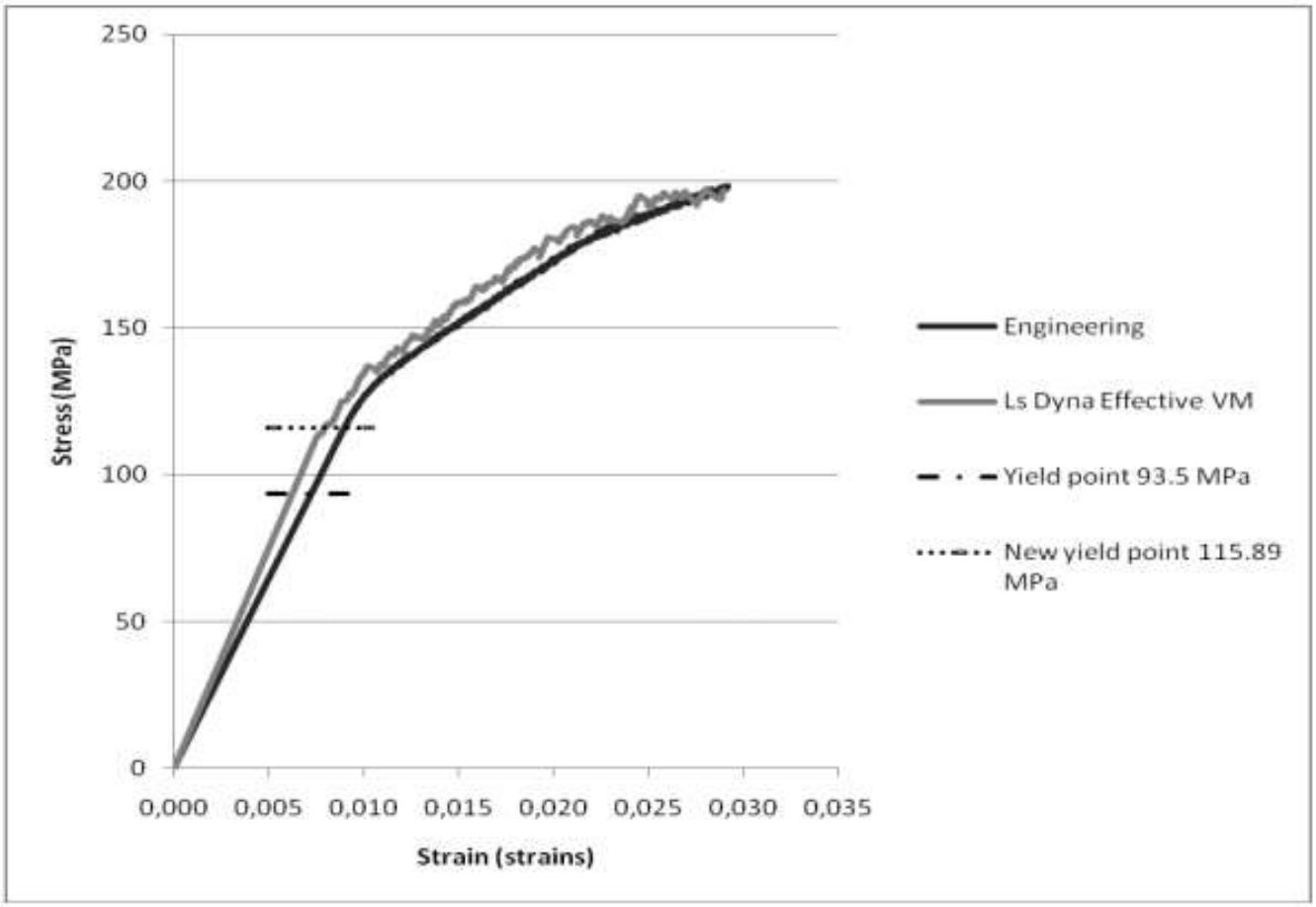

Figure 39: Engineering stress - strain curve and effective stress - strain curve with strain rate curves

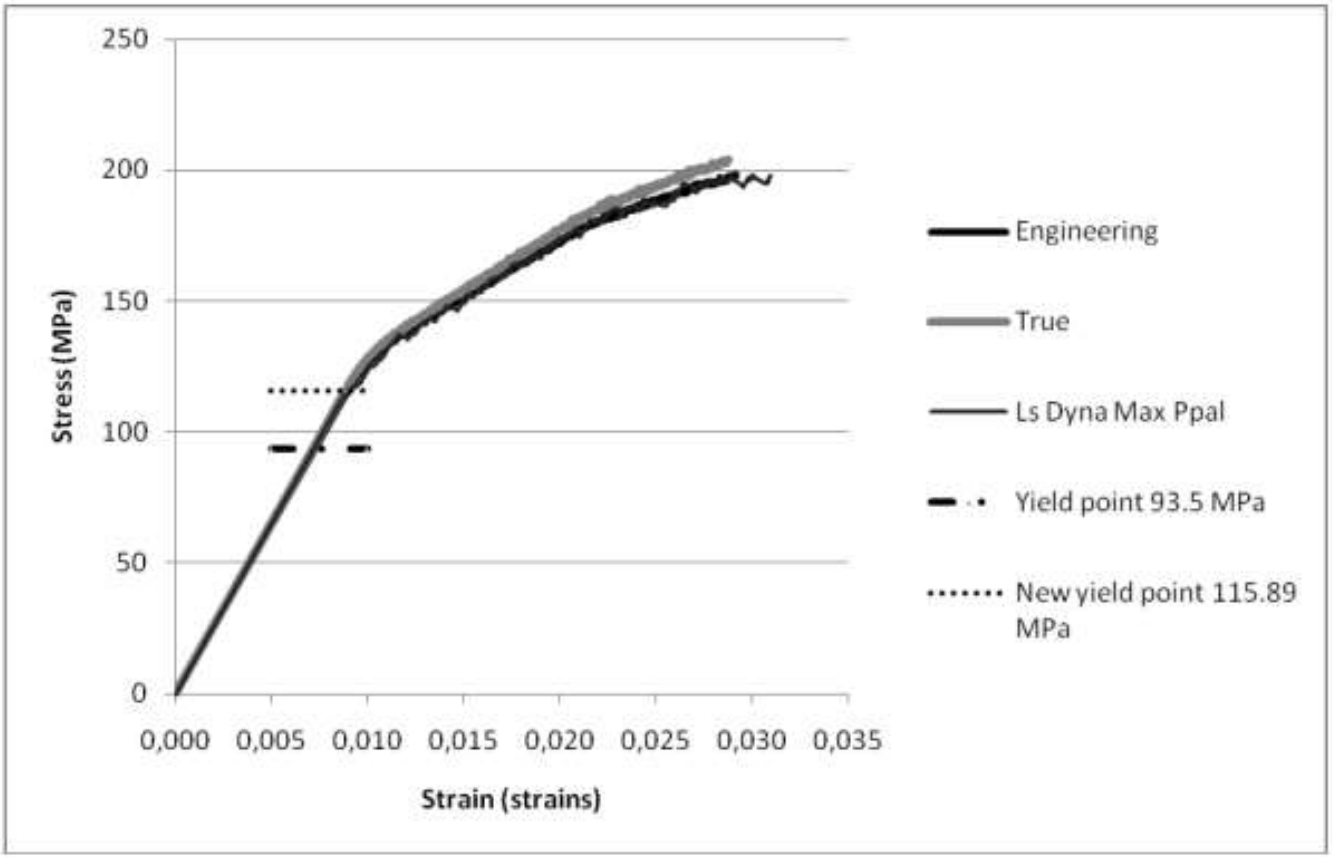

Figure 40: Engineering stress - strain curve, true stress - strain curve and maximum

Stress strain curves without taking into account the stress strain parameters:

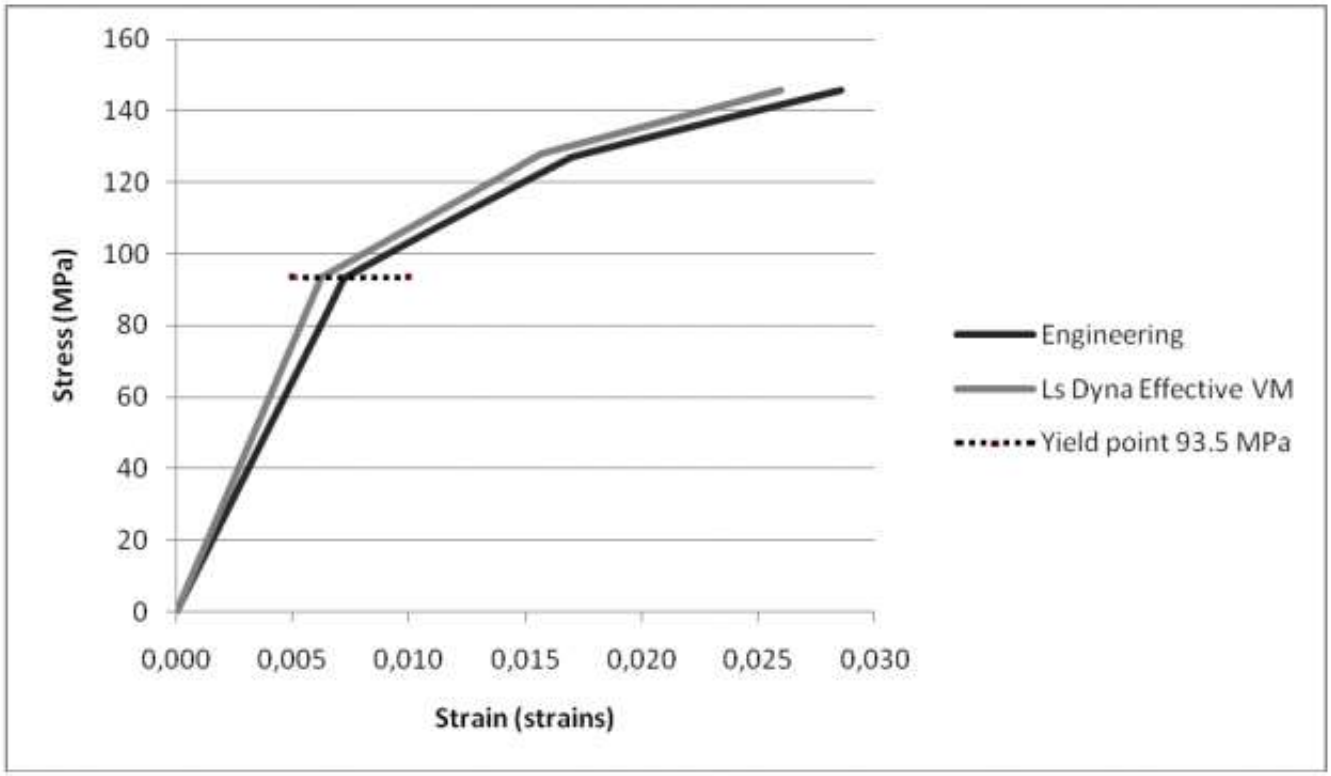

Figure 41: Engineering stress - strain curve and effective stress - strain curve without strain rate factors.

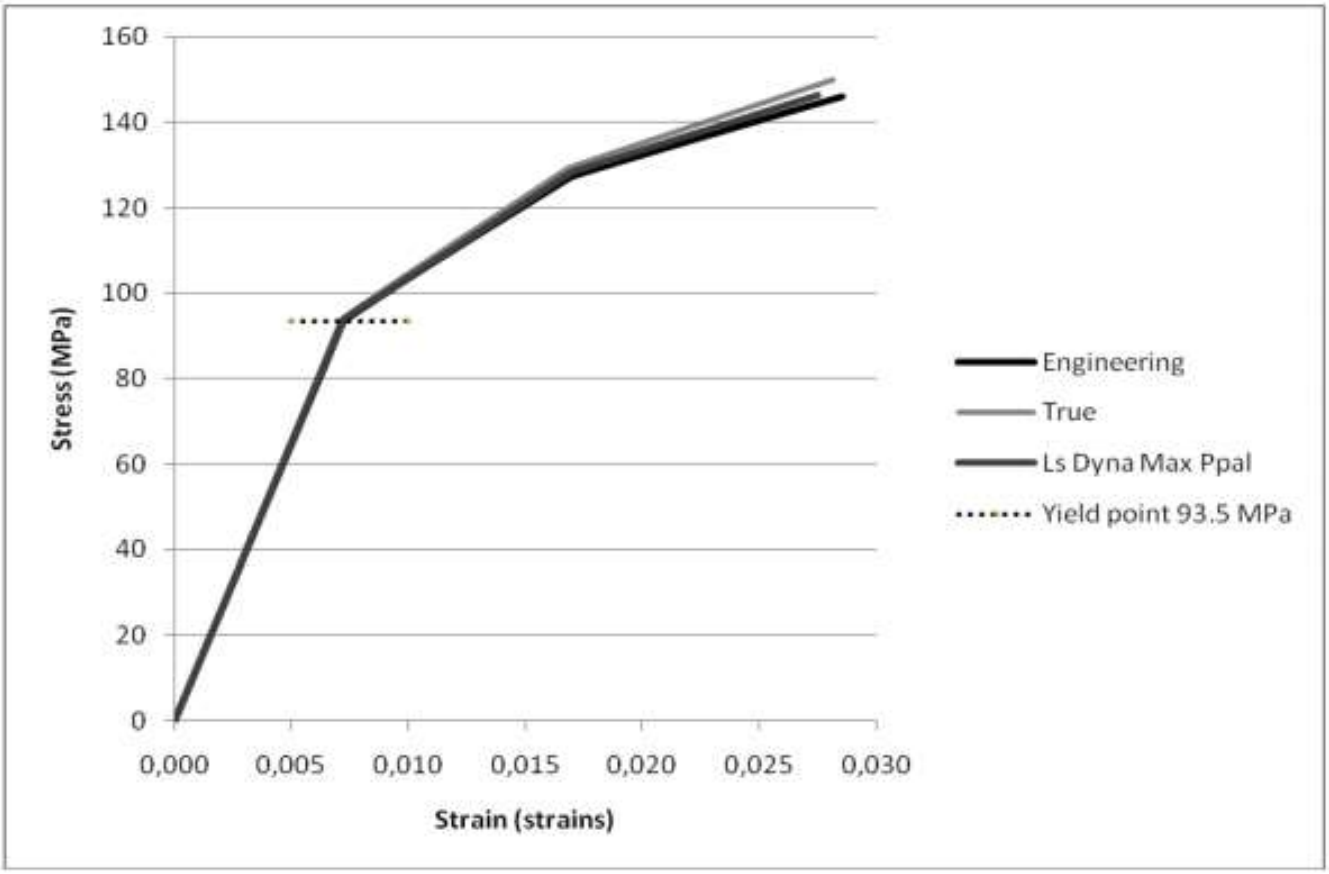

Figure 42: Engineering stress - strain curve, true stress - strain curve and maximum principal stress - strain curve without strain rate factors.

5.10.2 Influence of stain rate:

Ls Dyna has into account strain rate effects. Specifically, for the piecewise linear plasticity the relation is as follows [32]:

$$\beta = 1 + \left(\frac{\dot{\varepsilon}}{C}\right)^{1/p}$$

Figure 43: Formulation for β parameter

$$\sigma'y = \beta \cdot \sigma y$$

Figure 44: Formulation for yield stress with the influence of strain rate

Where:

C: Strain rate parameter

P: Strain rate parameter

$\dot{\varepsilon}$: Strain rate

σ_Y: Yield stress

σ'_Y : Yield stress with the influence of strain rate

Results with C = 360.70001, P = 4.605

For THUMS model, with C = 360.70001, P = 4.605 and σY = 93.5 MPa, the strain rate effect is remarkable in the yield stress.

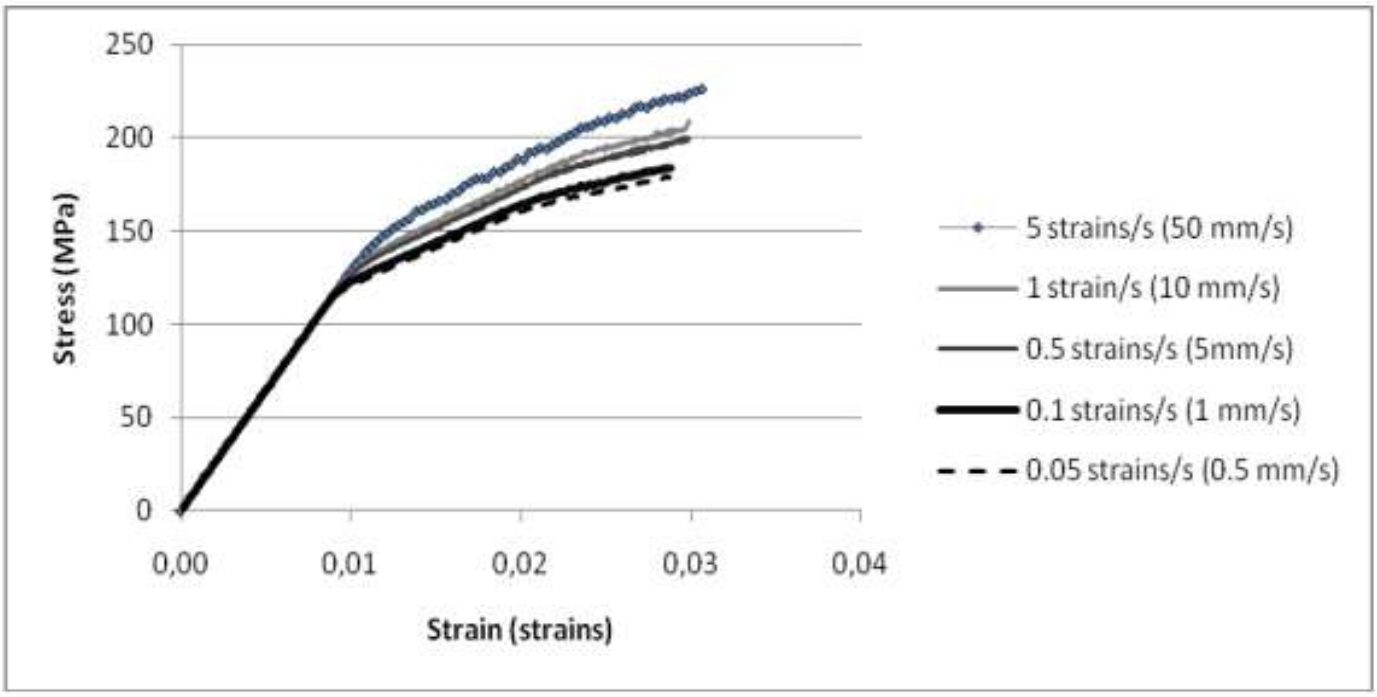

Figure 45: The effect of the strain rate in the stress – strain curve for C = 360.70001 and P = 4.605

Taking into account the effect of the strain rate, the higher is the strain rate, higher is the yield stress and higher is the ultimate stress. This agrees with two tensile test realized with bovine femur and tibia, where the authors concluded that the yield stress increase with the strain rate [30].

Results with C = 0 and P = 0

In Ls Dyna, when C and P parameters are cero, the strain rate effect is not taken into account.

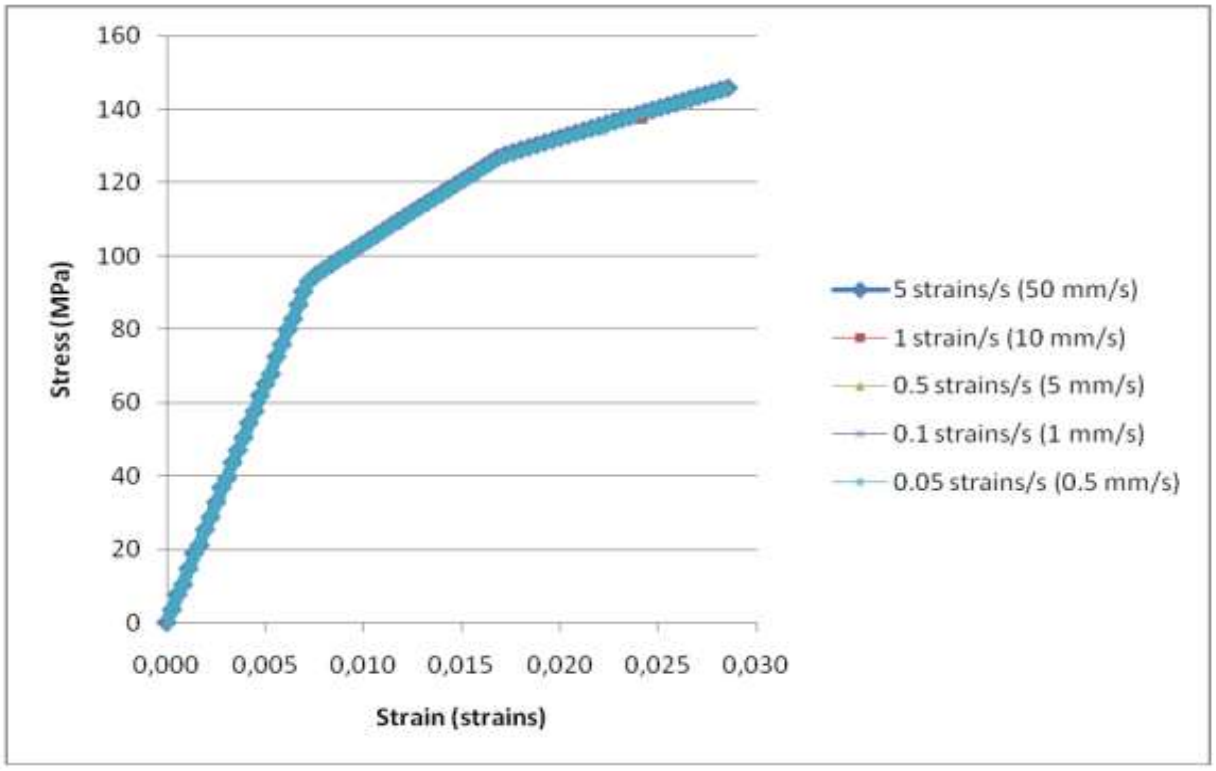

Figure 46: The stress – strain curve for different strain rates without taking into account the strain rate parameters

If the strain rate parameters aren´t take into account, the stress – strain curve don´t change for different velocities of displacement.

5.10.3 Comparison with experimental and simulated results:

The simulation of cortical bone of rib, with a shell with element size of 0.2 mm x 0.2 mm, and strain ratio of 0.5 strains/s has been compared with the results obtained experimentally by Kemper. Table below shows the mean values of elastic modulus, ultimate stress and ultimate strain obtained by Kemper for all cadavers. With these values, a range was determined.

	E [MPa]	σ_{ut} [MPa]	ε_{ut} [strains]
All cadavers	13960 ± 3760	124.29 ± 32.45	0.02685046 ± 0.01390781

Figure 47: The mean value of material properties of all cadavers

Taking into account the strain ratio, with C = 360.70001 and P = 4.605 the result of simulation overestimate the ultimate stress obtained by Kemper. The curves aren´t in the range obtained by Kemper.

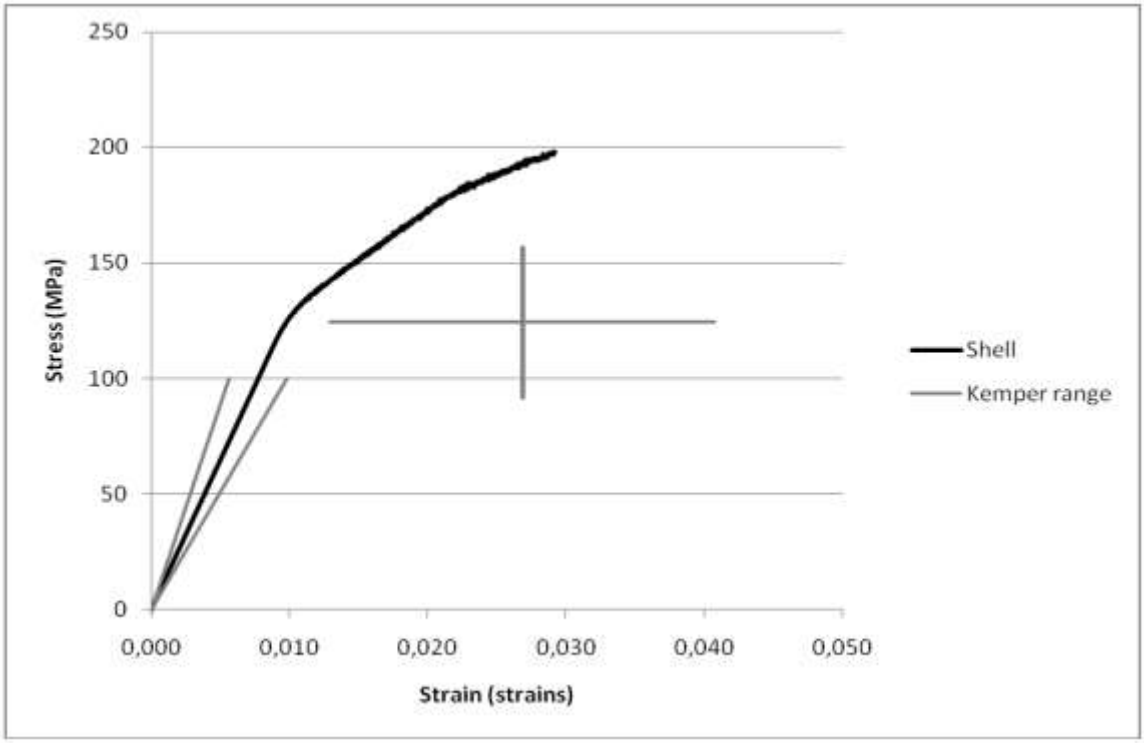

Figure 48: Engineering stress – strain curve with C = 360.70001 and P = 4.605

can be because of the values de C and P are too big. Maybe for a strain rate of 0.5 strain/s it´s not necessary to take into account the strain ratio for a dynamic load. It can be seen that without taking into account the influence of the strain ratio, with C = 0 and P = 0, the curves are similar to these obtained experimentally. They are inside de values given by Kemper in the image below.

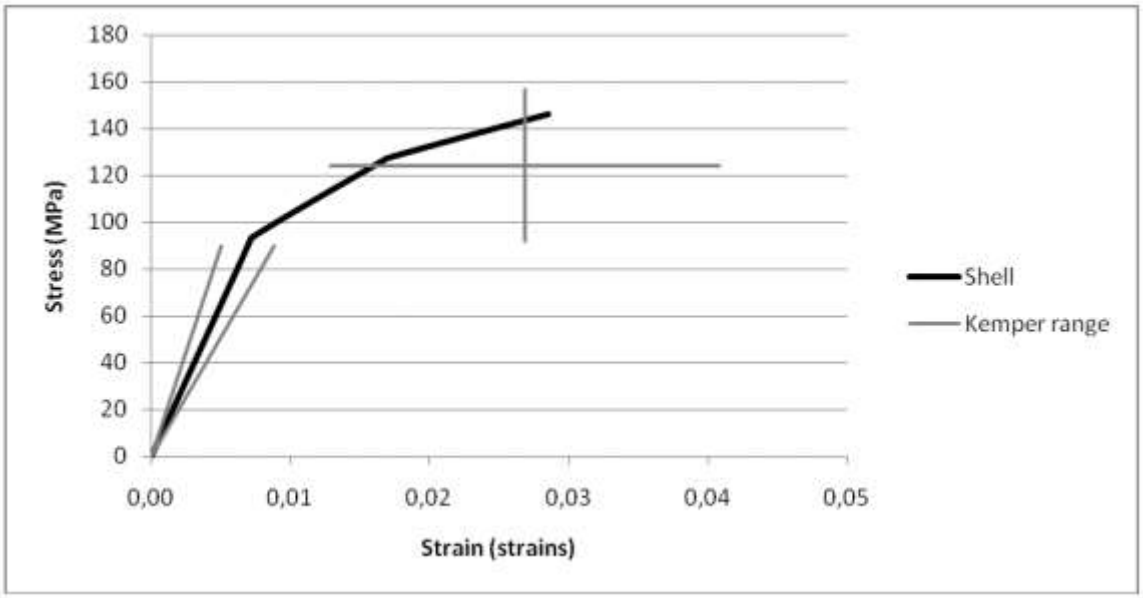

Figure 49: Engineering stress – strain curves with C = 0 and P = 0

The simulation done in Ls Dyna has mechanical values of a man of 30 - 40 years old. The range given by Kemper was done with the average values of six cadavers from 18 to 67 years old. The values are experimental values, but, cannot be affirmed to be significant enough to generalize, because of the low number of PHMS analysed and the significant differences due to the age.

5.11 Conclusion:

- The rib cortical bone specimen was simulated with Piecewise linear plasticity material
- The internal energy and the rupture moment are stabilized for a shell element size of 0.2 mm x 0.2 mm.
- Shell element of 0.2 mm x 0.2 mm with a thickness of 0.3 mm and two layers of solid elements of 0.2 mm x 0.2 mm with a thickness of 0.15 mm have the same stress-strain curve if the strain rate parameters are not taken into account. So, if the strain rate parameters are not taking into account, the ratio element size/thickness for a shell element used in these simulations does not affect the results.
- Taking into account the effect of the strain rate, with the Ls Dyna definition included in the material Piecewise linear plasticity, the higher is the strain rate, higher is the yield stress.
- If the strain rate parameters aren´t taken into account, the stress-strain curve don´t change for different velocities of displacement.
- The effective plastic strain over time is different if the strain rate parameters are taken into account or not. If the strain rate parameters are taken into account, it will take longer to break.
- Taking into account the strain ratio, with C = 360.70001 and P = 4.605, the stress-strain curves aren´t in the range obtained experimentally by Kemper.
- Without taking into account the influence of the strain ratio, with C = 0 and P = 0, stress-strain curves are similar to these obtained experimentally. They are inside the values obtained by Kemper.

6. FEA Analysis of human skull: (Paper focus: Human skull material comparison based on strain parameters)

The main aim of this project was to develop a model for predicting skull fractures of a 50th percentile male, using a finite element head model developed at the Neuronics department of KTH, Royal Institute of Technology. The skull bone is modeled skull bone. Due to the coarse mesh of the FE head model the material model was not allowed to include any erosion, deleting element as they reach their ultimate strain. With these requests, two materials from the LS-DYNA material library seemed appropriate: **material 81, MAT_PLASTICITY_WITH_DAMAGE and material 105 MAT_DAMAGE_2.**

To evaluate these materials and adjust the input parameters a dog bone FE model was developed and tension tests were simulated with this model, equivalent to tension tests performed on equally shaped skull bone specimens. The material simulating a behavior most similar to the behavior from the tension tests turned out to be material 81. This material model was then implemented in the full FE head model for further input parameter adjustment and validation. Four different cadaver experiments were simulated, with different impacting objects: sphere, box, cylinder and flat cylinder surface, and impacted areas of the head: vertex, temporo-parietal and frontal. The forces obtained in the simulations were compared to the forces of the cadaver experiments. The fracture prediction was based on the damage parameter, which could be plotted to visualize the areas where the ultimate strain was exceeded and thereby the area most likely to be fractured. This parameter was then compared to the documented fractures from the cadaver experiments.

The result showed that using material 81 with the input parameter EPPFR=0.05 gave the overall most accurate forces and fracture predictions. The breaking stress, σB, did not affect the fractures significantly but a reduced σB resulted in reduction of the peak forces. The thickness of the diploë did not have any significant impact on the fracture occurrence, but a thinner diploë had a reducing impact on the peak forces as well.

6.1 Method:

The main method for this project has been to simulate different load setups on FE models of bone samples and full cadaver heads in the computer software LS-DYNA [6] and analyzing the results in LS-PrePost (J. Currey, 1984) and MATLAB (J. Wood, 1971).

6.2 Material models:

The cranial bone consists of three layers, where the inner layer of softer, porous bone is called the diploë and the two outer layers of stronger, compact bone are called tables. The material properties of the tables differ from those of the diploë, hence they need to be modelled using different material models.

In the original model, the diploë was modeled as solid elements, with the material model MAT_ISOTROPIC_ELASTIC_PLASTIC, a Young's modulus of 1 GPa and a yield stress of 32.7 MPa. Failure of the stiffer tables are assumed to result in skull fractures, since if the tables are broken the diploë is likely to be ruptured as well,

hence no focus was devoted adjustments of material model or input parameters of the diploë. The impact of the diploë thickness was investigated in the frontal impact simulations since this thickness of the FE head model differed from the measured diploë of the cadaver heads in some of the experiments.

For the compact bone, two LS-DYNA material models were investigated to find the most appropriate for simulating the behavior of compact bone. Due to the coarse mesh and the requirement to maintain the energy balance of the FE model, the material models could not include any erosion, deleting elements as they ruptured. Instead, the material had to include a damage parameter, softening the material as it began to yield. The load carrying ability was assumed to decrease rapidly as the material failed. Two material models were found in the LS-DYNA material library, which seemed to meet these request. They were material 81 (MAT_PLASTICITY_WITH_DAMAGE) and material 105 (MAT_DAMAGE_2). Material 81 calculated the damage parameter from the plastic strain, according to equation (European road safety observatory, 2012).

$$D = \frac{\varepsilon_{eff}^{p} - \varepsilon_{failure}^{p}}{\varepsilon_{rupture}^{p} - \varepsilon_{failure}^{p}}$$

Here ε_{eff}^{p} is the plastic strain in the material, $\varepsilon_{failure}^{p}$ is the plastic strain where the material begins to fail and $\varepsilon_{rupture}^{p}$ is the plastic strain where the material ruptures. $\varepsilon_{rupture}^{p}$ is the parameter adjusted to gain a rapid decrease of the load carrying ability, and is referred to as EPPFR hereafter.

Material 105 calculated the damage parameter from the plastic strain using the equation, shown below.

$$\dot{D} = \frac{Y}{S(1-D)}\dot{r}$$

Here, D is the evolution of the damage parameter D, Y is the strain energy release rate, a function of the Young's modulus and Poisson's ratio. S is a pre-set constant and r is calculated according to equation (S. Kleiven, 2002) below,

$$\dot{r} = \dot{\varepsilon}_{eff}^{p}(1-D)$$

where ε_{eff}^{p} is the accumulation of effective plastic strain. The input parameters S and EPPFR were adjusted to gain a material behavior representing the behavior of compact cranial bone. For each material model those parameters were the ones that could not be determined by using the data from the experiment by Wood et al (R. P. Hubbard, 1971). For both materials the Young's modulus, density and Poisson's ratio were inserte8d along with the tabulated effective plastic strain with its corresponding yield stress.

PARAMETER	LS-DYNA VARIABLE	VALUE							
Young's modulus [Pa]	E	1.71e+10							
Density [kg/m3]	RO	2009							
Poisson's ratio	PR	0.22							
Plastic strain	ESP1-8	0.0	6.46e-5	1.108e-4	1.847e-4	2.678e-4	3.555e-4	4.294e-4	0.1
Corresponding yield stress [Pa]	ES1-8	4.492e+7	5.768e+7	6.484e+7	6.993e+7	7.486e+7	7.931e+7	8.201e+7	8.201e+7
Plastic strain	ESP1-8	0.0	6.130e-5	6.230e-5	1.236e-4	1.505e-4	1.898e-4	2.290e-4	0.1
Corresponding yield stress [Pa]	ES1-8	5.158e+7	5.575e+7	5.947e+7	6.364e+7	6.765e+7	6.959e+7	7.152e+7	7.152e+7

Figure 50: Input parameters in LS-DYNA material cards for material 81 and 105, for modelling of compact bone

Row 5 and 6 represents the EPS and ES values for σB =82 MPa and row 7 and 8 represents the EPS and ES values for σB=71 MPa.

To test the material behavior and adjust the relevant input parameters, a FE model of a tension test sample in the shape of a dog bone was developed, with a fairly coarse mesh to replicate the mesh of the skull model as far as possible.

The left edge of the structure was constrained in all directions and a load was applied in the x-direction on the right edge of the dog bone to result in a strain rate in the four middle elements of approximately 10 s-1 . Both material 81 and 105 were tested and adjusted to fit the material behavior from the experiment. For material 81 the variable varied was EPPFR with the values 0.1, 0.05 and 0.01, and for material 105 the varied variable was S with the values 10 000 and 25 000. A smaller mesh where the element size of the waist of the model was approximately 0.36*0.63 mm, equal to the half of the original mesh size, was also tested and evaluated.

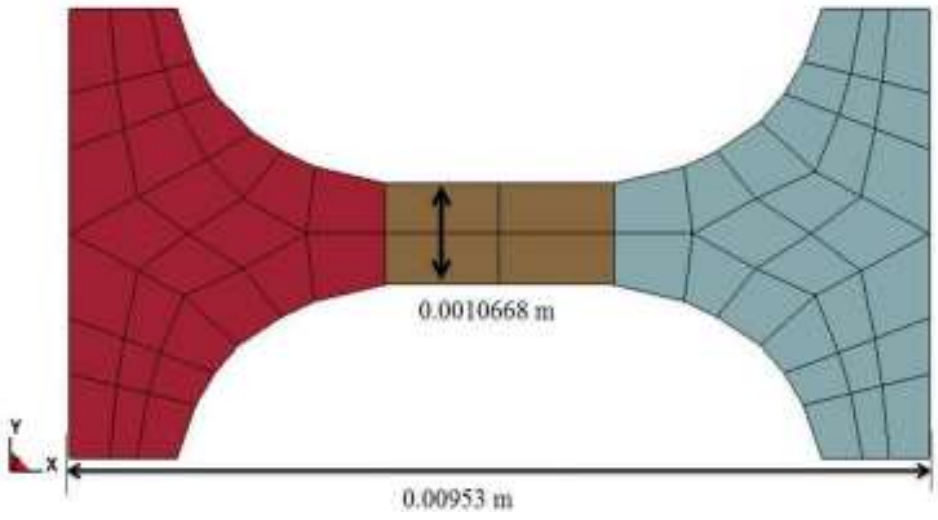

Figure 51: FE model of dog bone

6.3 Fracture prediction:

Both material models tested for compact bone included a damage parameter, stored in the LS-PrePost 3d binary plot under History Variable 1. This parameter ranged from 0-1, where 1 indicates an element where the ultimate plastic strain is exceeded. By extracting the output data of this variable the appearance of the fracture can be determined, and visualized by plotting its propagation over the skull bone.

6.4 Simulation Models:

To further investigate and adjust the input parameters of the material models a number of simulations of cadaver experiments were set up. To increase the applications of the model, a variation of impactors and impacted regions of the head were investigated. To validate the results from the simulations, cadaver experiments where the frontal bone and vertex were impacted by a sphere were simulated and results compared to the experimental results.

6.5 Simulation set ups for cadaver experiments:

- Temporo-Parietal Impact by Flat Surface (a)
- Frontal Impact by Cylinder (b)
- Frontal Impact by Flat Surface (c)
- Validation against Study of Vertex and Frontal Impact by Sphere (d & e)

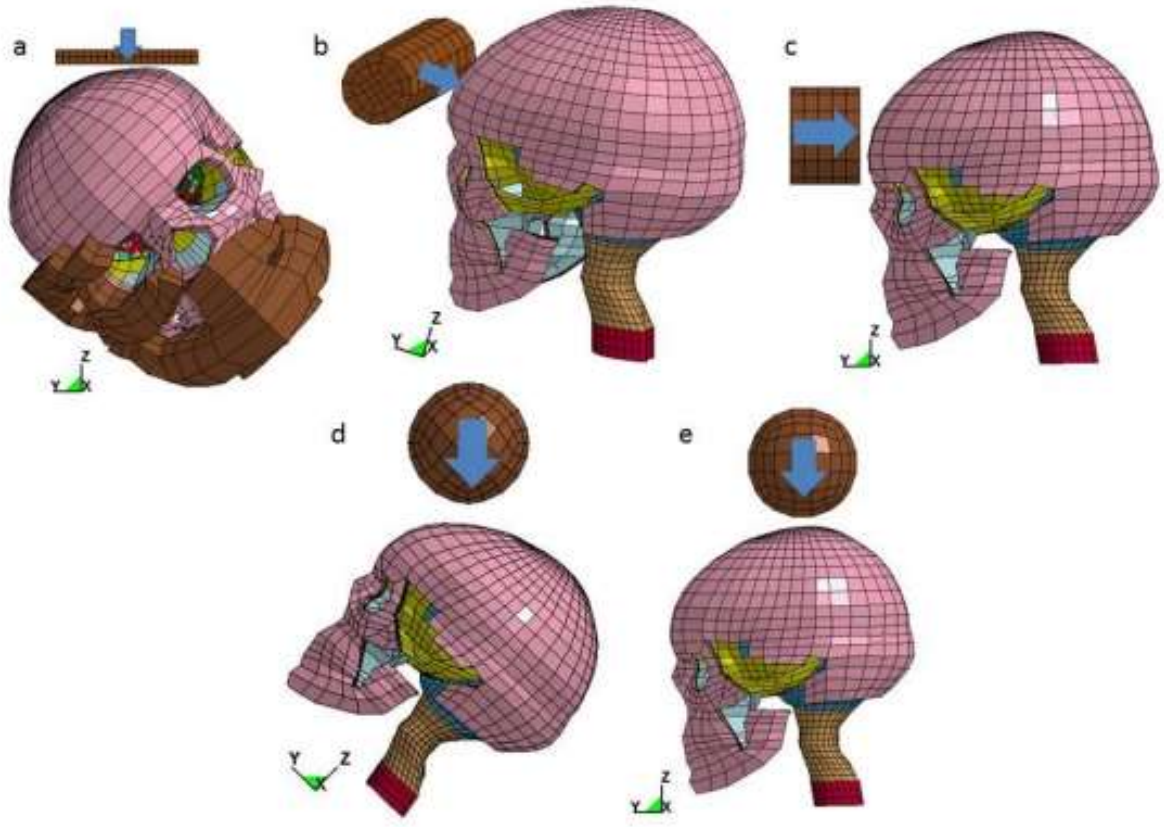

Figure 52: Simulation setups of the cadaver experiments.

6.6 Results:

The simulations of the dog bone were performed using both material models, with a variation of material parameters. The results of the simulations with σB=71 and σB=82 MPa are presented in the stress-strain plots in Figure 3. It was obtained that, for material 81, the lower EPPFR the faster was the drop of the load carrying ability, and the same could be obtained when varying the S value of material 105. Testing the two different material models and their input parameters resulted in material 81 with EPPFR = 0.01 and 0.05, as well as material 105 with S = 10 000 giving in the steepest slope of the curve after failure. It was also found that the element size had a small impact on the result of the stress strain relationship after failure. No changes were found on the trends of the curves for two evaluated σB.

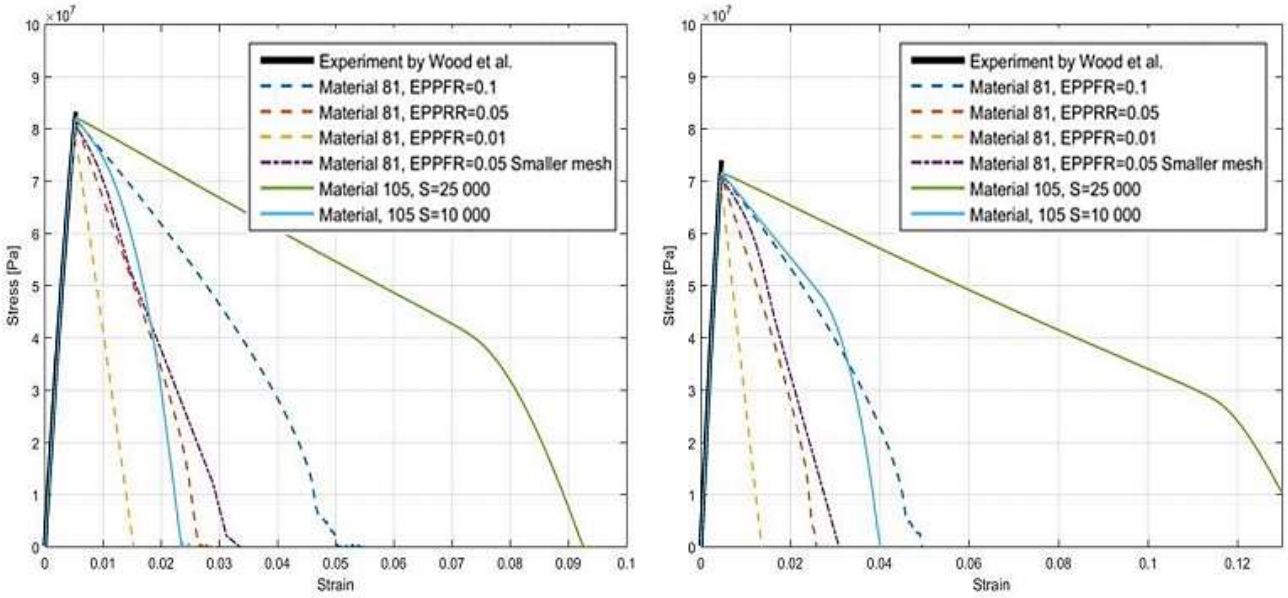

Figure 53: Result from simulation of tension test with dog bone FE model. Left image shows the result from simulations with σB=82 MPa and the right shows the result from the simulations with σB=71 MPa.

6.7.1 Temporo-parietal impact by flat surface

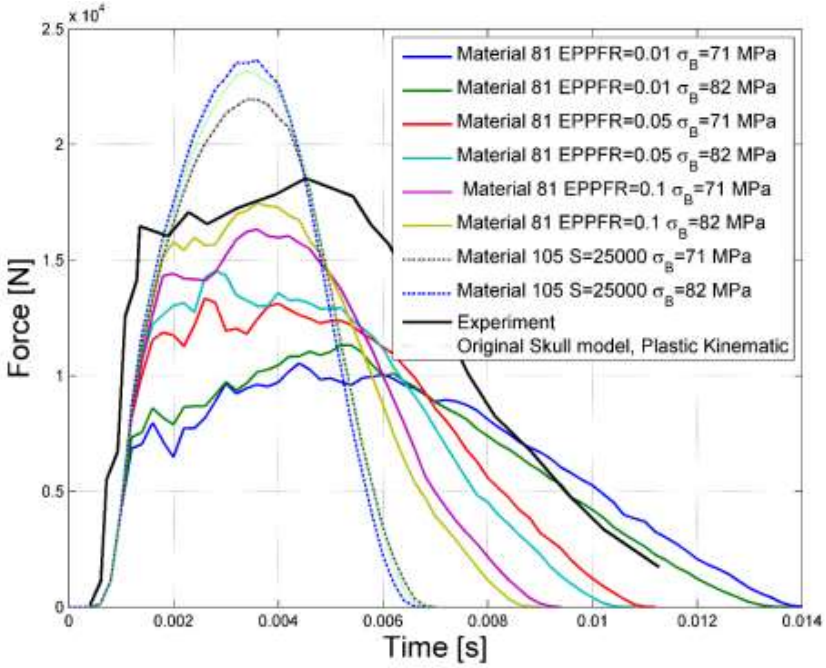

Figure 54: Force-time plot from simulations of temporo-parietal impact with flat surface.

For all simulations of material 81, no erosion was obtained and the force curve shows discontinuities around the peak of the curve, indicating fracture (J. W. Melvin, 1969), along with the trend of the curves following the experiment. The peak forces obtained in the cadaver experiments ranged from 5 800-17 000 N, an interval within which all forces obtained in the simulations with material 81 occurred. Since one of the request on the material models was to not include any erosion of elements and material 105 did for S=10 000, this material model was considered as too unstable due to the erosion which could not be avoided and therefore not used in the following simulations.

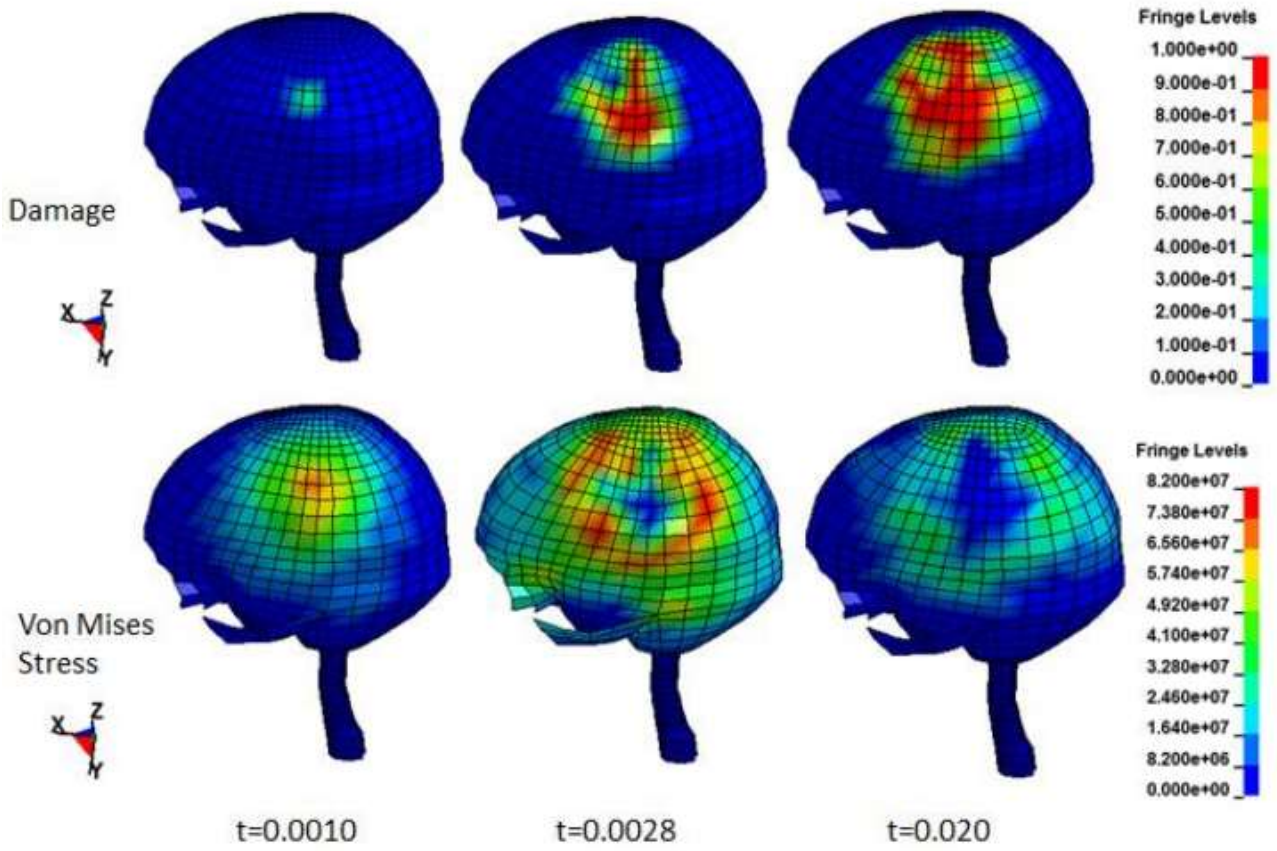

Figure 55: Plotted damage propagation and von Mises stress from simulation of the temporo-parietal impact, with material 81 and input parameter EPPFR=0.05 and σB=82 MPa.

The left column shows the result at the time where the failure starts, middle column shows the result at the time for the maximum force, right column shows the result at the end of the impact, where the impactor is no longer in contact with the head.

6.7.2 Frontal Impact by Cylinder

The frontal impact by a 4.5 kg cylinder gained higher forces than obtained in the cadaver experiment. The forces obtained in the simulations ranged between 10 500-22 140 N depending on input parameters and impact velocity, compared to the forces measured in the experiment ranging between 4225-7340 N. The bone thickness at impact site of the cadaver heads differed from the diploë thickness of the FE head model. Hence, the thickness of the diploë was scaled down by approximately 60% from 11.1 to 4.5 mm, with minor variations due to geometry. Results of the simulation is shown below for impact velocity 3.0 m/s and 3.5 m/s respectively.

GEOMETRY	σB [MPa]	EPPFR	MAX FORCE [N]	FRACTURE	REDUCTION [%]
Original diploë	71	0.01	14 540	Y	
		0.05	18 270	N	
		0.1	18 460	N	
	82	0.01	15 410	Y	
		0.05	18 710	N	
		0.1	19 040	N	
Scaled diploë	71	0.01	11 220	Y	22.8
		0.05	14 610	N	20.0
		0.1	15 110	N	18.2
	82	0.01	12 440	Y	19.3
		0.05	15 520	N	17.1
		0.1	15 730	N	17.4

Figure 56: Maximum force, fracture occurrence and force reduction due to diploë thickness reduction, at impact velocity 3.0 m/s

GEOMETRY	σB [MPa]	EPPFR	MAX FORCE [N]	FRACTURE	REDUCTION [%]
Original diploë	71	0.01	13 430	Y	
		0.05	18 140	Y	
		0.1	20 820	N	
	82	0.01	16 310	Y	
		0.05	20 860	N	
		0.1	22 140	N	
Scaled diploë	71	0.01	10 500	Y	22.8
		0.05	15 630	Y	14.9
		0.1	16 970	N	18.5
	82	0.01	12 170	Y	25.4
		0.05	16 900	Y outer, N inner	19.0
		0.1	17 980	N	18.8

Figure 57: Maximum force, fracture occurrence and force reduction due to diploë thickness reduction, at impact

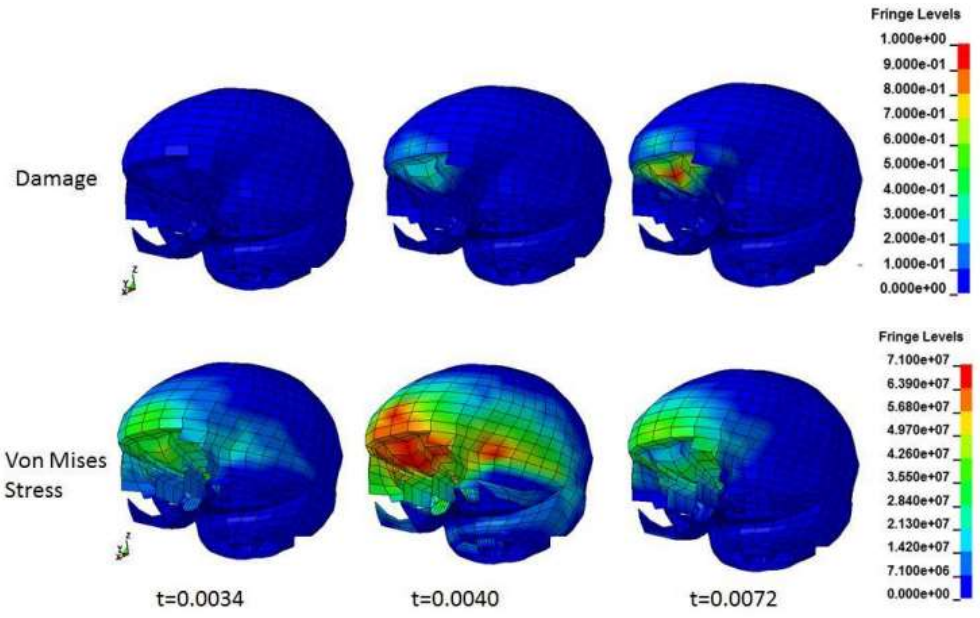

Figure 58: Plotted damage propagation and von Mises stress from simulation of the frontal impact by cylinder, with material 81 and input parameter EPPFR=0.05 and σB=71 MPa.

The left column shows the result at the time for initial contact, middle column shows the result at the time for the maximum force, right column shows the result at the end of the impact, where the impactor is no longer in contact with the head.

6.7.3 Frontal Impact by Flat Surface

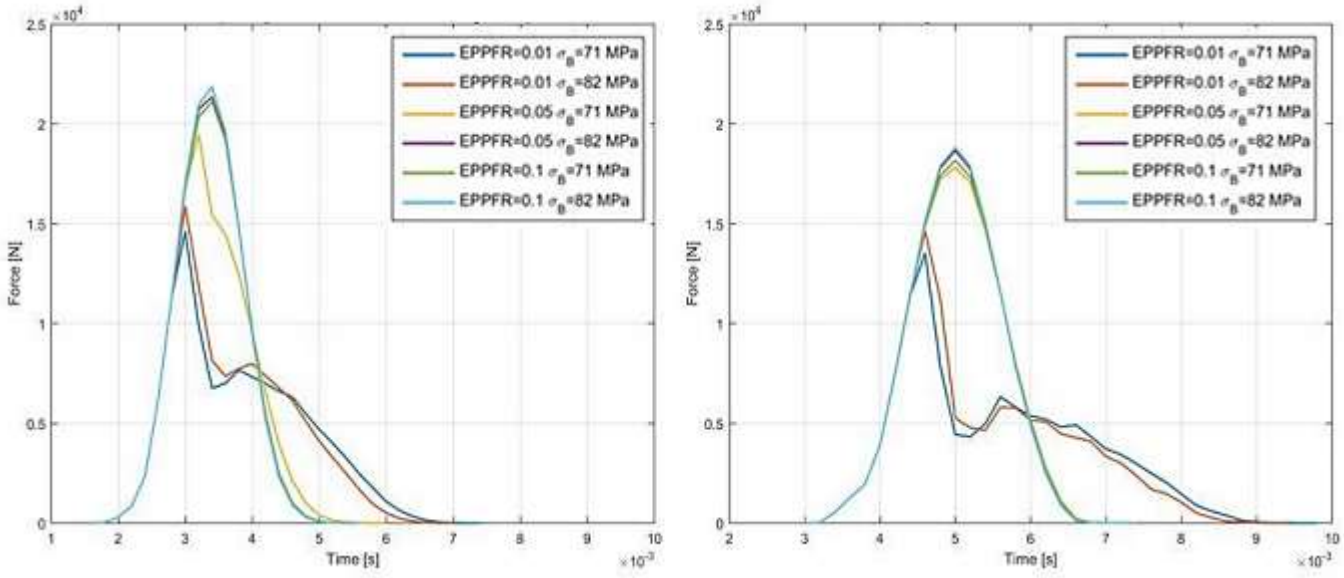

Figure 59: Force-time plots from simulations of frontal impact by flat surface at impact velocity 3.8 m/s.

The left image shows the result from simulations with the original diploë and the right image shows the result from simulations with the scaled diploë. Input variables EPPFR=0.01,0.05 and 0.1 were used for both σB=71 MPa and 82 MPa. No experimental force-time history was available to compare with.

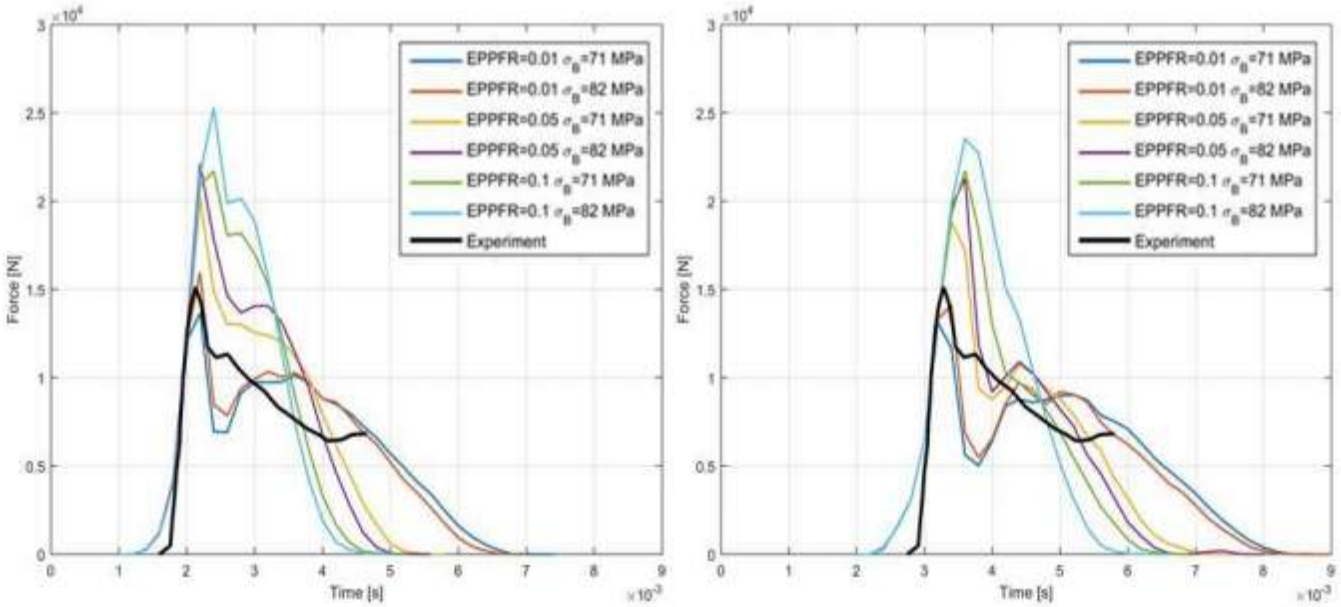

Figure 60: Force-time plots from simulations of frontal impact by flat surface at impact velocity 5.3 m/s.

The left image shows the result from simulations with the original diploë and the right image shows the result from simulations with the scaled diploë. Input variables EPPFR=0.01, 0.05 and 0.1 were used for both σB=71 MPa and 82 MPa. The black curve in both images is data extracted from the literature from the study by Verschueren et al (E. S. Gurdjan, 1947).

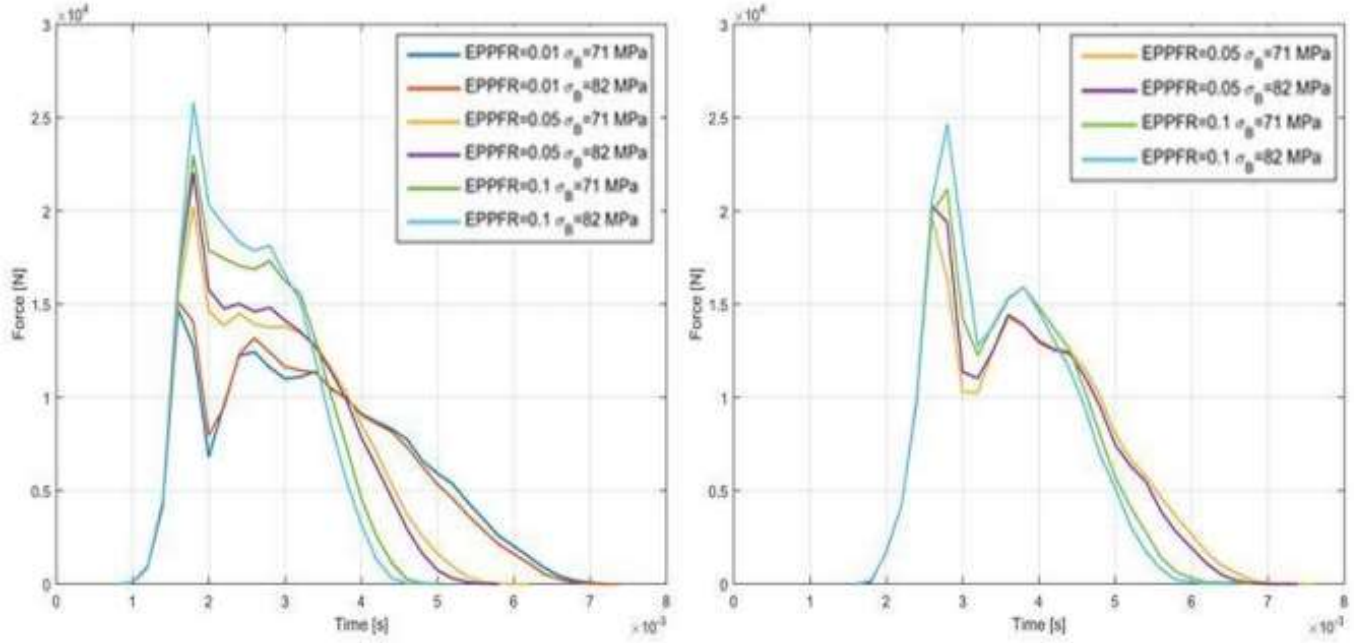

Figure 61: Force-time plots from simulations of frontal impact by flat surface at impact velocity 6.9 m/s.

The left image shows the result from simulations with the original diploë and the right image shows the result from simulations with the scaled diploë. Input variables EPPFR=0.01,0.05 and 0.1 were used for both σB=71 MPa and 82 MPa, except from the scaled model where EPPFR=0.01 and both σB resulted in negative volume elements, hence these results were eliminated.

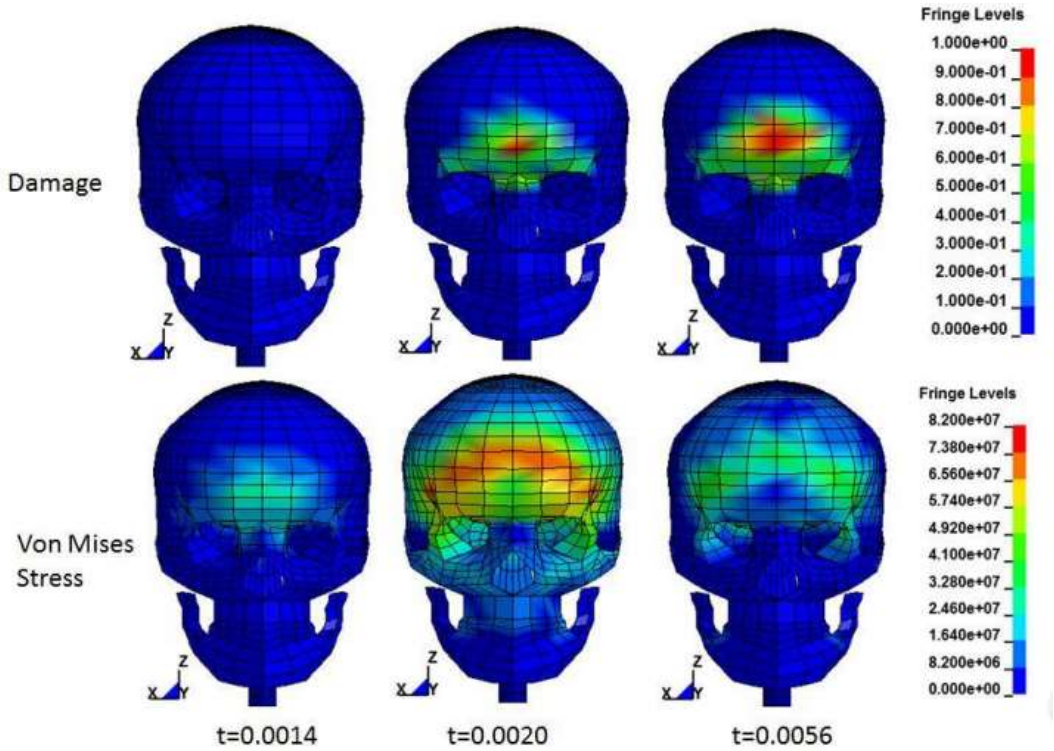

Figure 62: Plotted damage propagation and von Mises stress from simulation of the frontal impact by flat surface, with material 81 and input parameter EPPFR=0.05 and σB=82 MPa

The left column shows the result at the time of the initial impact, middle column shows the result at the time for the maximum force, right column shows the result at the end of the impact, where the impactor is no longer in contact with the head.

6.7.4 Validation against Study of Vertex and Frontal Impact by Sphere

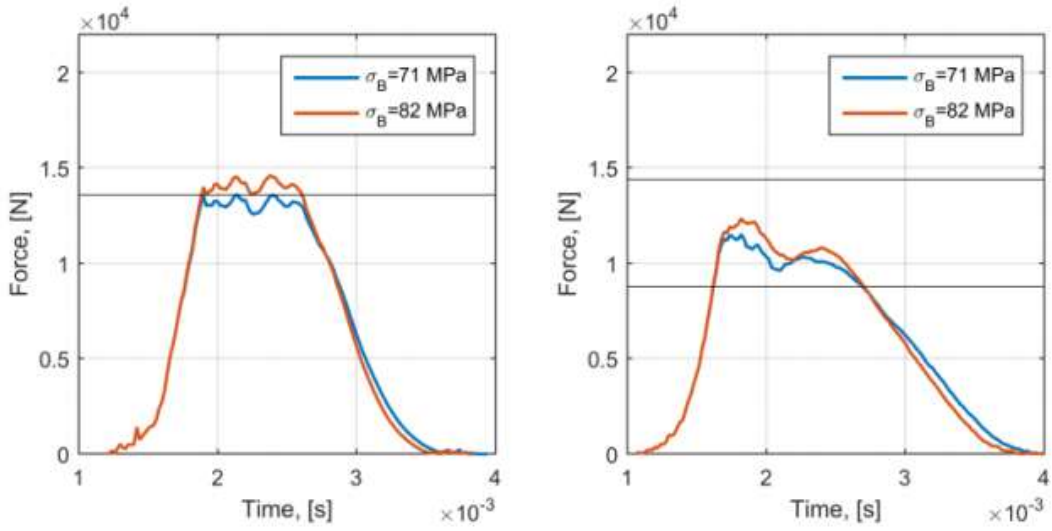

Figure 63: Force-time plots with input parameter EPPFR=0.05.

Frontal impact is presented in the image to the left while the vertex impact is presented in the image to the right. The horizontal lines represent the maximum force obtained in the experiments. The two lines in the right image shows the highest and lowest experimental value.

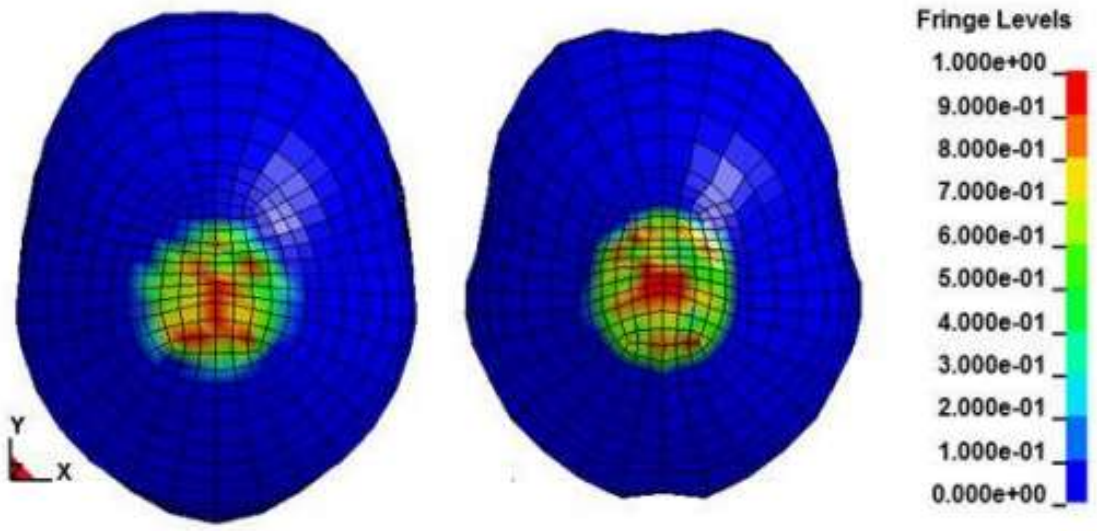

Figure 64: Plotted damage parameter over vertex region from simulation of vertex impact by sphere

The left image shows the outer table while the right image represents the inner table.

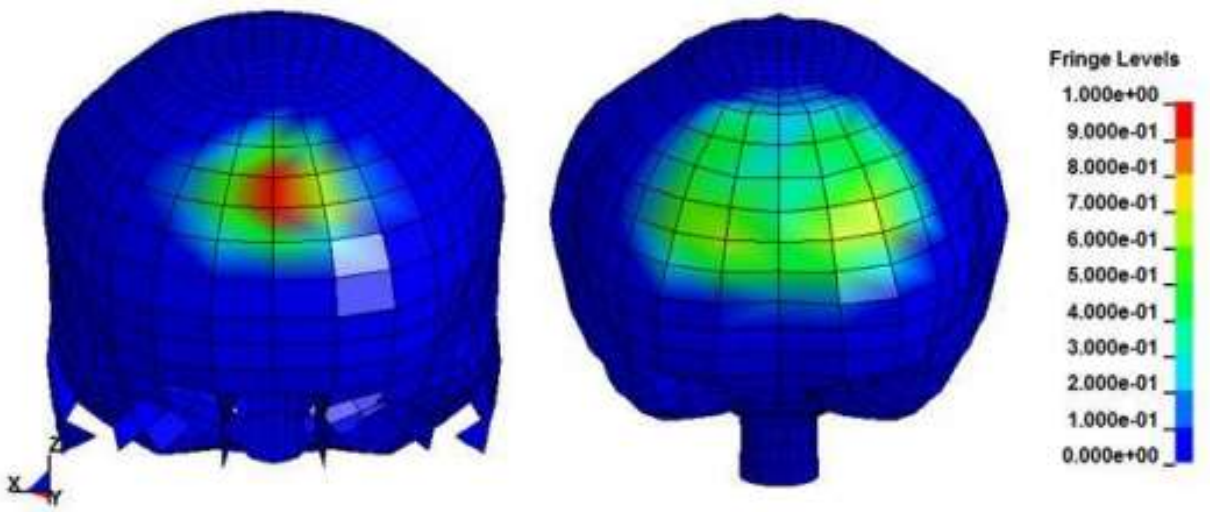

Figure 65: Plotted damage parameter over the frontal bone, from simulation of frontal impact by sphere.

The left image shows the outer table while the right image represents the inner table.

6.8 Conclusion:

- Two material models were found in the LS-DYNA material library, which seemed to meet these request. They were material 81 (MAT_PLASTICITY_WITH_DAMAGE) and material 105 (MAT_DAMAGE_2).
- Material model 81 with input parameter EPPFR=0.05 gave the most stable simulations and accurate results, both for fracture forces and fracture prediction.
- The fracture prediction is limited, in terms of fracture propagation and type of fractures, due to the coarse mesh of the model.
- The breaking stress does not significantly affect the fracture modelling, but have an impact on the peak forces obtained in all simulations.
- The thickness of the diploë does not significantly affect the fracture modelling, but have an impact on the peak forces obtained in the simulations of the frontal impacts.

7. Effect of load rate on the fracture tolerance of the tibia: (Pape focus: FE analysis of tibia and comparison with experimental results)

Fractures of the lower leg are common during frontal automotive collisions and military blasts. These two scenarios cause injury via a similar axial loading mechanism. The majority of previous studies that have conducted axial impact tests to determine the injury limits of the lower leg have simulated automotive impacts; however, due to the viscoelastic nature of bone, it remains unclear whether limits from automotive experiments can be applied to higher-rate blasts. The purpose of this work was to study the effect of load rate on the fracture tolerance of the tibia during these two scenarios.

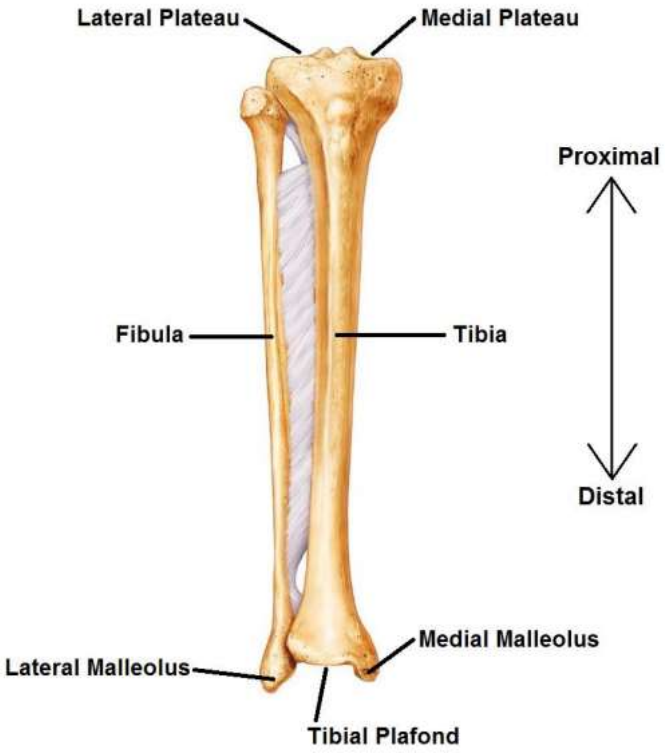

Figure 66: Lower Leg Anatomy

Frontal view of the bones of the right-sided lower leg, with key anatomical landmarks highlighted. Adapted from Martini et al. (2009).

7.1 Injury tolerance for lower leg axial impact:

The loading scenario replicated through testing, significant factors that contribute to injury prediction, force that corresponds to a 10% probability of injury, and locations of injury are summarized for previous cadaveric lower leg axial impact studies.

Study	Loading Scenario	Significant Injury Risk Factors	10% Injury Risk Force	Injury Locations
Yoganandan *et al.* (1996, 1997)	Automotive	Axial force, age	5.4 kN	Foot/ankle complex
Griffin *et al.* (2001)	Military	Load rate, impulse, axial force, body weight	2.1 kN	Calcaneus, cuboid, navicular, talus, and distal tibia
Seipel *et al.* (2001)	Automotive	Axial force	2.5 kN	Calcaneus
Funk *et al.* (2002)	Automotive	Axial force, gender, age, body weight, Achilles tension	5.8 kN	Foot/ankle complex
McKay and Bir (2009)	Military	Axial force, impactor velocity	2.4 kN	Calcaneus, cuboid, fibula, tibia, talus
Quenneville *et al.* (2011)	Military	Projectile mass, velocity, momentum, kinetic energy, impact duration, impulse, axial force, age, height, body mass	7.9 kN	Distal tibia
Yoganandan *et al.* (2014)	Automotive	Axial force, age	6.8 kN	Foot/ankle complex
Bailey *et al.* (2015)	Both	Axial force, dorsiflexion angle	6.2 kN	-

Figure 67: Injury tolerance for lower leg axial impact at different circumstances

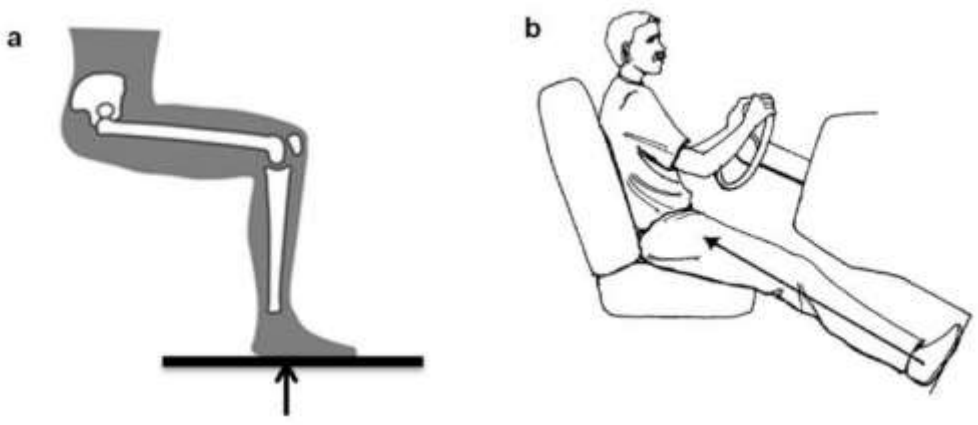

Figure 68: Impact loading of the lower leg due to a) military underbody blast (Quenneville 2016); b) contact with the floor pan during a frontal automotive collision (Whiting and Zernicke 1998).

7.2 Modelling the Tibia:

The tibia model used in this work was previously developed by Quenneville and Dunning (2011). All bone components were modelled using the ELFORM 1 constant stress element formulation.

The material properties in the present study were kept the same as were used in Quenneville and Dunning (2011). The cortical bone was modelled as an elastic-plastic material (LS-Dyna® material model MAT 24), which is defined using material and strain rate dependency properties. The properties of cortical bone were taken from the literature. These included a density of 1,850 kg/m3 , an elastic modulus of 17 GPa, a Poisson's ratio of 0.3, a yield stress of 0.125 GPa, and a tangent modulus of 1 GPa. The strain rate dependency of bone was modelled using a family of curves method obtained from Untaroiu et al. (2004). This method uses stress versus strain curves defined at several different strain rates to determine the material's strain rate dependency.

Similarly, the cancellous bone was also modelled using an elastic-plastic material model, with material properties obtained from the literature: density of 1,000 kg/m3 , elastic modulus of 0.4 GPa, Poisson's ratio of 0.3, yield stress of 10 MPa, and tangent modulus of 0.025 GPa. Since a family of curves could not be found in the literature for cancellous bone, a Cowper-Symonds method was used to accounts for strain rate effects. This model scales the yield stress by the factor: where $\dot{\varepsilon}$ is the strain rate, C = 360.7 and P = 4.605 (Iwamoto et al. 2005).

$$1 + \left(\frac{\dot{\varepsilon}}{C}\right)^{1/p}$$

The marrow was simply modelled as an elastic material (LS-Dyna® material model MAT 1) with a density of 1000 kg/m3, a modulus of 200 MPa, and a Poisson's ratio of 0.35.

A 36.7 kg impactor was used to impact the leg at 7.2, 9.9, and 11.6 m/s velocities.

7.3 Contact and boundary conditions:

Accurate modelling of contact interfaces is essential to the predictive capability of a finite element model. Contact parameters among all the model parts needed to be defined so the model recognizes how they should interact with each other. In LSDYNA®, contact defines (via parts, part sets, segment sets, and/or node sets) which locations should be checked for potential penetrations of another part. The program checks for penetrations by the slave nodes into the master segments at every time step, and if penetration is detected, a restoring correction is applied to resist and eliminate the penetration. Determining which location to assign as the slave segment and which to assign as the master segment depends on a variety of factors, including the coarseness of the mesh and how deformable each part is.

The contact card *CONTACT_TIED_NODES_TO_SURFACE_OFFSET was used to define the contacts between the top plate and the back plate, and the back plate and the bone pot. All of these components were rigid, which means that constraint-based contacts could not be used with these materials (LSTC 2015). The OFFSET option turns a constraint-based contact into penalty-based, which can be used with rigid parts. In the case of the contact between the top plate

and the back plate, a slave node set was created at the back plate that was tied to a master segment set on the top plate. In the case of the contact between the back plate with the pot, a slave node set was created at the bone pot that was tied to a master segment set on the back plate.

The contact card *CONTACT_TIED_SURFACE_TO_SURFACE_OFFSET was used to define contact between deformable components of the apparatus using segment sets (the proximal end of the tibia with the bone pot, the base of the talus with the impact bracket, and the impact bracket with the deformable sponge). This contact type allowed for the surface of the talus and surface of the deformable sponge to be tied to the elastic impact bracket as it translated forward.

Contact between the surface of the talus and the distal articular surface of the bone was defined using the *CONTACT_AUTOMATIC_SURFACE_TO_SURFACE card. Segment sets were defined at the interfacing surfaces and this two-way treatment of contact checks for penetrations by both surfaces in the contact. Due to the presence of cartilage on the articular surface of the tibia, a very low frictional coefficient was assigned to this contact (0.01) for both static and kinetic friction (Hamill and Knutzen 2003). To ensure accurate placement of the talus against the distal articular surface of the tibia, the talus was positioned against the distal surface of the tibia using automatic contact detection. The talus and tibia were both aligned in the anteroposterior and mediolateral axes when they were imported into LS-PrePost®. The talus was then moved axially towards the tibia until it was just making contact with the articular surface, without any initial penetrations.

Contact between the impact bracket and bearing rail was also defined using the CONTACT_AUTOMATIC_SURFACE_TO_SURFACE card, again with segment sets defined at the interfacing surfaces. To model the frictional forces of the impact bracket as it moved along the bearing rail, an iterative process was used to determine the frictional coefficients to assign to this contact. This involved independently varying the values of the static and kinetic frictional coefficients from values between 0 and 0.1 by increments of 0.05. The frictional coefficients were adjusted in an attempt to match the peak axial force from the non-fracture experimental tests. The values that reduced the peak force error between the two non-fracture test were then used for all simulation trials.

The contact between the projectile and the deformable sponge was also defined using automatic surface to surface contact, except the entire parts were used to define the contact instead of segment sets, due to the large deformation the sponge experienced during impacts. For this same reason, interior contact was defined for the sponge to prevent its nodes from penetrating its own faces.

The top rail and bearing rail were constrained in all directions to remain stationary during impact. The bone specimen, bone pot, back plate, and top plate were left unconstrained and free to move in any direction, similar to the movement of the specimen during experimental testing. The talus, impact bracket, deformable sponge, and projectile were constrained to move only in the y-direction (the direction of impact), to produce purely axial movement.

To accurately model the swinging movement of the specimen after impact, gravity was included in the model to act in the negative z-direction. Impacts were modelled using an initial velocity in the positive y-direction for the projectile, in accordance with the experimental testing conditions.

7.4 Comparison to experimental results:

Of the six donors that were tested experimentally, one was selected to use for validation of the finite element model. Selection was based on an evaluation of the age and fracture force for both test conditions. In order to choose the most representative data, each donor was ranked on its proximity to the average value for each factor, and the donor with the 'most average' overall rank was selected, which was donor 1567 (Table 70). The force curves from both tibias from this donor were compared to those of the model, in order to assess the model's ability to predict fracture forces from impacts.

Donor	Age (years)	Age Rank	Low-Rate Force (N)	F_A Rank	High-Rate Force (N)	F_M Rank	Sum	Overall Rank
1494	50	6	10,672	3	13,275	3	12	5
1536	55	4	10,826	2	14,258	4	10	3
1538	66	2	9,063	6	13,500	1	9	2
1541	68	3	12,802	5	11,812	6	14	6
1567	61	1	11,257	4	13,311	2	7	1
1600	74	5	11,002	1	14,542	5	11	4
Average	62.3		10,937		13,450			

Figure 69: Selection of Most Representative Donor

Donors were ranked according to their age and fracture forces in both the lower-rate and higher-rate test conditions being closest to the average of all specimens tested. Donor 1567 was deemed the most representative of the sample population.

Test	Projectile Mass (kg)	Projectile Velocity (m/s)
Lower-Rate Non-Fracture	21.0	6.2
Lower-Rate Fracture	34.6	6.2
Higher-Rate Non-Fracture	6.3	11.3
Higher-Rate Fracture	6.9	11.3

Figure 70: Model Testing Conditions

The model was validated using four testing conditions. Both a fracture test and a nonfracture test were simulated under both experimental conditions to investigate the model's ability to predict tibia response at varying dynamic loading rates. The corresponding projectile mass and projectile velocity for the experimental tests were inputs for the model.

The model's ability to distinguish between a fracture test and a non-fracture test was evaluated using critical maximum principal strain and Von Mises stress values from literature. Areas with maximum principal strain values exceeding critical strain values of 0.016 for cortical bone (Untaroiu et al. 2005) and 0.134 for cancellous bone (Takahashi et al. 2000) were deemed as fracture points, while critical Von Mises stress values of 5.3 MPa for cancellous bone and 134 MPa for the cortical region were used (Untaroiu et al. 2005). Fringe plots were used to visualize regions that exceeded these critical values during all testing conditions.

Solid elements that are modelled with a constant stress formulation (ELFORM 1) can undergo hourglassing. Hourglassing is an artificial deformation mode that produces zero strain and no stress (LSTC, 2015). This occurs in elements with a constant stress formulation due to the fact that they have a single integration point through each

element, and the integration will misleadingly not record a stress if it remains unchanged at this location during a simulation (as would happen in a trapezoid-shaped deformation). To ensure that artificial deformation modes were not present in the model, the simulation's hourglass energy was evaluated. This was done by measuring the model's hourglass energy to determine if it remained below a threshold value of the simulation's total internal energy. An acceptable range of 10% or less of the total internal energy was used since this has been used in previous studies (Quenneville and Dunning, 2011).

7.5 Results:

Modelling the impact bracket as an elastic component with the material properties of steel caused the impact bracket to experience bending during impact and exert a force against the bearing rail (Figure 73). Using peak force values from the non-fracture experimental testing, values of 0.1 for the static friction coefficient and 0.05 for the kinetic friction coefficient were chosen to model the frictional forces that occurred between the impact bracket and the bearing rail. Generally, a greater value for the coefficient of static friction decreased the peak force produced by the model, while a greater value for the coefficient of kinetic friction decreased the time to peak force.

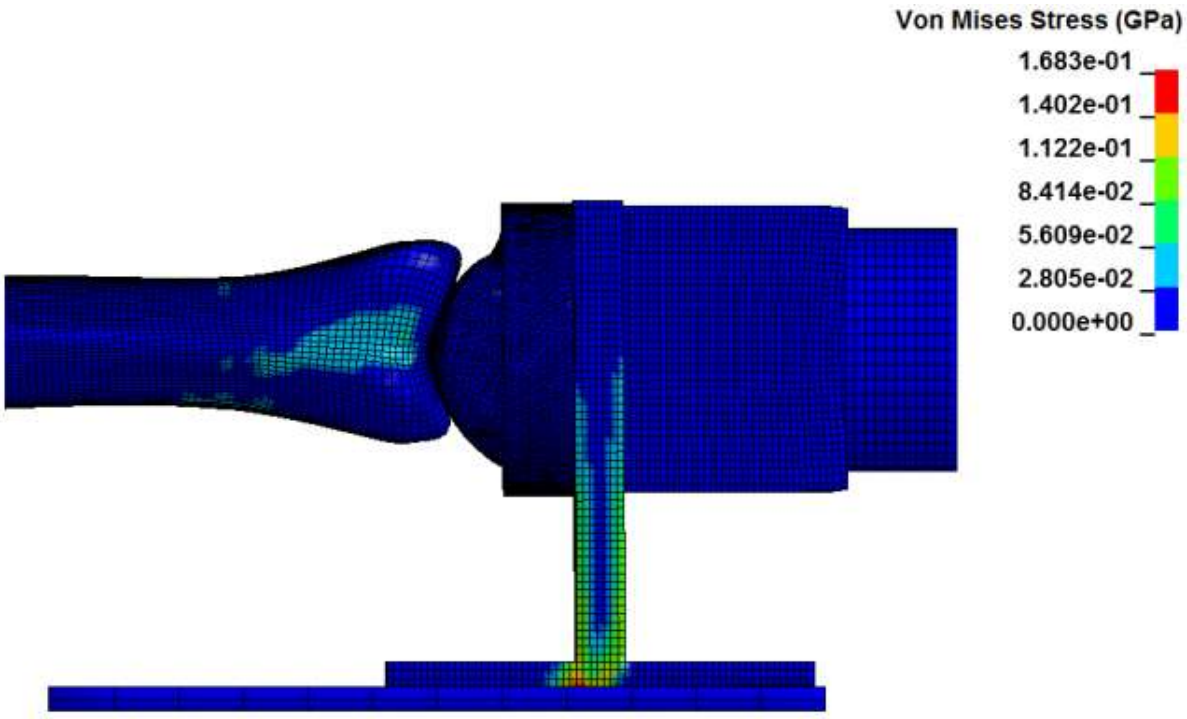

Figure 71: Impact Bracket Loading

The impact of the projectile striking the deformable sponge that was attached to the impact bracket caused a frictional force at the interface between the impact bracket and the bearing rail. The coefficients of friction between the impact bracket and the bearing rail were optimized to minimize errors in peak axial forces from non-fracture experiments. A static coefficient of friction of 0.1 and a kinetic coefficient of friction of 0.05 resulted in peak forces within 20% of those seen experimentally.

Peak axial force during the lower-rate test condition was 7.9 kN (90% of experimental value) for the non-fracture condition (Figure 73) and 8.3 kN (73% of experimental value) for the fracture test (Figure 74). The peak force values

for the higher-rate condition were 12.4 kN (118% of experimental value) for the non-fracture test (Figure 75) and 12.8 kN (96% of experimental value) for the fracture test (Figure 76)

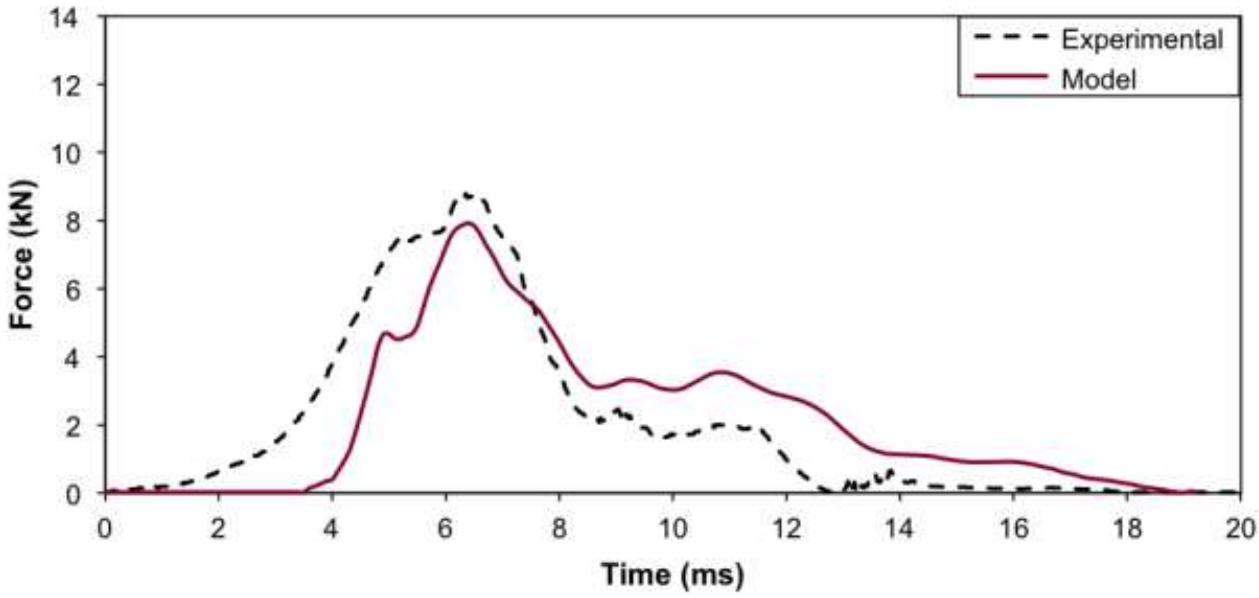

Figure 72: Force Curves for Lower-Rate Non-Fracture Tests

The peak force of the model was 90% of the experimental force, whereas impact duration was 127% as much. The model curve was represented in red, while the dashed black line represented the experimental curve.

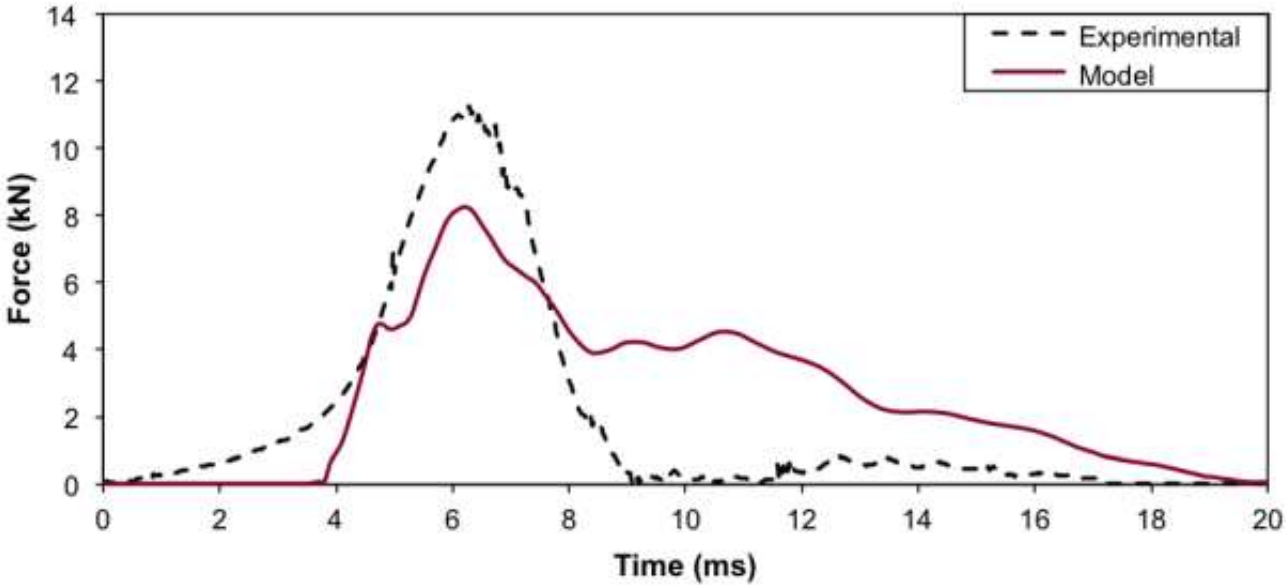

Figure 73: Force Curves for Lower-Rate Fracture Tests

For the lower-rate fracture test, the simulation achieved 73% of the experimental axial force, while duration was 133% as much.

A comparison of the peak force, impact duration, and impulse values between the simulation and experimental results is shown in Table 77. The model values were presented as a fraction of the experimental values for these factors in order to compare the two (Table 78). Impact duration values were larger in the FE simulation than the experimental

values for all four test conditions. For the automotive tests, the duration was 15.2 ms (127% of experimental) in the non-fracture test, while duration was 16.1 ms (133% of experimental) in the fracture test. In the higher-rate condition, non-fracture duration was 8.4 ms (118% of experimental) while the fracture duration was 8.5 ms (185% of experimental). Impulse values were also larger in the simulation than in experiments.

Established thresholds from the literature for Von Mises stress and maximum principal strain were used as criteria to determine fracture in the model. Fringe plots were created for all four test conditions that showed regions of the distal surface of the tibia that exceeded the corresponding critical values, highlighted in red. For the lower-rate automotive test condition, maximum principal strain values that exceeded the established thresholds were not seen in cancellous bone in either the non-fracture or fracture tests, but miniscule regions were seen in the cortical bone in both the non-injurious and injurious tests (Figure 79). In terms of Von Mises stress, regions of fracture were seen in the cancellous bone, but in both the non-injurious and injurious tests; fracture was not seen in the cortical bone (Figure 80). For the higher-rate military tests, maximum principal strains only predicted fracture in a very small region in the cortical bone in both the nonfracture and fracture tests (Figure 81). Von Mises stress during the military tests also only predicted fracture in the cortical bone and in both injurious and non-injurious tests (Figure 82).

The hourglassing that occurred in the model throughout each simulation was evaluated by comparing to the total internal energy of the model. Hourglass energy was between 2.0% and 3.0% of the total internal energy for all tests, and as such was deemed to be acceptable.

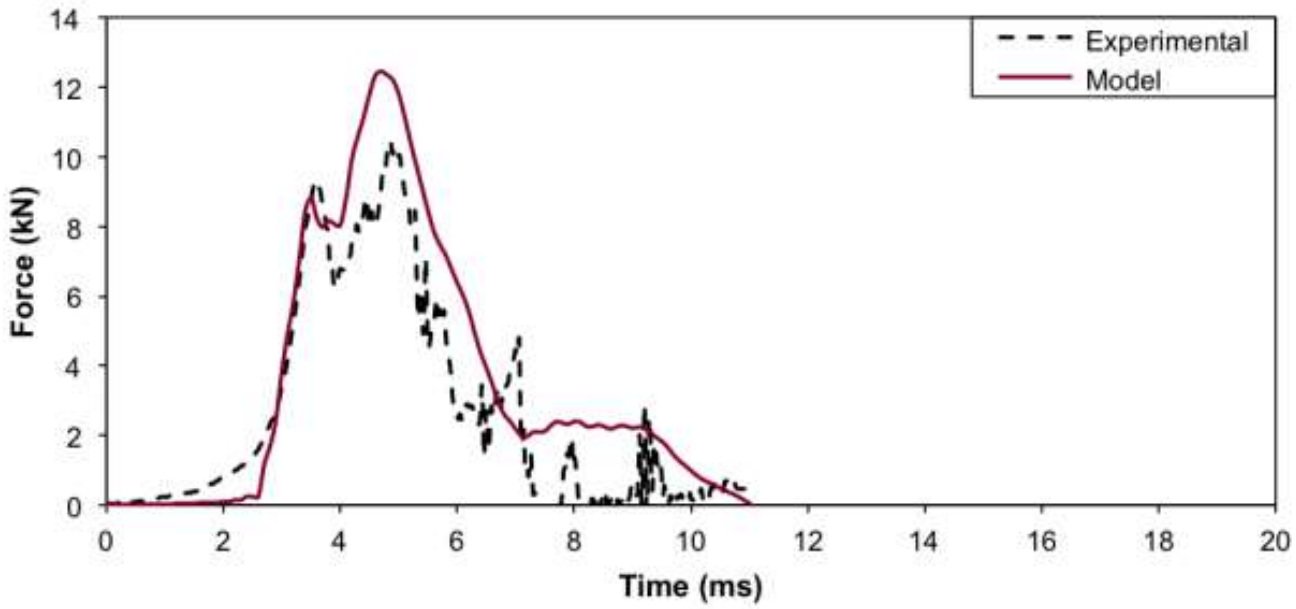

Figure 74: Force Curves for the Higher-Rate Non-Fracture Tests

Peak force of the simulation was 118% of the force from the experimental test, while duration was also 118% of the experimental value in the higher-rate non-fracture tests.

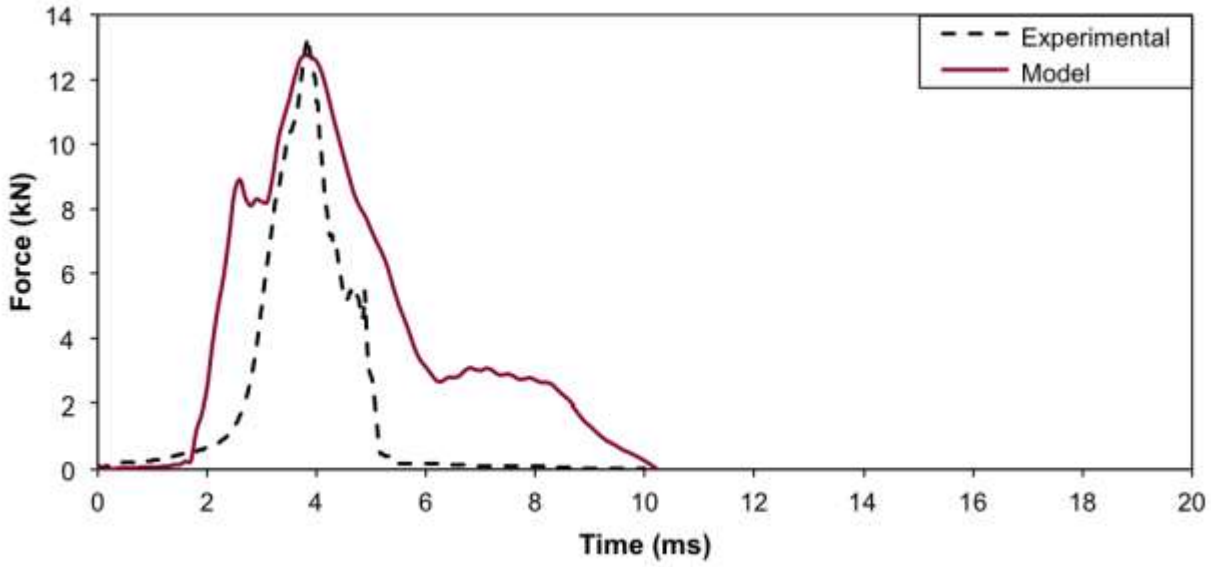

Figure 75: Force Curves for Higher-Rate Fracture Tests

Peak force of the simulation matched was 96% of the experimental value in the higher rate fracture test, while duration was 185% of the experimental value.

7.6 Summary of model validation results:

	Auto Non-Fracture		Low-Rate Fracture		High-Rate Non-Fracture		Military Fracture	
	Model	Experiment	Model	Experiment	Model	Experiment	Model	Experiment
Peak Force (kN)	7.9	8.8	8.3	11.3	12.4	10.5	12.8	13.3
Duration (ms)	15.2	12.0	16.1	12.1	8.4	7.1	8.5	4.6
Impulse (Ns)	41.0	39.2	51.3	37.5	38.7	27.3	41.9	18.2

Figure 76: Summary of Model Validation Results

The values for peak axial force, impact duration, and impulse values for the four test conditions in the experimental and computational testing.

	Low-Rate Non-Fracture			Low-Rate Fracture			High-Rate Non-Fracture			High-Rate Fracture		
	F	D	I	F	D	I	F	D	I	F	D	I
Model/Experimental	0.90	1.27	1.05	0.73	1.33	1.37	1.18	1.18	1.42	0.96	1.85	2.30

Figure 77: Summary of Model Validation Results

These values were compared between the four simulation tests and the corresponding experimental tests by providing the ration between model values and experimental values.

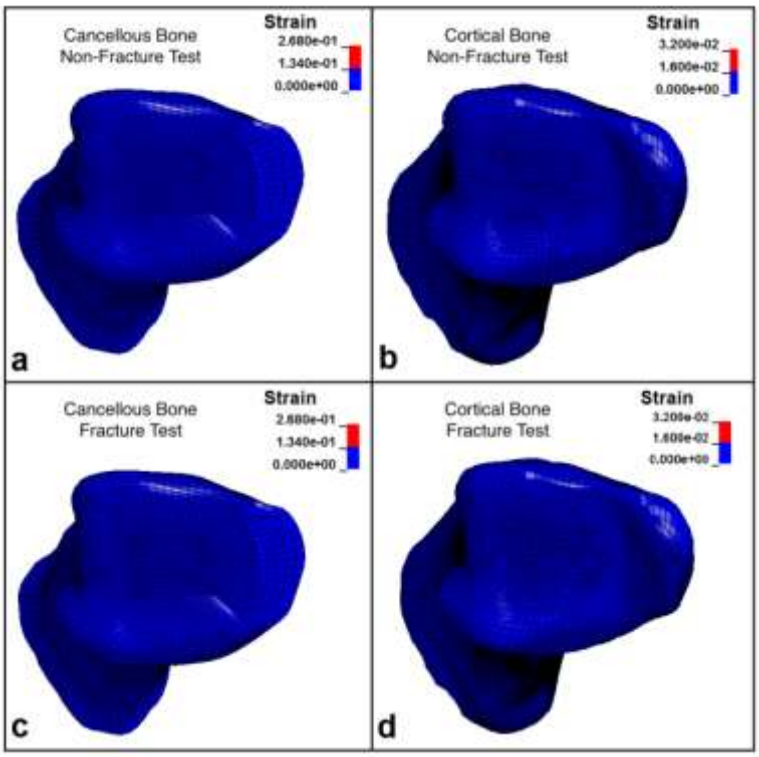

Figure 78: Maximum Principal Strain in the Lower-Rate Tests

The threshold for fracture was 0.134 for cancellous bone and 0.016 for cortical bone (elements exceeding these thresholds are shown in red).

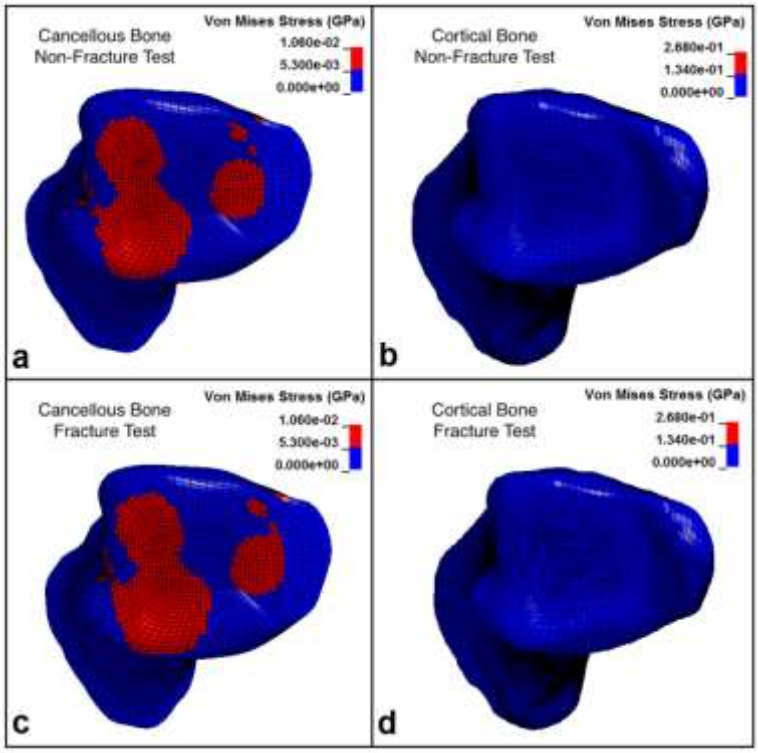

Figure 79: Von Mises Stress in the Lower-Rate Tests

The threshold for fracture was 5.3 MPa for cancellous bone and 134 MPa for cortical bone, with elements exceeding these values shown in red.

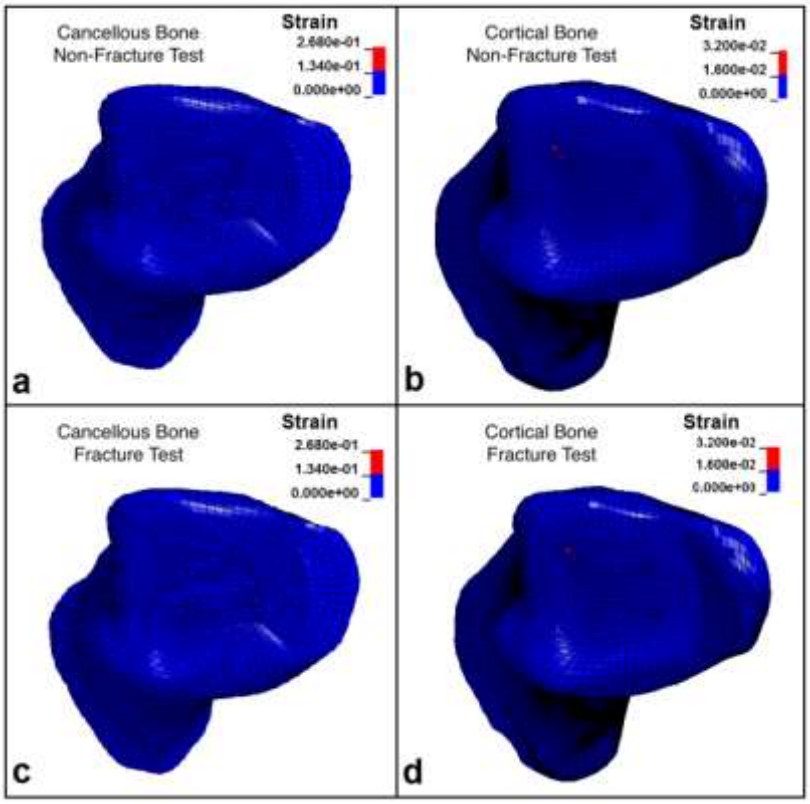

Figure 80: Maximum Principal Strain in the Higher-Rate Tests

The threshold for fracture was 0.134 for cancellous bone and 0.16 for cortical bone, with elements exceeding these values shown in red.

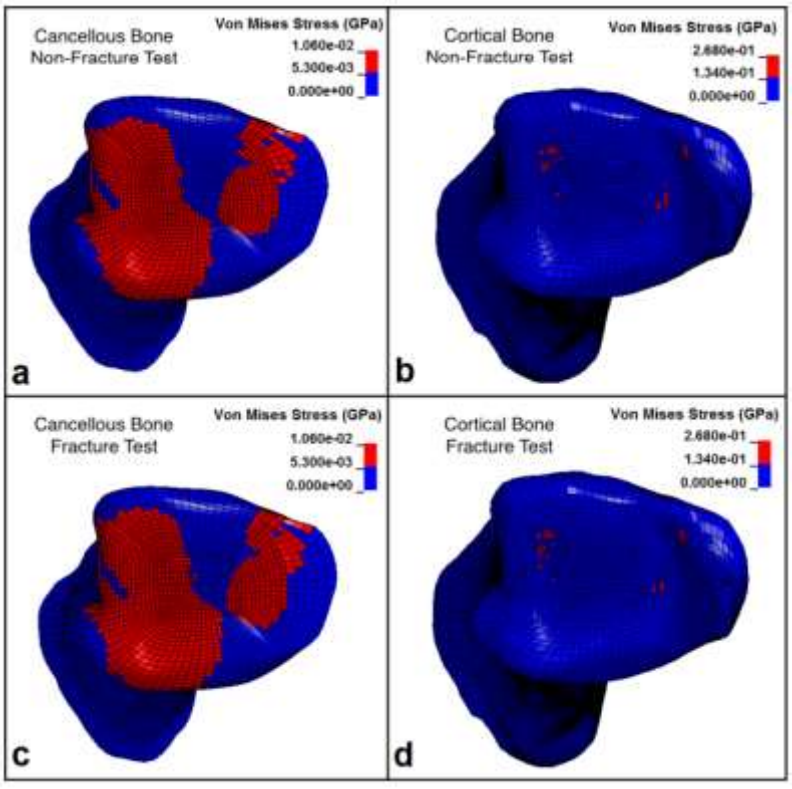

Figure 81: Von Mises Stress in the Higher-Rate Tests

The threshold for fracture was 5.3 MPa for cancellous bone and 134 MPa for cortical bone, with elements exceeding these values shown in red.

The model's peak force values were within 20% of experimental values for the non-fracture cases, and within 27% for the fracture cases. Results from future studies using this model can therefore be used as a general indicator of the force produced at the tibia during an axial impact, and the boundary conditions of the model can be easily altered to test a variety of impact conditions.

7.7 Results discussion:

Accurate representation of the physical contacts in the model is also crucial to its results. The contact friction that occurred at the interface between the impact bracket and the bearing rail was modelled through an iterative process using peak force values from the non-fracture tests for both the lower rate and higher-rate test conditions. The peak force values from the fracture tests were not used since a FE model does not simulate the energy lost due to cracking during a fracture. The values used for frictional coefficients resulted in a static coefficient of friction that is greater than the kinetic coefficient of friction. Coefficient of friction values are often less for kinetic friction (Gross et al. 2013), so it is likely that this would also be the case during the experimental testing.

The peak force values achieved by the computational model were more aligned with cadaveric results in the non-injurious simulations (within 20% of experimental forces) than the injurious simulations (96% of fracture force was achieved in the higher rate fracture test but only 73% was achieved in the lower-rate fracture test). It was expected that the results would be less consistent when evaluating injurious tests since the model does not simulate failure occurring in the tibia and its associated loss of energy due to fracture. However, these peak force relationships correspond to the model being compared to a single donor that was selected as being most representative of the six donors tested. When the peak force values were compared to the average peak force values across all donors from cadaveric testing, the model's results actually fell within the range of these values. Previous finite element studies corroborate their models by developing acceptable corridors for validation parameters such as peak force based on cadaveric testing, analogous in this work to the average peak fore across all donors. While the model had some degree of error when verifying its results to a specific donor, its results actually represented the average population tested experimentally in Chapter 3 quite well. Since the model was meant to represent the response of an average population, its ability to predict peak force during impact loading was considered to be successful. The previous study that developed the model of the isolated tibia (Quenneville and Dunning 2011a) showed that peak force was within 10% of the experimental values for all tests except the fracture test. However, the higher level of agreement in that study was expected since the computational results were evaluated against the results of the corresponding specimen in cadaveric testing.

The impact durations seen in the results of the simulation were larger than those seen experimentally. It is interesting to note that impact durations were better aligned in the non-fracture tests (27% for the lower-rate condition and 18% for the higher-rate condition) than for the fracture tests (33% for the lower-rate condition and 85% for the higher-rate condition). Impact durations were fairly inconsistent during injurious cadaveric tests since the deformation of the bone would lead to a sudden lack of contact against the talus. Since the model does not simulate bone fractures, these inconsistencies with injurious tests were expected. Impulse values were greater in the simulation than those seen

experimentally for all four test conditions (between 5% and 130% greater). This was likely caused by the longer impact durations that the model showed.

The inaccuracies in terms of impact duration and peak force may be attributed to the modelling of the deformable sponge. The material properties of the sponge were determined through compressive testing using a material testing machine. Due to the limitations of this apparatus, the compression tests were conducted at a rate of 50 mm/min. This is magnitudes smaller than the loading rate of the deformable sponge during impact testing. It is likely that the stiffness of the sponge would vary depending on loading rate, and in reality, the sponge may be much stiffer when subjected to the load rates observed in cadaveric testing, as deformable sponges and foams typically have material properties that are strain-rate dependent (Saha et al. 2005). Since the deformable sponge was used to control the impact duration, and therefore the loading rate, accurate modelling of its material properties may have a great effect on the overall results of the FE model. While a rigorous investigation of the material properties of the deformable sponge was not within the scope of this work, better characterization may lead to a more accurate model, and could be a beneficial topic of future investigation.

The simulation's ability to predict fracture based on critical values for maximum principal strain and Von Mises stress was limited. Several tests resulted in failure being predicted in the non-fracture tests (Von Mises stress for both the lower-rate and higherrate non-fracture tests in cancellous bone and Von Mises stress in the cortical bone region for the military non-fracture test). Overall, the fringe plots were indistinguishable between non-injurious and injurious tests. As such, the peak forces established by the model were determined to be as the best predictors of fracture based on injury risk curves produced in the previous cadaveric work. Also, in the previous model of the isolated tibia that used in this study (Quenneville and Dunning 2011a), maximum principal strain values were not capable of predicting areas of fracture, while the values for Von Mises stress were limited in their ability to predict fracture. The results of this model were therefore in agreement with those of the previous paper that developed the model of the isolated tibia.

A limitation of this work is the fact that the model was validated using experimental results from a bone that do not correspond to the tibia used in the simulation, and the material properties of this bone were taken from values from literature. The varied geometry and material properties within a given population can lead to a great range in injury tolerance. However, this previously validated model of the tibia was created with the intention of being representative of an average male, and its material properties correspond to values representative of an average male population. The donor that was selected to validate the model was also deemed the most average in terms of age and fracture forces for the sample of specimens available from cadaveric testing. Since the model was created with the purpose of being representative of an average male tibia and meant as a general tool that can respond within the natural range of this population, the use of the previously validated tibia mesh and its material properties was deemed acceptable. Another limitation of this work is that the frictional coefficients used to model the contact between the impact bracket and the bearing rail were determined through an iterative process in which values were only ranged by increments of 0.05. The frictional coefficients were also only varied up to values of 0.1 for both static and kinetic friction. Smaller

increments and values greater than 0.1 for the fractional coefficients may lead to more accurate results in terms of the model's ability to match the peak forces seen in experimental testing.

There were several other limitations of this work, many of which are common in finite element models of bone. For computational purposes, the material properties of bone were simplified. The cancellous bone, cortical bone, and marrow were modelled as isotropic and homogeneous materials. In reality, these biological tissues are anisotropic and heterogeneous. The effects of strain rate on the material properties of cortical bone were modelled using a family of curves approach established by Untaroiu et al. (2004). This method provided stress-strain curves for cortical bone up to a strain rate of 1 s-1 . Any strain rates above this maximum rate defined used this curve. During dynamic loading, the bone was subjected to strain rates much larger than this (maximum strain rates seen in the FE model were 32.1 s -1 for the lower-rate automotive condition and 40.2 s -1 for the higher-rate military condition) and as such, providing the stress-strain curves beyond this strain rate would improve the cortical bone's response. In addition, the strain rate effects of cancellous bone were modelled using the Cowper-Symonds approach, which scales the yield stress of a material depending on the strain rate. The elastic modulus of the material however, does not get scaled in this approach. For these high-strain simulations, it is likely that the strain rate has a significant effect on the modulus of the material. The computational simulation in this work was subjected to a range of impact velocities greater than the previous work conducted to create the tibia model. For this reason, it is likely that the effects of strain rate on the tibia may be greater in this study. It would be of interest for future work to investigate the ability of the family of curves and CowperSymonds methods of modelling bone's strain rate dependencies under such a large difference of impact severities. This further investigation may improve the model's ability to predict fracture in the tibia under axial loading.

The work conducted in this chapter produced a FE model of the isolated tibia's response to dynamic axial loading at various rates. The computational model was subjected to varied impact severities (mainly in terms of impact velocity) that has not previously been seen in lower leg axial loading simulations. For this reason, the results of this work can be applied to impact scenarios of various loading rates, including both automotive and military loading conditions. While there are several challenges to simulating this type of loading that are apparent in this work, this model's prediction of force is promising. This model will serve as a beneficial general tool in future works to assess the tibia's risk of injury under automotive and military loading scenarios, and to evaluate the effect of protective systems on fracture risk.

7.8 Conclusion:

- All bone components were modelled using the ELFORM 1 constant stress element formulation
- The cortical bone was modelled as an elastic-plastic material (LS-Dyna® material model MAT 24) and the cancellous bone was modelled as a deformable sponge.
- The contact card *CONTACT_TIED_NODES_TO_SURFACE_OFFSET was used to define the contacts between the top plate and the back plate, and the back plate and the bone pot. All of these components were rigid, which means that constraint-based contacts could not be used with these materials

- The contact card *CONTACT_TIED_SURFACE_TO_SURFACE_OFFSET was used to define contact between deformable components of the apparatus using segment sets (the proximal end of the tibia with the bone pot, the base of the talus with the impact bracket, and the impact bracket with the deformable sponge).
- Contact between the surface of the talus and the distal articular surface of the bone was defined using the *CONTACT_AUTOMATIC_SURFACE_TO_SURFACE card
- Contact between the impact bracket and bearing rail was also defined using the CONTACT_AUTOMATIC_SURFACE_TO_SURFACE card, again with segment sets defined at the interfacing surfaces
- After simulation the model's peak force values were within 20% of experimental values for the non-fracture cases, and within 27% for the fracture cases.
- Smaller increments and values greater than 0.1 for the fractional coefficients may lead to more accurate results in terms of the model's ability to match the peak forces seen in experimental testing.
- Since the deformable sponge was used to control the impact duration, accurate modelling of its material properties may have a great effect on the overall results of the FE model.

8. Conclusion:

Design and simulation of the bone is a complex process with various parameters to be considered. Paper 4 used in this report focuses on the mesh quality of the model. Meshing is a vital part of the finite element analysis process as it greatly affects the output results. Paper 4 states that for many biomechanical modelling tetrahedral elements are preferred as the meshing process is automated. However, hexahedral elements derive better results as it gives better regularity, angle distribution and anisotropy whilst showing improved convergence and sensitivity to mesh orientation.

Paper 5 however focused on creating realistic finite element models of the human cortical bone focusing on its material properties. The model was simulated in LSDYNA using the material card MAT_PIECEWISE_LINEAR_PLASTICITY as it can be defined as an elasto-plastic material with an arbitrary stress versus strain curve and arbitrary strain rate dependency. It was also found that their results were more close to experimental results by Kemper when strain parameters C and P were considered to be 0.

The following paper 6 focused on finite element analysis of a human skull to determine from their two material cards material 81, MAT_PLASTICITY_WITH_DAMAGE and material 105 MAT_DAMAGE_2 the apt one to predict skull fractures. It was found that material model 81 with a rupture strain value of 0.05 gave more stable simulation and accurate results for both fracture forces and fracture prediction.

The last paper of the report paper 7 focused on finite element analysis of tibia fractures focusing on frontal automotive collisions and military blasts and was the apt paper to correlate with the research as it focused on dynamic impact. The material card used in this report was again MAT_PIECEWISE_LINEAR_PLASTICITY for the compact bone and the cancellous bone was modelled as deformable sponge. The model's peak force values were within 20% of experimental values for the non-fracture cases, and within 27% for the fracture cases.

9. References:

- Alberts, B. (1994). Molecular biology of the cell. 3rd ed. New York: Garland.
- Bankoff, A. (2012). Biomechanical Characteristics of the Bone. Human Musculoskeletal Biomechanics. [online] Available at: https://www.intechopen.com/books/human-musculoskeletal-biomechanics/biomechanical-characteristics-of-the-bone [Accessed 19 Jul. 2018].
- Dhanopia, A. and Bhargava, M. (2017). Finite Element Analysis of Human Fractured Femur Bone Implantation with PMMA Thermoplastic Prosthetic Plate. Procedia Engineering, 173, pp.1658-1665.
- Goswami, T. (2011). Human musculoskeletal biomechanics. Rijeka: InTech.
- HOLTROP, M. (2018). The Ultrastructure of Bone. ANNALS OF CLINICAL AND LABORATORY SCIENCE, [online] 5(4). Available at: http://www.annclinlabsci.org/content/5/4/264.full.pdf [Accessed 19 Jul. 2018].
- Lawless, B., Sadeghi, H., Temple, D., Dhaliwal, H., Espino, D. and Hukins, D. (2017). Viscoelasticity of articular cartilage: Analysing the effect of induced stress and the restraint of bone in a dynamic environment. Journal of the Mechanical Behavior of Biomedical Materials, 75, pp.293-301.
- Mackerle, J. (1997). Finite element/boundary element analysis of viscoelastic and viscoplastic problems a bibliography (1994–1996). Finite Elements in Analysis and Design, 27(3), pp.273-287.
- Manda, K., Xie, S., Wallace, R., Levrero-Florencio, F. and Pankaj, P. (2016). Linear viscoelasticity - bone volume fraction relationships of bovine trabecular bone. Biomechanics and Modeling in Mechanobiology, 15(6), pp.1631-1640.
- Manda, K., Xie, S., Wallace, R., Levrero-Florencio, F. and Pankaj, P. (2016). Linear viscoelasticity - bone volume fraction relationships of bovine trabecular bone. Biomechanics and Modeling in Mechanobiology, 15(6), pp.1631-1640.
- Parashar, S. and Sharma, J. (2016). A review on application of finite element modelling in bone biomechanics. Perspectives in Science, 8, pp.696-698.
- Parashar, S. and Sharma, J. (2016). A review on application of finite element modelling in bone biomechanics. Perspectives in Science, 8, pp.696-698.
- Sanborn, B., Gunnarsson, C., Foster, M. and Weerasooriya, T. (2016). Quantitative Visualization of Human Cortical Bone Mechanical Response: Studies on the Anisotropic Compressive Response and Fracture Behavior as a Function of Loading Rate. Experimental Mechanics, 56(1), pp.81-95.
- Wang, J., Parnianpour, M., Shirazi-Adl, A. and Engin, A. (2000). Viscoelastic Finite-Element Analysis of a Lumbar Motion Segment in Combined Compression and Sagittal Flexion. Spine, 25(3), pp.310-318.
- Wu, Z., Ovaert, T. and Niebur, G. (2011). Viscoelastic properties of human cortical bone tissue depend on gender and elastic modulus. Journal of Orthopaedic Research, 30(5), pp.693-699.
- Yamashita, J., Furman, B., Rawls, H., Wang, X. and Agrawal, C. (2001). The use of dynamic mechanical analysis to assess the viscoelastic properties of human cortical bone. Journal of Biomedical Materials Research, 58(1), pp.47-53.
- MARTINEZ, A. (2016). THE EFFECT OF LOAD RATE ON THE AXIAL FRACTURE TOLERANCE OF THE ISOLATED TIBIA DURING AUTOMOTIVE AND MILITARY IMPACTS. [ebook] Hamilton, Ontario: McMaster University. Available at: https://macsphere.mcmaster.ca/bitstream/11375/20966/2/Martinez_Alberto_A_2016Dec_MASc.pdf [Accessed 19 Jul. 2018].
- ANDERSSON, F. (2016). Finite Element Modeling of Skull Fractures. [ebook] Stockholm, Sweden: semanticscholar.org. Available at: https://pdfs.semanticscholar.org/b49f/b7805d164637deeca1bc268fa03fb035b5d2.pdf [Accessed 19 Jul. 2018].

- Basafa, E., Armiger, R., Kutzer, M., Belkoff, S., Mears, S. and Armand, M. (2013). Patient-specific finite element modeling for femoral bone augmentation. Medical Engineering & Physics, 35(6), pp.860-865.
- Bbc.co.uk. (2018). BBC - GCSE Bitesize: Bone growth. [online] Available at: http://www.bbc.co.uk/schools/gcsebitesize/pe/appliedanatomy/2_anatomy_skeleton_rev4.shtml [Accessed 19 Jul. 2018].
- El-Asfoury, M. and El-Hadek, M. (2009). Static and Dynamic Three-Dimensional Finite Element Analysis of Pelvic Bone. World Academy of Science, Engineering and Technology International Journal of Mechanical and Mechatronics Engineering, [online] 3(9). Available at: https://waset.org/publications/14728/static-and-dynamic-three-dimensional-finite-element-analysis-of-pelvic-bone [Accessed 19 Jul. 2018].
- Ftp.lstc.com. (2012). LS-DYNA® KEYWORD USER'S MANUAL. [online] Available at: http://ftp.lstc.com/anonymous/outgoing/jday/manuals/LS-DYNA_manual_Vol_II_R6.1.0.pdf [Accessed 19 Jul. 2018].
- Kumar Reddy, M., Ganesh, B. and Bharathi, K. (2016). Use of Finite Element Analysis to Predict Type of Bone Fractures and Fracture Risks in Femur due to Osteoporosis. Journal of Osteoporosis and Physical Activity, 4(3).
- Lstc.com. (2018). Total Human Model for Safety - THUMS | Livermore Software Technology Corp.. [online] Available at: http://www.lstc.com/thums [Accessed 19 Jul. 2018].
- LSTC.com. (2007). http://lstc.com/pdf/ls-dyna_971_manual_k.pdf. [online] Available at: http://lstc.com/pdf/ls-dyna_971_manual_k.pdf [Accessed 19 Jul. 2018].
- MENDIZABAL DONES, A. (2018). Finite Element Simulation: Tensile test of rib cortical bone. [ebook] Göteborg, Sweden: CHALMERS UNIVERSITY OF TECHNOLOGY. Available at: http://publications.lib.chalmers.se/records/fulltext/128516.pdf [Accessed 19 Jul. 2018].
- Panagiotopoulou, O., Wilshin, S., Rayfield, E., Shefelbine, S. and Hutchinson, J. (2014). What makes an accurate and reliable subject-specific finite element model? A case study of an elephant femur. Journal of The Royal Society Interface, 11(99), pp.20140854-20140854.
- Ramirez, D. and Angeles, H. (2015). Viscoelastic Characterization of Bovine Trabecular Bone Samples. World Academy of Science, Engineering and Technology International Journal of Mechanical and Mechatronics Engineering, [online] 9(5). Available at: http://waset.org/publications/10001717/viscoelastic-characterization-of-bovine-trabecular-bone-samples [Accessed 19 Jul. 2018].
- Thiagarajan, G., Lu, Y., Dallas, M. and Johnson, M. (2014). Experimental and finite element analysis of dynamic loading of the mouse forearm. Journal of Orthopaedic Research, 32(12), pp.1580-1588.
- Umadevi, N. and Geethalakshmi, S. (2011). A brief study on human bone anatomy and bone fractures. IJCES International Journal of Computer Engineering Science, [online] 1(3). Available at: http://www.rxiv.org/pdf/1208.0135v1.pdf [Accessed 19 Jul. 2018].
- Web.mit.edu. (2018). Eight-node brick element (C3D8 and F3D8). [online] Available at: http://web.mit.edu/calculix_v2.7/CalculiX/ccx_2.7/doc/ccx/node26.html [Accessed 19 Jul. 2018].
- Taylor, M., Tanner, K., Freeman, M. and Yettram, A. (1996). Stress and strain distribution within the intact femur: compression or bending?. Medical Engineering & Physics, 18(2), pp.122-131.
- Choi, K. & Goldstein, S.A. (1992), A comparison of the fatigue behavior of human trabeculae and cortical bone tissue. Journal Biomechanics, 25: 1371.
- Shipman, P., Walker, A.; & Bichell, D. (1985), The Human Skeleton. Cambridge, Harvard University Press.
- Beaupied H., Lespessailles E., Benhamou C. (2006), Evaluation of macrostructural bone biomechanics. Joint Bone Spine 74 (2007) pp 233 – 239.

- Kemper A., McNally C., Kennedy E., Manoogian S. et al (2005), Material Properties of Human Rib Cortical Bone from Dynamic Tension Coupon Testing. Stapp Car Crash Journal. November 2005. Vol. 49. pp. 199 – 230.
- Ordaka J., Meijer R., Rooij L. et al (2007), Validation of a Finite Element Human Model for Prediction of Rib Fractures. SAE 2007-01-1161. Detroit, Michigan.
- J. Currey (1984), The Mechanical Adaptations of Bones. Princeton, New Jersey: Princeton University Press
- J. Wood (1971), "Dynamic response of human cranial bone," J. Biomech., vol. 4, no. 3, pp. 1–12.
- European Road Safety Observatory (2012), "Traffic Safety Basic Facts 2015 Pedestrians,".
- S. Kleiven (2002), "Finite Element Modeling of the Human Head," Ph.D dissertation, Department of Aeronautics, Royal Institute of Technology, Stockholm.
- R. P. Hubbard (1971), "Flexure of Layered Cranial Bone," J. Biomech., vol. 4, pp. 251–263.
- J. W. Melvin, D. H. Robbins, and V. Roberts (1969), "The Mechanical Behaviour of the Diploë Layer of the Human Skull in Compression," Dev. Mech., vol. 5, pp. 811–816.
- E. S. Gurdjan, H. R. Lissner, and J. E. Webster (1947), "The Mechanism of Production of Linear Skull Fracture," Surgery, Gynecol. Obstet., vol. 85, pp. 195–210.
- Bonicelli, A., Xhemali, B., Kranioti, E. and Zioupos, P. (2017). Rib biomechanical properties exhibit diagnostic potential for accurate ageing in forensic investigations. PLOS ONE, 12(5), p.e0176785.
- Hay, E. (1982). Cell Biology of Extracellular Matrix. Plenum.
- Huiskes, R. and Chao, E. (1983). A survey of finite element analysis in orthopedic biomechanics: The first decade. Journal of Biomechanics, 16(6), pp.385-409.
- Black J, Korostoff E. (1973), Dyanmic mechanical properties of viable human cortical bone. J Biomech 6:435–438
- Lakes RS, Katz JL, Sternstein SS. (1979), Viscoelastic properties of wet cortical bone—I. Torsional and biaxial studies. J Biomech 12:657–678
- Fondrk M, Bahniuk E, Davy DT, Michaels C. (1988), Some viscoplastic characteristics of bovine and human cortical bone. J Biomech 21:623–630
- Raspanti M, Guizzardi S, De Pasquale V, Martini D, Ruggeri A. (1944), Ultrastructure of heat-deproteinated compact bone. Biomater 15:433–437.
- McElhaney J. (1966), Dynamic Response of Bone and Muscle Tissue. Journal of Applied Physiology, 21, 1231–1236.
- McElhaney, J.; Fogle, J.; Byars, E.; Weaver, G. (1964), Effect of Embalming on the Mechanical Properties of Beef Bone. Journal of Applied Physiology 1964, 19 (6), 1234–1236.
- Lakes R., Katz J.L. (1979), "Viscoelastic properties of wet cortical bone, relaxation mechanisms", J. Biomech.
- Iyo T., Maki Y., Sasaki N., Nakata M. (2003), "Anisotropic viscoelastic properties of cortical bone", J. Biomech., 2003.
- Quaglini V., La Russa V., Corneo S. (2008), "Nonlinear stress relaxation of trabecular bone", Mechanics Research Communications.
- Topolinsky T., Cichansky A., Mazurkiewicz A., Nowicky K. (2011), "Study of the behavior of the trabecular bone under cyclic compression with stepwise increasing amplitude", J. Biomech.
- Ashman R.B. (1989), Experimental techniques, "Bone Mechanics", Cowin, S.C., CRC Press, Boca Raton, FL.

- Griffin, L. V, Harris, R.M., Hayda, R.A., and Rountree, M.S. (2001). Loading rate and torsional moments predict pilon fractures for antipersonnel blast mine loading. International IRCOBI Conference on the Biomechanics of Impacts, Isle of Man (UK), 115–131.
- Funk, J.R., Crandall, J.R., Tourret, L.J., MacMahon, C.B., Bass, C.R., Patrie, J.T., Khaewpong, N., and Eppinger, R.H. (2002). The axial injury tolerance of the human foot/ankle complex and the effect of Achilles tension. Journal of Biomechanical Engineering, 124 (6), 750–757.
- McKay, B.J. and Bir, C.A. (2009). Lower extremity injury criteria for evaluating military vehicle occupant injury in underbelly blast events. Stapp Car Crash Journal, 53 (November), 229–249.
- D. Edgar I., R. and H. José J, et al., A. (2015). Viscoelastic Characterization of Bovine Trabecular Bone Samples. International Journal of Mechanical and Mechatronics Engineering, [online] 9(5). Available at: http://waset.org/publications/10001717/viscoelastic-characterization-of-bovine-trabecular-bone-sample [Accessed 20 Jul. 2018].
- Lakes, R. (2018). Biomechanics: Bone viscoelasticity. [online] Silver.neep.wisc.edu. Available at: http://silver.neep.wisc.edu/~lakes/Biom2.html [Accessed 19 Jul. 2018].
- Lawless, B., Sadeghi, H., Temple, D., Dhaliwal, H., Espino, D. and Hukins, D. (2017). Viscoelasticity of articular cartilage: Analysing the effect of induced stress and the restraint of bone in a dynamic environment. Journal of the Mechanical Behavior of Biomedical Materials, 75, pp.293-301.
- Sanborn, B., Gunnarsson, C., Foster, M. and Weerasooriya, T. (2016). Quantitative Visualization of Human Cortical Bone Mechanical Response: Studies on the Anisotropic Compressive Response and Fracture Behavior as a Function of Loading Rate. Experimental Mechanics, 56(1), pp.81-95.
- Yamashita, J., Furman, B., Rawls, H., Wang, X. and Agrawal, C. (2001). The use of dynamic mechanical analysis to assess the viscoelastic properties of human cortical bone. Journal of Biomedical Materials Research, 58(1), pp.47-53.

10. Appendix:

10.1 Viscoelastic behaviour of bone

Viscoelasticity is the property of a substance of exhibiting both elastic and viscous behaviour, the application of stress causing temporary deformation if the stress is quickly removed but permanent deformation if it is maintained.

Bone exhibits viscoelastic behaviour, i.e. the stress depends not only on the strain but also on the time history of the strain. Such behaviour can manifest itself as creep, which is a gradual increase in strain under constant stress; stress relaxation, which is a gradual decrease in stress in a specimen held at constant strain; load-rate dependence of the stiffness; attenuation of sonic or ultrasonic waves; or energy dissipation in bone loaded dynamically. Experimental rheology modalities based on each of the above phenomena have been used in the study of bone. The results have been converted to a common representation via the interrelationships inherent in the linear theory of viscoelasticity, to permit a direct comparison of results. In the case of tension / compression, there is very significant disagreement among the published results. This disagreement may result from nonlinear viscoelastic behaviour not accounted for in the transformation process, or from experimental artifacts. In the case of shear deformation, however, there is good agreement between results obtained in different kinds of experiments. The loss tangent, which is proportional to the ratio of energy dissipated to energy stored in a cycle of deformation, achieves a minimum value of about 0.01 at frequencies from 1 to 100 Hz. At lower and higher frequencies, the loss tangent, hence the magnitude of viscoelastic effects, is greater, e.g. 0.08 at 1 MHz and at one micro-Hz. To compare, the loss tangent of quartz may be less than one part per million, in metals, from one part in ten thousand to 0.01, in hard plastics from 0.01 to 0.1, and in soft polymers, it may attain values greater than 1. It is notable that the minimum energy dissipation in bone occurs in a frequency range characteristic of load histories during normal activities (Lakes, R. (2018).

10.2 How loading rate (and magnitude?) influences viscoelasticity of bone:

10.2.1 Viscoelasticity of articular cartilage

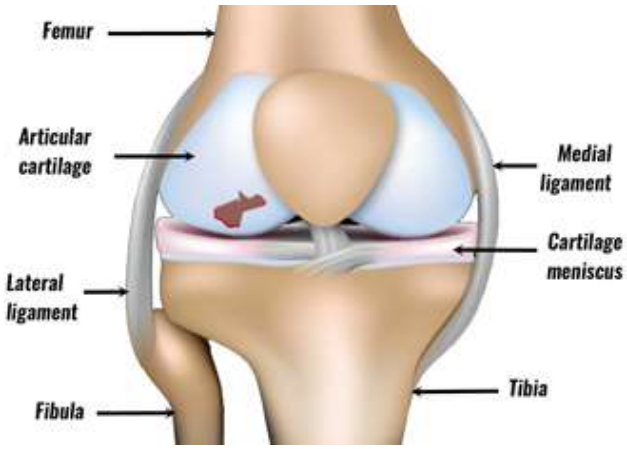

Figure 82: Bovine femoral and humeral head articular cartilage

This information was sourced from the paper: Viscoelasticity of articular cartilage - Analysing the effect of induced stress and the restraint of bone in a dynamic environment. The aim of this study was to determine the effect of the induced stress and restraint provided by the underlying bone on the frequency-dependent storage and loss stiffness (for bone restraint) or modulus (for induced stress) of articular cartilage, which characterise its viscoelasticity (Lawless et al., 2017).

So the factors identified that affect the viscoelasticity is:

- frequency-dependent storage
- loss of stiffness for bone restraint
- Modulus for induced stress of articular cartilage

Dynamic mechanical analysis has been used to determine the frequency-dependent viscoelastic properties of bovine femoral and humeral head articular cartilage. A sinusoidal load was applied to the specimens and out-of-phase displacement response was measured to determine the phase angle, the storage and loss stiffness or modulus. As induced stress increased, the storage modulus significantly increased ($p < 0.05$). The phase angle decreased significantly ($p < 0.05$) as the induced stress increased; reducing from 13.1° to 3.5°. The median storage stiffness ranged from 548 N/mm to 707 N/mm for cartilage tested on-bone and 544 N/mm to 732 N/mm for cartilage tested off-bone. On-bone articular cartilage loss stiffness was frequency independent ($p > 0.05$); however, off-bone, articular cartilage loss stiffness demonstrated a logarithmic frequency-dependency ($p < 0.05$) (Lawless et al., 2017).

In conclusion, the frequency-dependent trends of storage and loss moduli of articular cartilage are dependent on the induced stress, while the restraint provided by the underlying bone removes the frequency-dependency of the loss stiffness.

10.2.2 Viscoelastic properties of the human cortical bone

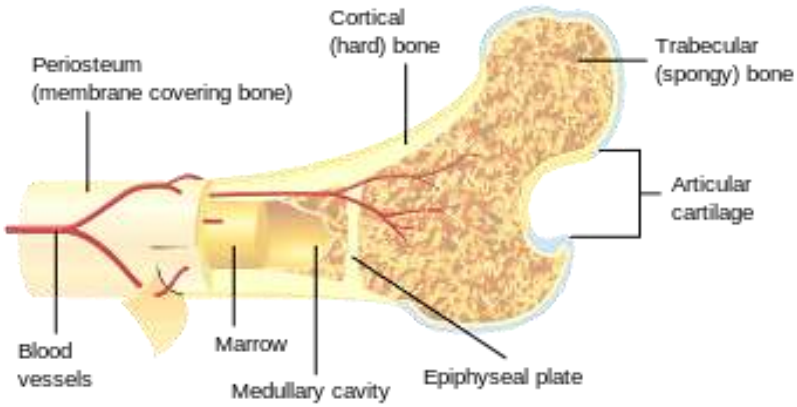

Figure 83: Anatomy of a human cortical bone

This extract is taken from the paper: The use of dynamic mechanical analysis to assess the viscoelastic properties of human cortical bone.

Black et al. measured the dynamic mechanical properties of human bone under tensile conditions using different loading frequencies at 37.5°C and reported that frequency affected the storage modulus. Lakes et al. described the viscoelastic response of bone under torsional loading as a function of temperature. These studies suggest that the viscoelastic behaviour of bone may have a pronounced effect on its fracture behaviour under dynamic loading.
Beyond these studies, there are few published documents available that focus on the viscoelasticity of bone, especially cortical bone. The purpose of the present study was to explore the use of a dynamic mechanical analyser (DMA) as a tool for investigating the viscoelastic properties of bone, and furthermore, to study the effects of various test parameters and establish a reliable technique for using the DMA for bone research (Fondrk et al., 1988). Although the DMA is widely used for characterization of no biologic materials such as plastics and metals, its use for bone has not been described yet. In this study, we mainly performed isothermal tests of human cortical bone at body temperature using the DMA and measured the loss tangent and storage modulus as representative measures of bone viscoelastic properties (Yamashita et al., 2001).

A uniaxial compressive study of human femoral cortical bone was completed over a range of strain rates from quasi-static (0.001/s) to high rates (approximately 1000/s). Loading was applied in the transverse and longitudinal directions of the bone axis. An Instron load frame was used for quasi-static and intermediate rate experiments, while an SHPB setup was used for high-rate investigations. Optical strain measurements with a DIC method were used to measure strain. The mechanical properties of the bone used in this study were found to be anisotropic; the measured properties in the longitudinal direction were higher than the transverse direction. The ultimate strength of the bone material varied from 152.1 ± 21.6 MPa at quasi-static rate to 319 ± 23.9 MPa at high rate in the longitudinal direction and the transverse strength was 86.6 ± 21.7 MPa at quasi-static rate and 178.9 ± 26.02 MPa at dynamic rates.

The compressive stress-strain response found in this study agreed with other studies on human bones. McElhaney (1966) found that an embalmed human femur had an ultimate strength of about 140 MPa at quasi-static rate, while the strength at high rate (1500/s) was about 300 MPa in the longitudinal direction of the bone. In general, direct comparisons between embalmed and fresh bone are unwise because of the significant effects of embalming on bone microstructure and constituents leading to altered ultimate strength, failure strain, and modulus of elasticity of bone 15 material (McElhaney et al, 1994). In an attempt to quantify these effects, McElhaney et al (1994), conducted a comparative study and found that embalming caused a 12% reduction in ultimate compressive strength. The value of ultimate strength found in this study on fresh bone was 152.1 ± 21.6 MPa at quasi-static and 319 ± 23.9 MPa at dynamic rate in the longitudinal direction. After the 12% reduction in strength was accounted for, the range of ultimate strength found for human bone by McElhaney (1966), would be 168–355 MPa, which are similar to the values found in this study (Sanborn et al., 2016).

The failure strength of the human cortical bone in two directions was found to be positively correlated with strain rate. These experiments indicate that cortical bone from the human femur shaft is anisotropic, having higher stiffness and strength in the longitudinal direction of the bone at all strain rates. A review of available cortical bone failure strengths indicates that unembalmed and hydrated bone must be studied to obtain an accurate mechanical response. Furthermore, mechanical properties of the femur should not be applied to other bones for numerical modelling purposes, especially in the case of the tibia, which has been found to possess different failure strengths and moduli compared to the femur. Further work is needed to quantify rate-dependent regional variations within the same bone for numerical models. Additional studies are needed to assess the relationship between possible changes of failure strength with donor age (Sanborn et al., 2016).

Factors affecting viscoelasticity of the cortical bone (experimental):

- Temperature affects storage modulus
- Failure strength in transverse and longitudinal direction has a positive correlation with the strain rate used

10.2.3 Viscoelastic Characterization of Bovine Trabecular Bone Samples

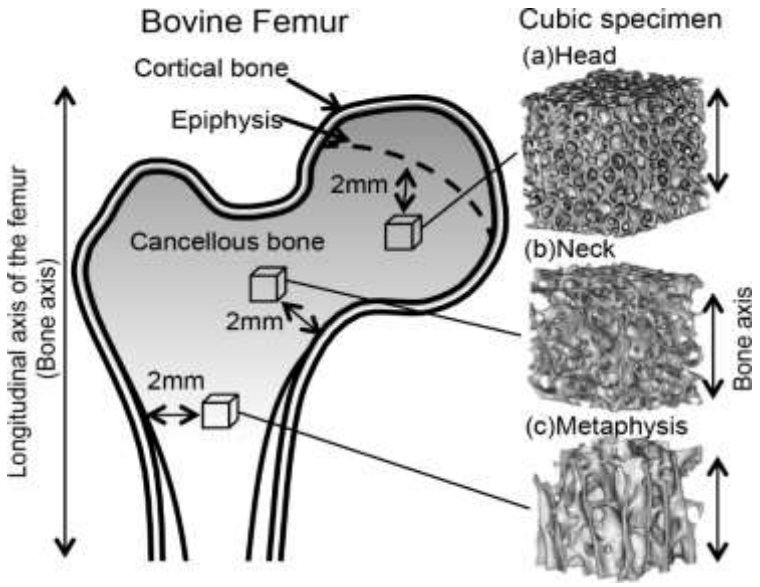

Figure 84: Anatomy of a bovine bone top area

This extract is form the paper: Viscoelastic Characterization of Bovine Trabecular Bone Samples

Knowledge of bone mechanical properties is important for bone substitutes design and fabrication, and more efficient prostheses development. The aim of this study is to characterize the viscoelastic behavior of bone specimens, through stress relaxation and fatigue tests performed to trabecular bone samples from bovine femoral heads. Relaxation tests consisted on preloading the samples at five different magnitudes and evaluate them for 1020 seconds, adjusting the results to a KWW mathematical model. Fatigue tests consisted of 700 load cycles and analyse their status at the end of the tests. As a conclusion we have that between relaxation stress and each preload there is linear relation and for samples with initial Young´s modulus greater than 1.5 GPa showed no effects due fatigue test loading cycles (D. Edgar I. et al, 2015).

The bone viscoelastic properties have already been explained as a result of different phenomena like thermoelasticity, piezoelectricity, movement of biological fluid through channels, as well as intrinsic viscoelasticity of collagen fibers (Lakes R., 1979),.

Iyo (2003) developed stress relaxation tests to evaluate cortical bone elastic modulus of a 36 months' bovine. The experiment consisted on obtaining small femur bars, the bars longitudinal direction was both perpendicular (5 pieces) and parallel (7 pieces) to the main femur axis, evaluating them through a stress relaxation tests, adjusting the results to an empirically created mathematical model. Equation below shows this mathematical model KWW, which is also the model that was used in this paper:

$$E(t) = E_0 \left\{ A_1 \exp[-(t/\tau_1)^{\beta}] + (1 - A_1) \exp[-(t/\tau_2)^{\gamma})] \right\}$$

where; E0 – initial Young's modulus; 1 τ – relaxation time for the quick region; 2 τ – relaxation time for the slow region; β and γ – geometric parameters; A1 – fractional contribution of the rapid relaxation region with respect to total relaxation. Quaglini (2008) performed stress relaxation tests on bovine femoral heads, they worked with 55 cylindrical specimens of 10 mm diameter and 20 mm height whose main axis was parallel to principal femur axis. The magnitudes of the preloads used during the test were 168, 320, 445, 577 and 727 N, strain rate was 0.015 s-1 and the load decreases was evaluated for 600 s. The resultant curves were normalized by dividing them between its initial preload, they concluded that the applied preload determines their behavior during relaxation test: the higher the preload, slower stress relaxation rate and higher stress magnitude to reach steady state (D. Edgar I. et al, 2015).

Factors affecting viscoelasticity of the cortical bone (experimental):

- Higher preload, slower stress relaxation rate and higher stress magnitude to reach steady state.

10.3 At what loading rate would a linear elastic model become viable (if any).

10.3.1 Viscoelastic Characterization of Bovine Trabecular Bone Samples

Knowledge of bone mechanical properties is important for bone substitutes design and fabrication, and more efficient prostheses development. The aim of this study is to characterize the viscoelastic behavior of bone specimens, through stress relaxation and fatigue tests performed to trabecular bone samples from bovine femoral heads. Relaxation tests consisted on preloading the samples at five different magnitudes and evaluate them for 1020 seconds, adjusting the results to a KWW mathematical model. Fatigue tests consisted of 700 load cycles and analyse their status at the end of the tests. As a conclusion we have that between relaxation stress and each preload there is linear relation and for samples with initial Young´s modulus greater than 1.5 GPa showed no effects due fatigue test loading cycles (D. Edgar et al., 2015).

Topolinski T. (2011), performed compressive fatigue tests to trabecular bone specimens from human femoral heads. The main characteristic of these tests is that load was increasing every certain number of cycles: at 1 Hz frequency, applying a cyclic sine load wave to the samples for 500 cycles and then increased in 10N the maximum load value, repeating the process until the specimen failure. They concluded that the specimens last between 3750 and 50,200 cycles and as loading cycles increase, the failure probability will also do so, but this increasing was linear (R2 = 0.9564).

For samples preservation, they were kept at room temperature submerged in a solution of 50% saline substance and 50% ethanol, this is the suggested method to preserve samples for short periods of time (less than 3 months), under these conditions the impact on the mechanical properties will be minimal (Ashman R.B., 1989). The samples were stored for a 4 days' maximum period.

We used 5 different preloads: 250, 500, 750, 1000, and 1250 N for stress relaxation tests at a constant strain rate $\dot{\varepsilon}$ = 0.0075 s-1. The best five successful results were selected for the subsequent analysis. The relaxation time was 1020 s, because we observed in unofficial tests that at this point were obtained load variations less than 0.5% (D. Edgar et al., 2015).

As it can be seen, the model fits to the experimental values so this part of the analysis is considered successful, likewise, numerical analysis reveals that it has a coefficient R2 = 0.98, that is why KWW model is considered valid for this study.

For stress relaxation tests, it is concluded that as the applied preload value increases, σ_{RELAX} results will present a higher standard deviation. It is concluded that decreasing percentage at the end of the test is independent of the preloading magnitude. In 5 selected results of the total number of specimens analysed, reduction percentages between 22% and 26% were obtained without showing a relationship with the applied preload. The relaxation stress presented a linear relation with the corresponding preload in the femoral heads evaluated specimens. The results allowed a

mathematical model KWW fit for stress relaxation, getting the specific constants for femoral trabecular bone (D. Edgar et al., 2015).

From fatigue tests, it was concluded that if the initial elastic modulus is less than 1.5 GPa, 700 loading cycles will be enough to damage their structures and cause significant stiffness decreases. They showed hysteresis rings so we can conclude that specimens absorbed energy was not being returned, and then their behavior is not perfectly elastic.

Effect of loading rate on a linear elastic model:

- Between relaxation stress and each preload there is linear relation and for samples with initial Young´s modulus greater than 1.5 GPa showed no effects due fatigue test loading cycles.
- If the initial elastic modulus is less than 1.5 GPa, 700 loading cycles will be enough to damage their structures and cause significant stiffness decrease.

10.4 How would these loading rates compare to different injury scenarios?

10.4.1 The effect of load rate on the axial fracture tolerance of the isolated tibia during automotive and military impacts

The input impact velocities ranged from 2.2 to 6.7 m/s, with energies ranging from 58 to 540 J. Twelve of the 22 specimens tested produced calcaneal fractures, while 10 tests did not cause fracture. Peak fracture forces ranged from 3.6 to 11.4 KN. The probability of calcaneal fracture was determined using a risk curve, showing a 10% probability of fracture at an impact force of 2.5 KN.

One of the first studies to investigate the fracture tolerance of the lower leg during military blasts was conducted by Griffin et al. (2001). With the goal of evaluating the protective capabilities of anti-mine protective footwear, full body cadavers were subjected to land mine detonations by placing the heel over a land mine. Loads were measured using load cells attached at the proximal tibia and strain gauges on the distal tibia and calcaneus. The axial loading rate, axial impulse (defined as the area under the force-time curve), weight of the explosive, and peak tibia force was determined to be contributing factors to prediction of pilon fractures. The risk of pilon fractures for the 50th percentile male was plotted over a range of loading rates, including 5, 10, and 20 kN/ms. During loading at a rate of 10 kN/ms, the force associated with a 10% risk of pilon fracture was 2.1 kN. Impacts delivered at greater load rate values resulted in higher force tolerances in the specimens.

Funk et al. (2002) investigated the effect of Achilles tension on axial loading tolerance of the foot/ankle complex. Forty-three lower extremity specimens were impacted axially with and without simulated Achilles tension, in order to study its effect. The Achilles tension replicated the active muscle tension that commonly occurs when occupants tense their legs prior to impact. A test apparatus was used to deliver an axial dynamic impact to the plantar surface of the foot at approximately 5 m/s. Active triceps surae muscle tension was replicated by applying tension to the Achilles tendon. Age, gender, body mass, and peak Achilles force were identified as predictor variables of the probability of injury. Assuming no Achilles tension, a 10% risk of fracture in the lower leg corresponded to a force of 5.8 kN for a 45-year-old 50th percentile male. Active muscle tension during impact exerted through the Achilles tendon increased the axial tibial force associated with a 10% risk of fracture by as much as 2 kN.

McKay et al. (2009) used lower extremity post mortem human specimens (PMHS) to develop injury criteria for occupants involving short duration axial loads of the lower leg from underbelly blast events. Eighteen specimens were each instrumented with a tibia triaxial load cell at the midshaft and strain gage rosettes were attached to the medial aspect of the calcaneus and to the medial surface of the tibia. The specimens were impacted using a high rate, linear floorplate impactor weighing 36.7 kg. The steel floorplate impacted the plantar surface of the foot, and was allowed to travel 24 mm to mimic floorplate intrusion after impact. The PMHS specimens were divided into three groups, using

three incrementally severe loading scenarios (average impact velocities of 7.2, 9.9, and 11.8 m/s and kinetic energies of 941, 1802, and 2494 J, respectively). Each specimen was subjected to a single impact. Twelve of the specimens suffered fractures of the calcaneus, talus, fibula, and/or tibia. Peak axial tibia force and impactor velocity were determined to be the best factors to identify injuries. The survival analysis identified a tibia axial force of 2.4 kN as having a 10% probability of incapacitating injury (Figure 1.4).

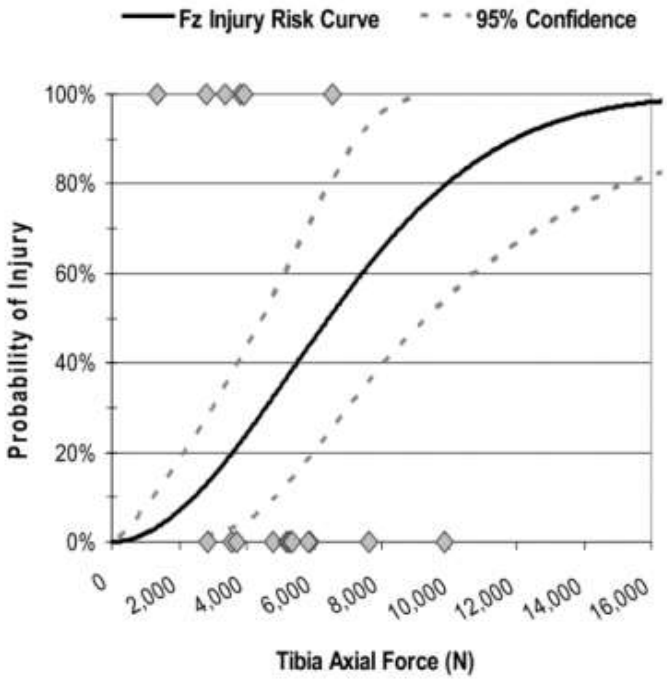

Figure 85: Injury Probability Curves, Yoganandan Model (Yoganandan et al., 2014).

A 10% risk of injury corresponded to an axial tibia force of 6.8 kN for a 45-year-old male.

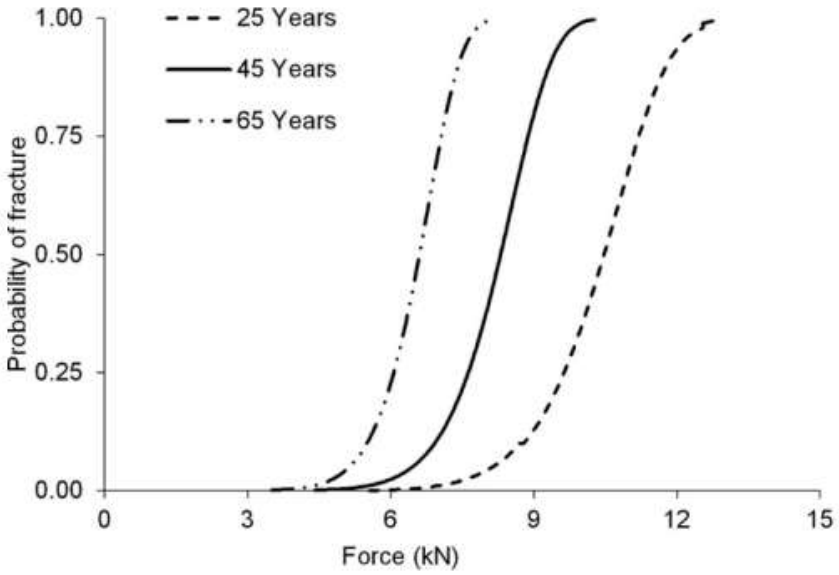

Figure 86: Injury Probability Curves, Yoganandan Model (Yoganandan et al., 2014).

A 10% risk of injury corresponded to an axial tibia force of 6.8 kN for a 45-year-old male.

Study	Loading Scenario	Significant Injury Risk Factors	10% Injury Risk Force	Injury Locations
Yoganandan *et al.* (1996, 1997)	Automotive	Axial force, age	5.4 kN	Foot/ankle complex
Griffin *et al.* (2001)	Military	Load rate, impulse, axial force, body weight	2.1 kN	Calcaneus, cuboid, navicular, talus, and distal tibia
Seipel *et al.* (2001)	Automotive	Axial force	2.5 kN	Calcaneus
Funk *et al.* (2002)	Automotive	Axial force, gender, age, body weight, Achilles tension	5.8 kN	Foot/ankle complex
McKay and Bir (2009)	Military	Axial force, impactor velocity	2.4 kN	Calcaneus, cuboid, fibula, tibia, talus
Quenneville *et al.* (2011)	Military	Projectile mass, velocity, momentum, kinetic energy, impact duration, impulse, axial force, age, height, body mass	7.9 kN	Distal tibia
Yoganandan *et al.* (2014)	Automotive	Axial force, age	6.8 kN	Foot/ankle complex
Bailey *et al.* (2015)	Both	Axial force, dorsiflexion angle	6.2 kN	-

Figure 87: Summary of Previous Injury Tolerance Studies (A. Martinez A., 2016)

The loading scenario replicated through testing, significant factors that contribute to injury prediction, force that corresponds to a 10% probability of injury, and locations of injury are summarized for previous cadaveric lower leg axial impact studies.

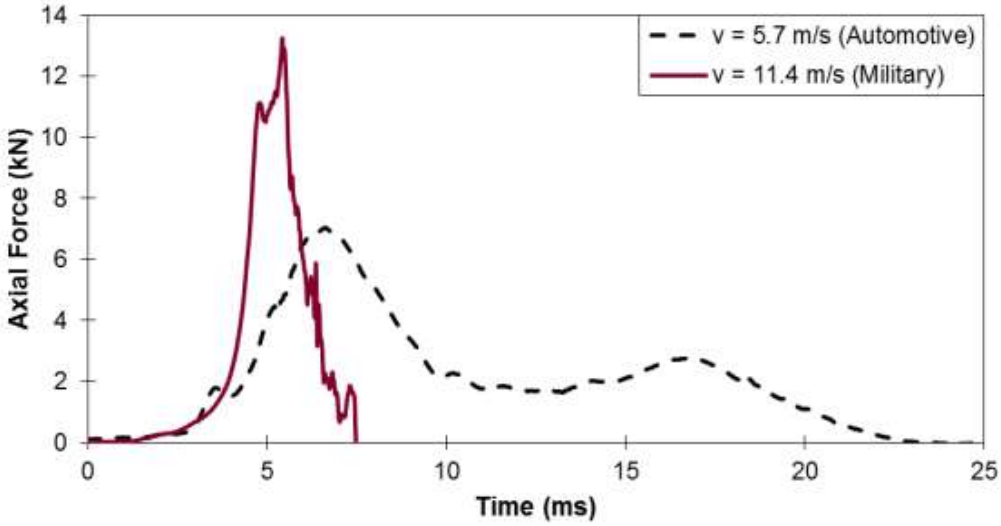

Figure 88: Representative Fracture Force-Time Curves for Both Test Conditions (A. Martinez A., 2016)

The higher-rate military condition had a larger peak force but shorter duration (13.5 kN, 6.2 ms) than the lower-rate condition (10.9 kN, 18.5 ms). Impulse was calculated as the integral of each force-time curve. Impulse for the higher-rate condition was 30.3 Ns, compared to 57.1 Ns for the lower-rate condition.

a)

	Auto Non-Fracture		Low-Rate Fracture		High-Rate Non-Fracture		Military Fracture	
	Model	Experiment	Model	Experiment	Model	Experiment	Model	Experiment
Peak Force (kN)	7.9	8.8	8.3	11.3	12.4	10.5	12.8	13.3
Duration (ms)	15.2	12.0	16.1	12.1	8.4	7.1	8.5	4.6
Impulse (Ns)	41.0	39.2	51.3	37.5	38.7	27.3	41.9	18.2

b)

	Low-Rate Non-Fracture			Low-Rate Fracture			High-Rate Non-Fracture			High-Rate Fracture		
	F	D	I	F	D	I	F	D	I	F	D	I
Model/Experimental	0.90	1.27	1.05	0.73	1.33	1.37	1.18	1.18	1.42	0.96	1.85	2.30

Figure 89: summary of model validation results (A. Martinez A., 2016)

a) The values for peak axial force, impact duration, and impulse values for the four test conditions in the experimental and computational testing.

b) These values were compared between the four simulation tests and the corresponding experimental tests by providing the ration between model values and experimental values.

a)	Lower-Rate (Automotive) Impact Condition				
Specimen	Projectile Mass (kg)	Force (kN)	Kinetic Energy (J)	Impulse (Ns)	Load Rate (kN/ms)
1494R	31.6	10.6	435	53.8	2.3
1536R	31.6	10.8	442	57.1	1.2
1538L	21.0	9.1	449	26.1	1.3
1541L	34.6	12.8	603	62.7	2.5
1567L	34.6	11.3	666	45.0	2.3
1600R	21.0	11.0	564	48.4	3.7
Average (±S.D.)	29.1 (6.4)	10.9 (1.2)	526 (98.2)	48.9 (12.8)	2.2 (0.9)

b)	Higher-Rate (Military) Blast Condition				
Specimen	Projectile Mass (kg)	Force (kN)	Kinetic Energy (J)	Impulse (Ns)	Load Rate (kN/ms)
1494L	6.9	13.3	443	22.1	4.6
1536L	8.3	14.3	594	30.3	9.2
1538R	8.3	13.5	533	27.3	4.7
1541R	6.5	11.8	429	27.3	3.7
1567R	6.9	13.3	443	27.3	6.2
1600L	7.6	14.5	612	25.9	4.8
Average (±S.D.)	7.4 (0.8)	13.5 (1.0)	509 (82)	26.7 (2.7)	5.5 (2.0)

Figure 90:Specimen Fracture Information (A. Martinez A., 2016)

Results for both the a) lower-rate impact condition and b) higher-rate condition showing peak values for each factor that were used for statistical analysis. The values for projectile mass, kinetic energy, and loading rate corresponded to

the fracture impact, while force and impulse corresponded to the impact (pre-fracture or fracture) that achieved peak forces. Detailed specimen information (age, potted mass, length) is provided in the table below.

Donor	Age (years)	Right/Left	Potted Specimen Mass (kg)	Tibia Length (m)
1494	50	L	1.47	0.40
		R	1.56	0.41
1536	55	L	1.54	0.43
		R	1.58	0.43
1538	66	L	1.49	0.38
		R	1.48	0.40
1541	68	L	1.51	0.41
		R	1.52	0.41
1567	61	L	1.60	0.42
		R	1.53	0.41
1600	74	L	1.48	0.38
		R	1.49	0.37

Figure 91: Specimen Information (A. Martinez A., 2016)

The donor number, age, side, potted mass, and length are given for all the tibia specimens used during experimental testing. All donors were male, and each provided a pair of tibias.

10.5 THUMS model

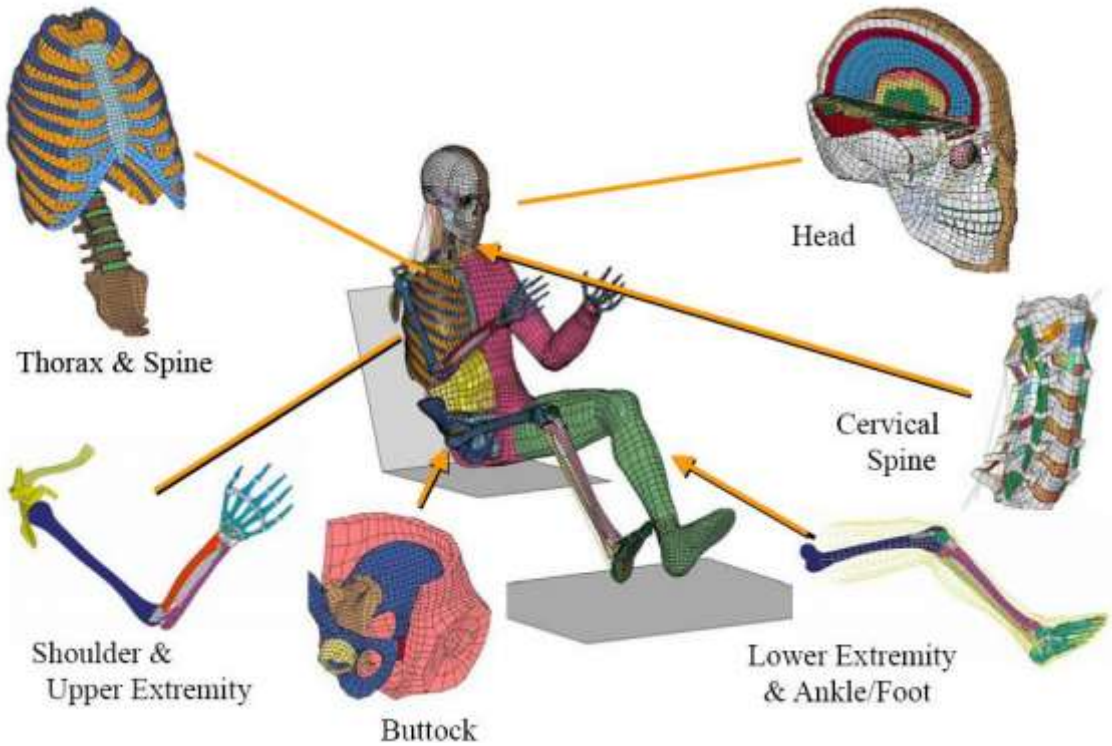

Figure 92: Composition of whole body THUMS (LSTC, 2018)